Tréhu, A.M., Bohrmann, G., Rack, F.R., Torres, M.E., et al., 2003
Proceedings of the Ocean Drilling Program, Initial Reports Volume 204

7. SITE 1248[1]

Shipboard Scientific Party[2]

INTRODUCTION

Site 1248 (proposed Site HR6) was drilled in ~830 m of water ~300 m northwest of the southern Hydrate Ridge summit (see Fig. **F1**, p. 51, in the "Leg 204 Summary" chapter). This site is located in the middle of a small (~150 m diameter) high-reflectivity spot on the seafloor imaged by a deep-tow side-scan sonar survey (see Fig. **F7**, p. 57, in the "Leg 204 Summary" chapter) (Johnson et al., in press). The small spot is located 300 m north of a larger, circular high-reflectivity patch around the Pinnacle, a well-known active carbonate chemoherm. These are the only two locations on southern Hydrate Ridge where high backscatter reflectivity, interpreted to be the seafloor manifestation of fluid venting, is observed. Television-sled surveys revealed some evidence for the presence of scattered authigenic carbonate fragments within the small high-reflectivity patch, which might be responsible for the higher backscatter signal observed in the side-scan sonar data. The three-dimensional (3-D) seismic data show attenuation of the underlying stratigraphic reflectivity, similar to what is observed beneath the Pinnacle (see Fig. **F7**, p. 57, in the "Leg 204 Summary" chapter). Both areas of high backscatter overlie the intersection of seismic Horizon A and the bottom-simulating reflector (BSR).

F1. Bathymetric map, p. 25.

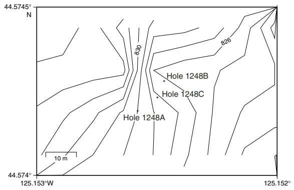

The principal objectives at Site 1248 were to investigate (1) whether the sediments below the high-reflectivity seafloor spot contain evidence of active fluid advection and (2) if these fluids are supplied by Horizon A.

Three holes were drilled at Site 1248 (Fig. **F1**). Logging-while-drilling (LWD) measurements were made in Hole 1248A down to 194 meters below seafloor (mbsf). Hole 1248B was abandoned at 17 mbsf after three cores. In Hole 1248C, 5 extended core barrel (XCB) cores were drilled to 48 mbsf followed by 11 advanced piston corer (APC) cores, and 1 XCB core to 149 mbsf. After poor core recovery (23%) in Cores

---

[1] Examples of how to reference the whole or part of this volume.
[2] Shipboard Scientific Party addresses.

Ms 204IR-107

204-128C-1X through 5X, recovery increased to 90% and remained high to total depth.

OPERATIONS

Three holes were drilled at Site 1248 (Table **T1**), under good weather conditions. Wind speed was 8–24 kt, gusting to 28 kt; seas were 4–9 ft; swell was 6–10 ft and the prevailing sea-surface current was from the north at ~0.5 kt.

T1. Coring summary, p. 62.

Hole 1248A was drilled without coring to obtain the initial LWD data for this site to a total depth (TD) of 194.0 mbsf. LWD operations began at 2130 on 20 July by spudding Hole 1248A at 832 m water depth. Drilling proceeded at reduced rates of penetration (ROP) of 15 m/hr and 15 spm circulation to moderate formation washout at shallow depths below seafloor. No real-time measurement-while-drilling (MWD) or nuclear magnetic resonance (NMR) data were recorded over this interval, as the pump rate was insufficient to activate the turbines in these tools. The penetration rate was increased to ~25 m/hr at a bit depth of 30 mbsf to TD (190 mbsf), and real-time MWD and NMR data were recorded (see **"Downhole Logging,"** p. 19). The LWD tools were pulled to ~60 m above the seafloor at 0700 on 21 July. Total bit run took ~15 hr.

Hole 1248B was spudded at 0300 hr on 1 August. Three cores were collected with the APC, after which the hole was abandoned at 17 mbsf. Coring disturbance resulting from near-seafloor massive gas hydrates and a shattered liner during retrieval of Core 204-1248B-3H caused poor core recovery (44%). There was one APCT tool deployment in Hole 1248B. There were no other special tools deployed at this site.

Hole 1248C was spudded with the XCB in an attempt to increase core recovery. Cores were drilled to 48 mbsf. Recovery was poor (23%) in Cores 204-128C-1X to 5X, and then it increased in Cores 204-1248C-6H through 17X to 90% of the penetration. Cores 204-128C-6H to 16H were collected with the APC; these were followed by one XCB core to 149 mbsf. Five in situ temperature runs were made at this hole: two APCT tool, two DVTPP, and one DVTP runs (Table **T13**).

LITHOSTRATIGRAPHY

Three holes were drilled at Site 1248, located to the west of the southern summit of Hydrate Ridge (see Figs. **F1,** p. 51, and **F7,** p. 57, both in the "Leg 204 Summary" chapter). Holes 1248B and 1248C were both cored, although Hole 1248B was abandoned at 17 mbsf as a result of poor recovery (~43%). Similarly, Hole 1248C had poor recovery from 0 to 40 mbsf (~26%), but by combining the data from both holes, it was possible to identify the complete sedimentary sequence at Site 1248.

On the basis of visual core descriptions (VCDs), smear slide and thin section analyses, and other parameters such as calcium carbonate content (expressed as weight percent $CaCO_3$) and mineralogy from X-ray diffraction (XRD), two main lithostratigraphic units (Units I-II and III) were distinguished (Fig. **F2**). We also compare and correlate our results with the 3-D multichannel seismic reflection data, downhole LWD data (resistivity at the bit [RAB] and density-porosity), and physical property measurements (magnetic susceptibility [MS] and gamma ray attenua-

F2. Lithostratigraphic summary, p. 26.

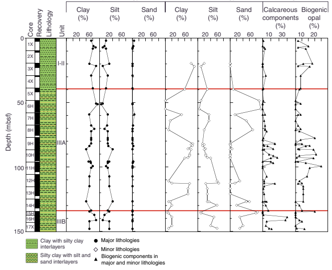

tion [GRA] density) to better constrain the lithostratigraphic units (Fig. F3).

F3. Seismic reflection profile and LWD data, p. 27.

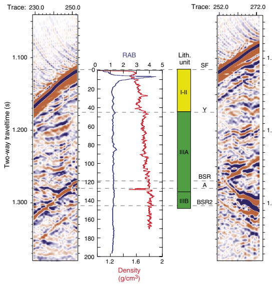

The sedimentary section recovered at Site 1248 is primarily composed of diatom-bearing to diatom-rich clay and silty clay above the Horizon Y unconformity identified on the 3-D seismic images at 39 mbsf and diatom- and nannofossil-bearing silty and sandy turbidites below it (Figs. F2, F3). We were able to define two lithologic units above Horizon Y at Sites 1245, 1247, and 1250. However, poor recovery (~34%) at this site made identification of two distinct units impossible. For the sake of consistency between the sites and based on both the 3-D seismic data and the proximity of the sites to each other, we decided to call this uppermost unit lithostratigraphic Unit I-II. This same upper unit definition above Horizon Y was applied at Site 1249. Correlation of the lithostratigraphic units defined here with the other Leg 204 sites is summarized in Figure F10, p. 60, in the "Leg 204 Summary" chapter.

Lithostratigraphic Units

Lithostratigraphic Unit I-II

Intervals: Cores 204-1248B-1H through 3H and Core 204-1248C-1X to Section 5X-1
Depths: Hole 1248B: 0.00–16.50 mbsf and Hole 1248C: 0.00–39.00 mbsf
Age: mid-Pleistocene to Holocene

Lithostratigraphic Unit I-II is a sequence of dark greenish gray (5GY 4/1), homogeneous fine-grained sediments that are mainly hemipelagic diatom-bearing to diatom-rich clay and silty clay. Most of the recovered sediments show mousselike and soupy textures (see **"Lithostratigraphy,"** p. 5, in the "Explanatory Notes" chapter) that obscure original sedimentary structure and are typically found in gas hydrate–bearing sediments. Authigenic carbonate precipitates related to the presence of gas hydrate are common in the upper part of this unit. Mottles and patches of dark gray (N3) iron sulfides and bioturbation are abundant. The lower boundary of lithostratigraphic Unit I-II is defined by the first occurrence (FO) of coarse grain–size sediments at ~39 mbsf in Core 204-1248C-5X (Fig. F2).

Smear slide descriptions indicate that lithostratigraphic Unit I-II is composed of sediments that are typically ~80% clay, ~19% silt, and ~1% sand. The major nonbiogenic components of the unit are quartz, feldspar, and clay and opaque minerals. Opaque grains, mostly sulfides in irregular and framboidal forms, are common in lithostratigraphic Unit I-II, especially between 20 and 30 mbsf, where they sometimes compose >10% of the total sediment (e.g., Samples 204-1248C-3X-1, 60 cm, and 4X-1, 20 cm). Sulfides appear as dark gray (N3) mottles or stained surfaces. Bioturbation, often evidenced by iron sulfide precipitates, is moderate to abundant throughout the lithostratigraphic unit.

The biogenic components (mainly siliceous microfossils) compose 2% to 13% of the total sedimentary components. Diatoms are abundant (≤12%) in the top 20 mbsf of lithostratigraphic Unit I-II (e.g., Samples 204-1248B-2H-1, 20 cm; 2H-2, 70 cm; and 204-1248C-3X-1, 60 cm) and are typically part of the silt fraction. Calcareous microfossils are rare, with foraminifers and nannofossils present at the base of lithostratigraphic Unit I-II in Sections 204-1248C-4X-1 and 5X-1 (Fig. F2).

The sediments of lithostratigraphic Unit I-II are generally disturbed and contain both soupy and mousselike textures that preserve no original sedimentary structures (Fig. **F4**). Gas hydrate was detected and sampled on the catwalk in several core sections between 0 and 10 mbsf. The observed sediment textures in this interval are spatially correlated with negative temperature anomalies in the infrared (IR) images and are, therefore, presumed to result from the dissociation of gas hydrate. The distribution of soupy and mousselike intervals and their relationship to the presence of gas hydrate is discussed further in **"Sedimentary Evidence of Gas Hydrate,"** p. 6.

F4. Sediment textures related to hydrate dissociation, p. 28.

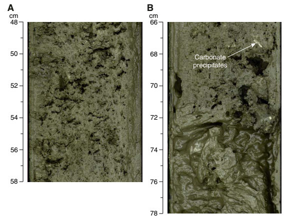

T2. Location of sampled carbonate nodules, p. 64.

Authigenic carbonates found at the top of lithostratigraphic Unit I-II are associated with mousselike intervals in the cores (Figs. **F4B**). Several large carbonate nodules (~2–5 cm in diameter) were found in every section of Core 204-1248B-1H, from 0 to 2.3 mbsf (Table **T2;** Fig. **F5**). Thin section analysis of carbonate nodules indicates that the concretions consist of micritic carbonate containing biogenic and nonbiogenic components and clasts (Fig. **F6**). Carbonate clasts are predominantly rich in quartz, feldspar, and glauconite grains. Bioclasts are mainly foraminifers (Fig. **F6**). Smaller carbonate precipitates (~0.2 cm in diameter) are scattered within the sediment in Sections 204-1248B-1H-1 and 1H-2 (Fig. **F4**), and carbonate-rich patches are present in interval 204-1248C-1X-1, 116–118 cm. Two phases of calcite of different Mg content were recognized in the upper 20 mbsf, based on the XRD analyses; their abundance seems to decrease downhole from Section 204-1248B-1X-1 to 204-1248C-4X-1 (Fig. **F7**).

F5. Carbonate nodule with mousselike sediments and a carbonate nodule, p. 29.

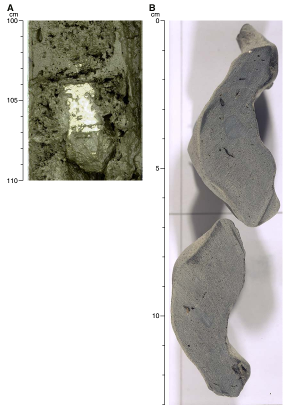

F6. Carbonate nodule, p. 30.

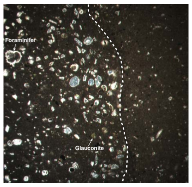

Lithostratigraphic Unit III

Interval: Sections 204-1248C-5X-1 through 17X-CC
Depth: 39.00–148.33 mbsf
Age: mid- to early Pleistocene

Lithostratigraphic Unit III is mainly composed of diatom- and nannofossil-bearing silty clay interbedded with thin layers of graded silt and fine sand, which we interpret as turbidites (Fig. **F2**). A fine-grained, thick debris flow deposit dominated by biogenic components disrupts the cyclicity of turbidite frequency toward the middle of the lithostratigraphic unit. Seismic reflector Horizon A, a regional stratigraphic marker predominantly composed of volcanic glass–rich sands and ashes, was also identified at Site 1248 within this lithostratigraphic unit. The upper boundary of lithostratigraphic Unit III is located at ~39 mbsf and is defined by (1) the onset of silt and sand turbidites, the frequency of which varies downhole, and (2) the increase in biogenic components, especially calcareous components (Fig. **F2**). The boundary between lithostratigraphic Units I-II and III correlates with Horizon Y, a seismic reflector that corresponds to the unconformity identified on the 3-D seismic data and drilled at Sites 1245, 1247, and 1250 (Fig. **F3**) (see Figs. **F5,** p. 55, **F6,** p. 56, and **F7,** p. 57, all in the "Leg 204 Summary" chapter). Based on changes in the abundance of biogenic calcareous components, lithostratigraphic Unit III was subdivided into two subunits (Subunits IIIA and IIIB) (Fig. **F2**).

F7. XRD records showing a decrease in calcite, p. 31.

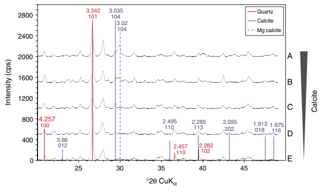

Lithostratigraphic Subunit IIIA

Lithostratigraphic Subunit IIIA (Hole 1248C; 39–134 mbsf) consists of dark greenish gray (5GY 4/1) diatom- and nannofossil-bearing silty clay. Based on smear slide analyses, this subunit is primarily composed of sediment with ~75% clay, ~25% silt, and <1% sand (Fig. **F2**). This major lithology is interbedded with thin (2 mm to 1 cm), closely spaced sandy silt and silt turbidites (Fig. **F2**). These turbidites dominate the intervals from 39 to 75 mbsf and from 110 to 133.5 mbsf, showing a maximum-event frequency of 50 cm in Cores 204-1248C-7H and 8H (see **"Site 1248 Visual Core Descriptions"**). At the bases of the turbidites, intense bioturbation of the hemipelagic clay is commonly observed (e.g., Core 204-1248C-16H). Iron sulfides are common throughout lithostratigraphic Subunit IIIA, especially in Core 204-1248C-8H, from 67 to 75 mbsf, showing abundant mottles, patches, and iron sulfide nodules of dark gray (N3) color. Mousselike textures were observed near intervals where gas hydrate was sampled at 87 and 105 mbsf (see **"Sedimentary Evidence of Gas Hydrate,"** p. 6).

Toward the middle of the subunit, from 82 to 112 mbsf, a 25-m-thick sedimentary sequence characterized by soft-sediment deformation features, convoluted bedding, and clay clasts was identified and interpreted to represent multiple debris flow deposits (Sections 204-1248C-9H-4 through 9H-5; 10H-2 to 10H-5; 11H-2 to 11H-5; and 12H-4 to 12H-5). Mud clasts, ranging from 1 to 5 cm in diameter on average, are embedded in a clay-rich convoluted matrix (Fig. **F8**). Biogenic components are common throughout the debris flow interval, composing on average 13% of the sedimentary components. Locally, they compose up to 15% (nannofossils) and 20% (diatoms) of both the major and minor lithologies (Fig. **F2**).

F8. Debris flow deposits, p. 32.

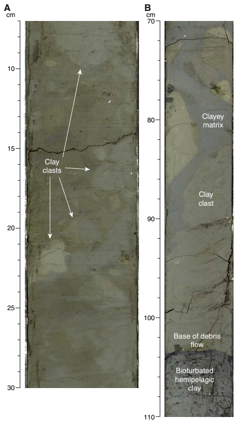

High concentrations of beige- to white-colored volcanic glass–bearing sands and volcanic ash (20%–60% glass content) were observed between 126 and 132 mbsf and correspond to the approximate depths of Horizon A in the 3-D seismic and LWD density data (Sections 204-1248C-14H-3 to 14H-CC) (Figs. **F3**, **F9**). The volcanic glass–rich sediment and ash sequences, typically ~2–3 cm thick, are composed of dark-greenish gray volcanic glass–rich sands that grade into sandy to silty ash containing up to 60%–80% glass. The glass is generally concentrated near the top of a fining-upward sequence because its low density, caused by the presence of vesicles, the amorphous mineral composition, and the platy shape cause it to settle more slowly through the water column than other mineral grains (Fig. **F9**).

F9. Volcanic ash– and glass–rich sand layers, p. 33.

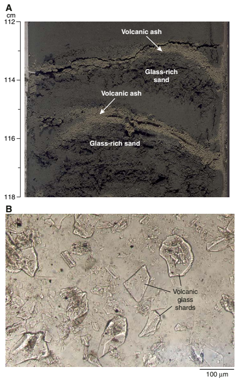

Prior to splitting Core 204-1248C-14H, a 5-cm-thick layer of light-colored "sand" was observed through the liner of the core on the catwalk. Subsequent drilling into the core liner to release excess gas pressure destroyed this light-colored layer, spreading a thin (<1 mm thick) coating of volcanic glass around the surface of the core. Examination of the core confirmed the existence of the glass; although physical evidence for the original mode of emplacement of the 5-cm-thick layer was not preserved.

Lithostratigraphic Subunit IIIB

Lithostratigraphic Subunit IIIB (Hole 1248C; 134–149 mbsf) consists of nannofossil-rich and diatom-bearing clay to silty clay. Smear slide analyses indicate that the presence of fine-grained sediment increases in lithostratigraphic Subunit IIIB (76% clays, 24% silts, and no sands in major lithology). Iron sulfide precipitates and bioturbation are moderate to rare along this subunit. The calcareous biogenic components, primarily nannofossils, increase considerably with respect to lithostratigraphic Subunit IIIA. They locally compose up to 30% of the sediment. Biogenic opal, predominantly in the form of diatoms, composes 5%–10% of the sediment (Figs. **F2**). Near the bottom of lithostratigraphic

Subunit IIIB, glauconite-rich sandy silts (up to 11% of glauconite) are present as minor lithologies (e.g., Sections 204-1248C-17X-3 and 17X-5).

Sedimentary Evidence of Gas Hydrate

Gas hydrate was sampled from one core in Hole 1248B and from seven cores in Hole 1248C. Although gas hydrate samples were removed from cores on the catwalk prior to sedimentological description, a disruption of the remaining sediment fabric, interpreted to be induced by hydrate dissociation, was described for all cores above the BSR in Holes 1248B and 1248C.

Soupy sediment textures were described in Cores 204-1248B-1H and 2H and 204-1248C-2X (Fig. **F4B**). These soupy layers range in thickness from 5 to 25 cm. In all cases, the soupy layer was bordered on both the top and bottom by sediment exhibiting mousselike textures. Carbonate nodules ranging in size from <0.1 to 0.5 cm in diameter were also found in the mousselike layer bordering the soupy sediment in Core 204-1248B-1H. Core 204-1248B-1H was the only core in Hole 1248B in which carbonate nodules were found and the only one, which these nodules were associated with sediment disruption related to gas hydrate dissociation (Fig. **F5A**).

Side-scan sonar imagery collected prior to this leg (Johnson et al., in press) show an apron of high backscatter surrounding Site 1248, which is interpreted as carbonate near or just beneath the seafloor. Therefore, the presence of carbonate nodules at this site was not unexpected. In addition, from 0 to 50 mbsf, the alkalinity of interstitial water (IW) samples is generally high, suggesting chemical conditions are favorable for authigenic carbonate precipitation at Site 1248 (see **"Carbon Cycling,"** p. 10, in "Interstitial Water Geochemistry").

Mousselike textures associated with sediment disruption and the dissociation of gas hydrate are present in all of the cores recovered above 125 mbsf from Hole 1248C and in all cores recovered from Hole 1248B (Fig. **F4A**); this was noted in the VCDs. IR thermal images helped distinguish ambiguous zones of stiffer mousselike textures at intervals along the edges of the core or next to a void from mousselike textures within the center of the core (see **"Physical Properties,"** p. 14). The stiffer disrupted textures, however, are still thought to be the result of hydrate dissociation rather than disturbance related to coring (also see **"Lithostratigraphy,"** p. 5, in the "Explanatory Notes" chapter).

Smear slide analyses of the sediments within and surrounding these disrupted zones do not reveal any characteristics that distinguish these zones from the dominant lithologies of lithostratigraphic Unit I-II. The soupy and mousselike layers are typically present in the predominant silty clay and diatom-bearing silty clay. At this site, silty and sandy interlayers that tend to preserve original bedding contacts are present within 0.1 to 1 m of the disrupted layers but do not show evidence of the dissociation of gas hydrate.

Our observations of the relationship between core disruption and the dissociation of gas hydrate are supported by both the IW geochemistry and LWD data from Site 1248. The chemical composition of IWs (see **"Interstitial Water Geochemistry,"** p. 9) indicates freshening relative to seawater values from 0 to 20 mbsf and also at discrete intervals to the estimated depth of the BSR at 115 mbsf. These low chlorinity anomalies are likely related to the addition of freshwater to the system from the dissociation of hydrate. In addition, from 0 to 20 mbsf, high LWD resistivity values indicate the presence of hydrate in the pore space of the sediment (see **"Downhole Logging,"** p. 19).

Environment of Deposition

The hemipelagic intervals between turbidites in lithostratigraphic Unit III typically vary in thickness from 5 to 20 cm, which is comparable in thickness to the adjacent turbidites. The largest clay-dominated zone, from 80–112 mbsf (i.e., Section 204-1248C-9H-3 through Core 12H), is actually composed of unsorted clay clasts within a clay to silty clay matrix that is high in biogenic opal and calcareous components. Soft-sediment deformation and load structures delineated by thin sulfide-rich laminae are observed within this interval as well. We interpret this interval as a series of debris flow deposits. Similar deposits at Sites 1249 and 1250 were also identified near the middle of lithostratigraphic Unit III and may correlate with the deposits seen here. The higher abundance of biogenic components in the debris flows at 80–112 mbsf, their unsorted nature, and their fine grain size suggest that they were derived from a proximal source area rich in hemipelagic clays.

Seismic Horizon A was recovered at Site 1248, thus providing a deep tie point for intersite correlation. Similar to Sites 1245 and 1250, Horizon A at Site 1248 consists of volcanic glass–rich turbidite sequences. The highest glass concentrations are present at the top of the sequences, where the less dense grains (like volcanic glass shards) settle out from suspension. The inverse grading of ash concentration within the normal graded sands and silts and the multiple presence of such events over a short period of time (i.e., they are separated by a few centimeters) suggest the volcanic ash was deposited by turbidity currents rather than repeated air fall ash deposition. However, future detailed sedimentologic work will better define the mode of emplacement.

The lack of coarse-grained material in the upper portion of lithostratigraphic Unit I-II, in addition to the high biogenic opal content, is indicative of sediment deposition dominated by hemipelagic clay accumulation. In contrast, coarser-grained sediments and graded beds indicate deposition dominated by periodic turbidity currents, which at Sites 1250, 1247, and 1245 are observed in lithostratigraphic Units II and III and at Site 1248 in the lower part of Units I-II and III. High-frequency turbidites usually also indicate a higher sedimentation rate than deposition dominated by hemipelagic clay accumulation. Based on the observed stratigraphy here, this would imply a higher sedimentation rate for lithostratigraphic Unit III vs. Unit I-II.

BIOSTRATIGRAPHY

A "bright spot" located northwest of the southern Hydrate Ridge summit was observed by a deep-towed SeaMARC side-scan sonar survey (Johnson et al., in press). The objective of drilling at Site 1248 was to test whether this bright spot is a buried carbonate formation that may be an incipient chemoherm.

Three holes were drilled at Site 1248. Hole 1248A was drilled to make LWD measurements. Cores recovered from Holes 1248B and 1248C contain a 150-m-thick Quaternary sedimentary sequence. Abundant gas hydrate samples were recovered from Cores 204-1248C-1X through 5X. In this interval, core recovery is poor, ranging from 9% to 31%, probably as a result of massive gas hydrate close to the seafloor. Biostratigraphy for Site 1248 was based on examination of diatoms and calcareous nannofossils from all core catcher samples and a few samples from within cores in Hole 1248C.

Diatoms

Hole 1248C yields common and moderately preserved diatoms, except for the lower part of the hole. Diatoms are common and poorly to moderately preserved in the interval from 0 to 120 mbsf and are few to absent and poorly preserved in the interval from 120 mbsf to the bottom of Hole 1248C. Diatom assemblages from Hole 1248C are dominated by species such as *Stephanopyxis dimorpha, Stephanopyxis* spp., *Neodenticula seminae,* and *Thalassionema nitzschioides*. A few warm-water taxa, such as *Hemidiscus cuneiformis* and *Fragilariopsis doliolus,* are present sporadically. Neritic species, such as *Actinoptychus senarius* and *Cocconeis* spp., are present in most samples, whereas freshwater species, such as *Aulacoseira* spp., are present sporadically.

All core catcher samples examined contain *N. seminae* and *Proboscia curvirostris* but do not contain *Actinocyclus oculatus*. They are assigned to North Pacific Diatom Zone (NPD) 11 (*P. curvirostris* Zone; 0.3–1.0 Ma). The absence of *A. oculatus* in the interval from 120 mbsf to the bottom of Hole 1248C is possibly a result of the dissolution of the species, which is suggested by the poor preservation of diatoms in this interval. Therefore, the age estimated for the interval from 120 mbsf to the bottom of Hole 1248C is older than the last occurrence (LO) of *A. oculatus* (1.0 Ma). The age of the bottom of Hole 1248C is estimated to be younger than 1.6 Ma, based on the presence of *P. curvirostris* in Sample 204-1248C-17X-CC (148.5 mbsf).

Calcareous Nannofossils

The sequence above 94 mbsf in Hole 1245C contains very rare and poorly to moderately preserved calcareous nannofossils, except for Sample 204-1248C-6H-CC. Rare to common and moderately to well-preserved calcareous nannofossils were found in the lower sequence, from 94 mbsf to the bottom of the hole.

Emiliania huxleyi and *Pseudoemiliania lacunosa* are absent in Samples 204-1248C-1X-CC to 4X-CC (2.38–29.64 mbsf), assigning the interval to Zone NN20. The LO of *P. lacunosa,* which is observed in Sample 204-1248C-5X-CC (41.35 mbsf), marks the NN19b/NN20 zonal boundary. We are unable to reliably determine the small *Gephyrocasa* spp. Acme Zone in the interval between 66.33 and 94.51 mbsf, where calcareous nannofossils are barren or very rare. The LO of *Calcidiscus macintyrei* (1.59 Ma) was found in Sample 204-1248C-13H-CC, indicating an early Pleistocene age for the sediments. Abundant *Gephyrocapsa lumina* are present in Sample 204-1248C-17H-CC (148.47 mbsf); therefore, the sediments at the bottom of Hole 1248C were assigned to the lower part of Quaternary Zone NN19, with an age of younger than 1.67 Ma.

Summary

A number of samples from Site 1248 yielded common to rare diatoms and common to rare calcareous nannofossils, which allowed us to recognize one diatom and two nannofossil events for Site 1248 (Table T3). However, we are unable to further subdivide the zones of NN20 and NN21 and the zones of NPD 12 and 11 because of poor core recov-

T3. Bioevents, p. 65.

ery in this interval. It is also impossible to determine some of the mid-Pleistocene bioevents, such as the small *Gephyrocapsa* spp. Acme Zone and the LO of *A. oculatus,* because poorly preserved diatoms and very rare calcareous nannofossils were found in the middle sequence of the hole. The age of the bottom of Hole 1248C is estimated to be younger than 1.6 Ma, based on the presence of *P. curvirostris* in Sample 204-1248C-17X-CC (148.5 mbsf). This estimate is supported by the presence of *G. lumina* in the same sample. Based on diatom and two nannofossil events and assemblages, the sediment sequence in Hole 1245C was determined to be of early Pleistocene–Holocene age (Fig. **F10**).

F10. Diatom and nannofossil event marker species, p. 34.

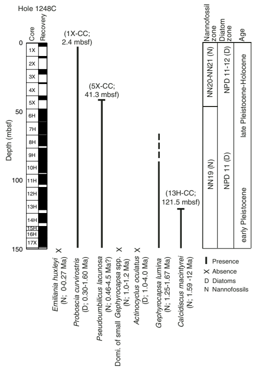

The linear sedimentation rates at Site 1248 were calculated using the biostratigraphic data (Table **T3**). A low sedimentation rate was estimated for the top of Hole 1248C, based on the absence of *E. huxleyi* and presence of *P. curvirstris* in Sample 204-1248C-1X-CC (2.38 mbsf). This is probably due to the current position of this site on a topographic high. The sedimentation rate is estimated to be 21 cm/k.y. for the interval from 2.38 to ~40 mbsf and 7 cm/k.y. for the interval from ~40 to 120 mbsf. The age of the bottom of Hole 1248C is estimated to be younger than 1.6 Ma (diatoms) or 1.67 Ma (nannofossils). Therefore, a higher sedimentation rate is suggested for the interval from 120 mbsf to the bottom of the hole, although the precise rate is unknown (Fig. **F11**).

F11. Age-depth plot, p. 35.

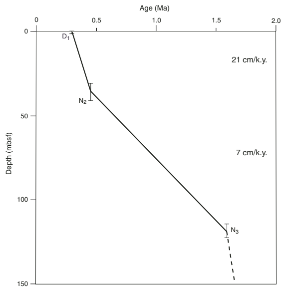

INTERSTITIAL WATER GEOCHEMISTRY

The main objectives of the IW program at this site were to provide geochemical proxies for the presence and abundance of gas hydrate and to establish constraints on the processes responsible for a circular “bright spot” observed on the seafloor reflectivity data (see **“Introduction,”** p. 1). Two holes were cored at Site 1248, and we recovered 33 IW samples at a frequency of approximately two whole-round samples per core in both Holes 1248B (4 samples) and 1248C (29 samples). The IW geochemistry data are tabulated in Table **T4** and are illustrated in Figure **F12.**

T4. Dissolved species in pore waters, p. 66.

Site 1248 was cored to a TD of 149 mbsf (Hole 1248B), just below the depth of the seismic reflector denoted as Horizon A (see **“Introduction,”** p. 1). This horizon lies just below the BSR; thus, the bulk of the IW data obtained at this site lies within the gas hydrate stability zone (GHSZ). The composition of the IW is influenced by gas hydrate geochemistry and by the possible migration of fluids that leads to the accumulation of these hydrate deposits in near-surface sediments. The distribution of dissolved chloride and sulfate provides important clues that can help us unravel gas hydrate dynamics and methane fluxes at this site. The downcore distribution of dissolved constituents in pore fluids can potentially be used to establish the presence and magnitude of upward fluid advection in accretionary margins (e.g., Torres et al., 2002). However, the data collected at Site 1248 cannot be used to quantify vertical flow rates because of the poor recovery of near-surface sediments and consequent low sample resolution. Further uncertainties are introduced by dilution of the pore water by gas hydrate dissociation during core recovery. Although in theory, the chloride data could be used to constrain the amount of freshening during gas hydrate recovery, these estimates are based on assumptions pertaining to the in situ chloride concentration, which in the near-surface sediments at Site 1248 is highly uncertain (see below).

F12. Various dissolved species, p. 36.

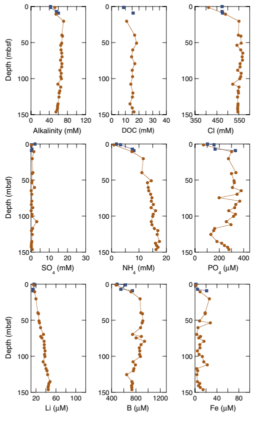

Chloride Concentration and the Presence of Gas Hydrate

The chloride profile at Site 1248 (Fig. **F12**) shows a pronounced anomaly in the upper 20 mbsf, which corresponds to a zone of gas hydrate presence near the seafloor. From 20 mbsf to the BSR (115 mbsf), the chloride distribution is characterized by excursions to lower concentrations superimposed on a linear trend assumed to reflect in situ chloride values. These chloride anomalies reflect dissociation of gas hydrates during recovery and can be used to estimate the amount of gas hydrate present in the sediments when used in conjunction with background in situ chloride data (see **"Interstitial Water Geochemistry,"** p. 13, in the "Explanatory Notes" chapter and **"Interstitial Water Geochemistry,"** p. 13, in the "Site 1244" chapter). We assumed a background concentration defined by the data points that appear to fit a smooth profile at this site, as indicated by the shaded portion of the chloride distribution (Fig. **F13A**). These background values correspond fairly well to the chloride concentrations obtained for Site 888, a site with no evidence of gas hydrate drilled west of the accretionary margin during Leg 146 (Kastner et al., 1995). Gas hydrate was indeed recovered from Site 1248 at depths corresponding to the observed chloride anomalies (Cores 204-1248C-1X, 3X, and 4X) (see **"Lithostratigraphy,"** p. 2). In addition, thermal anomalies seen in IR data (see **"Infrared Scanner,"** p. 15, in "Physical Properties") and variations in the resistivity data (see **"Downhole Tools and Pressure Coring,"** p. 18) also suggest the presence of gas hydrate from the seafloor to the BSR. The percentage of hydrate in the pore space of sediments below 20 mbsf, calculated from the Cl^- anomalies, ranges from 0% to 5%.

F13. Chloride concentration profile, p. 38.

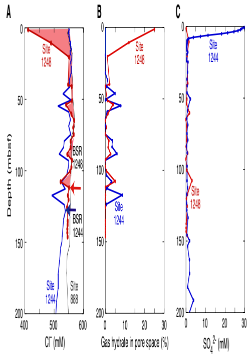

Even though we cannot quantify the advective rate at this site based on IW data (because of the poor recovery in near-surface sediments), a qualitative comparison between Sites 1248 and 1244 is consistent with a much faster rate of methane advection at Site 1248 (Fig. **F13**). The sediments below 40 mbsf at both sites have discrete chloride anomalies that indicate the presence of gas hydrate. However, at Site 1244 the upper sediments (above 40 mbsf) do not contain enough methane to allow for hydrate formation, as revealed by the absence of chloride anomalies (Fig. **F13B**) and the presence of dissolved sulfate in the upper 10 mbsf (Fig. **F13C**). In contrast, at Site 1248 there is abundant hydrate in the near surface and there is no sulfate in the shallowest sample collected at this site (Sample 204-1248B-1H-1, 0–20 cm). We believe that this difference reflects active advection of methane-bearing pore fluids or free gas at this site.

Carbon Cycling

Site 1248 is a locus for carbon cycling through the process of anaerobic methane oxidation (AMO), which occurs in the shallow subsurface. Sulfate concentrations are near zero in the shallowest IW sample (2.2 mM) (Sample 204-1248B-1H-1, 0–20 cm) and remain near zero downhole (Table **T4;** Fig. **F12**). Seawater sulfate and upward-moving methane are co-consumed near the seafloor by a consortium of microbes carrying out AMO:

$$CH_4 + SO_4^{2-} \rightarrow HCO_3^- + HS^- + H_2O$$

(Reeburgh, 1976). AMO typically occurs under diffusive conditions at the sulfate/methane interface (SMI) (for a discussion see **"Interstitial Water Geochemistry,"** p. 13, in the "Site 1244" chapter). However, because at Site 1248 methane is delivered by advection of water and/or free gas, typical biogeochemical zones (e.g., Froelich et al., 1979) are not present and sulfate reduction of sedimentary organic matter may decrease in importance. AMO occurring at methane seeps typically creates millimolar quantities of dissolved sulfide in the pore water (e.g., Paull et al., 1995; Sahling et al., 2002; Torres et al., in press). The sulfide concentration in the Leg 204 IW samples will be measured postcruise.

Alkalinity is anomalously high in the upper tens of meters of Site 1248 as compared to nonseep locales such as Site 1244 (Table **T4;** Fig. **F12**). Alkalinity increases rapidly with depth as methane carbon, delivered to the shallow subsurface by advection, is converted to dissolved carbon dioxide (ΣCO_2) by AMO. High interstitial alkalinity also promotes carbonate deposition and likely explains authigenic calcium carbonate observed in the sediment (see **"Lithostratigraphy,"** p. 2).

Major and Minor Element Distributions

Consistent with the depletion of sulfate throughout the core, the pore waters at this site have large dissolved barium concentrations. The dotted line in the barium distribution (Fig. **F14**) reflects the estimated in situ content, which reaches levels as high as 43 µM in Sample 204-1248B-1H-1, 0–20 cm, after correcting for dilution resulting from gas hydrate dissociation. These levels are much higher than the bottom seawater concentration, which at this site is ~9×10^{-2} µM (M. Torres, unpubl. data). The presence of dissolved sulfate in the pore fluids constitutes a barrier to dissolved barium transport because barium precipitates as solid barite ($BaSO_4$) in these horizons. Figure **F14** illustrates the difference in the barium distributions between Sites 1244, where there is sulfate in the upper 10 mbsf, and Site 1248, where fluid transport has depleted the sulfate even in the uppermost sample recovered at this site. At locations where advective flow results in transport of sulfate-depleted barium-rich fluids to the seafloor, barium is released to the bottom water (Torres et al., 1996, 2002). At Hydrate Ridge, large barium fluxes have been measured with benthic instrumentation (M. Torres, unpubl. data; Tryon et al., 2002), which is consistent with the observations obtained by drilling at this site.

F14. Interstitial sulfate and barium, p. 39.

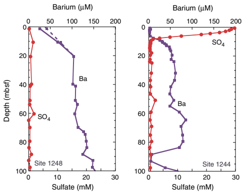

The advection of methane likely influences the carbonate geochemistry at this site. The sediments in lithostratigraphic Unit I (0–39 mbsf) contain small carbonate nodules, an authigenic phase that was not observed at the other sites drilled during this leg (see **"Lithostratigraphy,"** p. 2). The dissolved boron distribution at this site shows an increase in the upper 50 mbsf (Fig. **F15**). The excursions to lower boron values superimposed on this trend reflect dilution of the boron signal by hydrate dissociation. It is possible that the boron increase reflects an aragonite-to-calcite transformation (see **"Interstitial Water Geochemistry,"** p. 13, in the "Site 1244" chapter). Although the magnitude of the boron maximum at Site 1248 is similar to that observed at Site 1244, the dissolved strontium profiles are different between these two sites. Whereas no significant increase in Sr^{2+} was observed at Site 1244, at Site 1248, the dissolved strontium distribution parallels the boron profile, suggesting a stronger involvement of this element in carbonate diagenetic processes. Postcruise analyses of the carbonate fraction will

F15. Interstitial dissolved boron and strontium concentrations, p. 40.

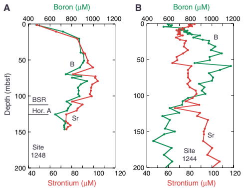

enhance our understanding of the diagenetic processes associated with the carbon cycle on Hydrate Ridge. This is particularly significant at Site 1248, where advection of methane-rich fluids is probably responsible for the presence of scattered carbonates on the seafloor and within the sediments.

ORGANIC GEOCHEMISTRY

Site 1248 is located within a prominent "bright spot" on deep-towed side-scan sonar seafloor reflectivity and a wipe-out zone on 3-D seismic data near the crest of southern Hydrate Ridge (see **"Introduction,"** p. 1). The shipboard organic geochemistry program for Holes 1248B and 1248C included analyses of hydrocarbon gases, carbonate carbon (IC), organic carbon (OC), total sulfur (TS) and total nitrogen (TN) content, and Rock-Eval characterization. A description of the methods used is summarized in **"Organic Geochemistry,"** p. 16, in the "Explanatory Notes" chapter.

Hydrocarbon Gases

The levels of methane (C_1), ethane (C_2), ethylene ($C_{2=}$), and propane (C_3) remaining in cores were measured using the headspace technique. The results are reported in Table **T5** and plotted as parts per million by volume (ppmv) of gas components vs. depth in Figure **F16.** Methane content is anomalously high near the seafloor, reaching 29,000–38,000 ppmv in the shallowest samples at 0.05–1.5 mbsf. The concentration of ethane is very high (46–63 ppmv) in the shallowest samples, decreases between ~40 and 100 mbsf, and increases to several hundreds of ppmv at depths below ~100 mbsf. Ethylene is present sporadically at trace levels (0.4–0.9 ppmv) throughout the depth interval cored. Propane is present in relatively high concentrations (tens of ppmv) in the upper section (0–120 mbsf) and is even more abundant (hundreds of ppmv) in headspace gas below 120 mbsf (Table **T5;** Fig. **F16**). The anomalously high concentrations of hydrocarbon gases near the seafloor indicate that Site 1248 is located in a highly advective fluid-flow setting. This interpretation is further supported by the presence of gas voids and gas hydrate in shallow sediments and pore water characteristics such as the absence of dissolved sulfate (see **"Carbon Cycling,"** p. 10, in "Interstitial Water Geochemistry").

Gas voids in cores are found as shallow as 1 mbsf. The composition of gas samples from voids or expansion gaps in the core liner are listed in Table **T6.** The void gas (vacutainer) samples are relatively pure methane, generally with minimal air contamination. Contents of methane in the voids are generally >900,000 ppmv (>90% by volume) unless diluted by air (Fig. **F17**). In the upper ~100 mbsf, ethane contents of void gas show a gradual decrease with depth, from ~1300–1700 ppmv near the seafloor to ~140 ppmv in the interval around 90 mbsf. Beneath 90–100 mbsf, the ethane contents increase abruptly to a range of 13,000–17,000 ppmv (Fig. **F18**). This order-of-magnitude increase in the relative ethane content below ~100 mbsf is also apparent in the headspace gas analyses. These trends are probably related to the migration of thermogenic hydrocarbons along relatively permeable zones near Horizon A (~128–132 mbsf) and may also be influenced by the formation and decomposition of gas hydrate (Fig. **F17**). The exact mechanism producing such relative ethane enrichment is still being investigated.

T5. C_1, C_2, $C_{2=}$, and C_3, p. 67.

F16. C_1, C_2, and C_3, p. 41.

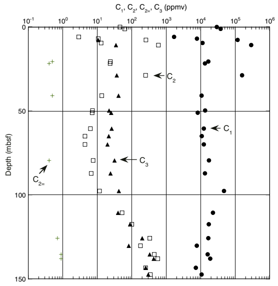

T6. Light hydrocarbon and non-hydrocarbon gases, p. 68.

F17. C_1, C_2, C_3, *i*-C_4, and *n*-C_4, p. 42.

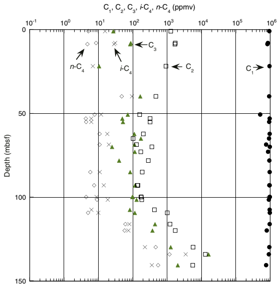

F18. Light hydrocarbons, p. 43.

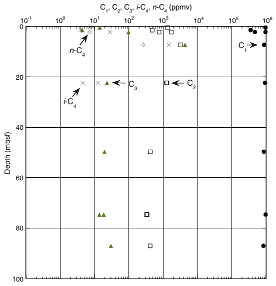

Propane contents in void gas range from 10.5 to 100.9 ppmv in the upper 100 mbsf and abruptly increase to >16,000 ppmv at ~135 mbsf. Isobutane and normal butane are present throughout the interval cored, and their concentrations also significantly increase below ~100 mbsf (Table T6; Fig. F17). Moreover, pentanes and hexanes, which are not present in the upper section, are present in the interval around ~135 mbsf (Table T6). The presence of C_{5+} hydrocarbons indicates the migration of thermogenic gases from greater depth. The prominent seismic reflection, Horizon A, which is composed of sand and silt (including volcanic ash components), may serve as a major migration pathway that facilitates fluid flow from the deeper subsurface into the shallow sediment.

Gas compositions expressed as the C_1/C_2 ratio of headspace and void gas are plotted vs. depth in Figure F19. The C_1/C_2 ratios for both headspace and void gas show a systematic increase from the seafloor to ~100 mbsf and then decrease to ~130 mbsf. This anomalous trend may reflect the mixing of gases from three hydrocarbon pools: (1) ethane-enriched mixed microbial and thermogenic gas near the seafloor, (2) ethane-depleted microbial gas at ~100 mbsf, and (3) ethane-enriched mixed microbial and thermogenic gas apparently migrating near Horizon A at ~130 mbsf. The observed C_1/C_2 gradient is inconsistent with predominantly vertical migration of ethane-enriched hydrocarbon gases to the seafloor through the cored interval. Instead, our interpretation suggests that the near-seafloor ethane-enriched gases may have migrated from the area of most active gas flux along shallow lateral stratigraphic or structural pathways. Alternatively, the observed trend of the C_1/C_2 ratios may reflect the processes of gas hydrate crystallization in the subsurface.

F19. C_1/C_2 ratio vs. depth, p. 44.

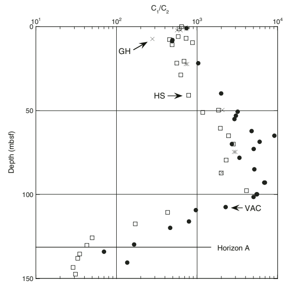

When C_1/C_2 ratios of the void gas are plotted vs. temperature (Fig. F20), the C_1/C_2 trend falls within the "anomalous" field, both near the seafloor and at depths greater than ~100 m. This suggests the possibility that migrated thermogenic hydrocarbons, probably associated with overpressured oil and gas reservoirs, may be present below the cored interval (Pimmel and Claypool, 2001). The C_1/C_2 ratio of void gases was found to be as low as 70 and that of headspace gases as low as 29 (i.e., well beyond the suggested limit of the anomalous field). Based on hydrocarbon monitoring data, Hole 1248C was abandoned at 149.0 mbsf to minimize the possible risk of blowouts and/or petroleum spills.

F20. C_1/C_2 ratio vs. temperature, p. 45.

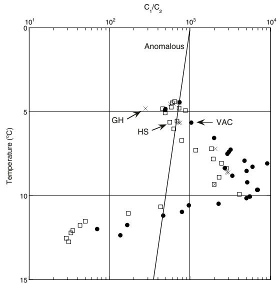

Gas Hydrate

Gas hydrate veins, nodules, and gas hydrate–cemented sediments were recovered from cores on the catwalk. At Site 1248, 11 samples of gas hydrates were decomposed and the gas hydrate–bound gases were analyzed (Table T7). Most gases are relatively pure methane, with minimal air contamination. Two samples from the shallowest cores contain relatively high concentration of H_2S (25 and 11,812 ppmv). However, these samples also contained a significant amount of surrounding sediment, which may have caused the presence of H_2S. Similarly, propane and butanes measured in most gas hydrate samples are probably present in associated sediments.

T7. Light hydrocarbon and nonhydrocarbon gases in gas hydrates, p. 69.

Two clean (minimal contamination from sediment) pieces of gas hydrate were decomposed for geochemical analysis (Table T7). One sample contains only methane and ethane, suggesting that gas was derived from Structure I gas hydrate. The other sample contains high concentrations of propane ($C_3 > C_2$) and butanes, suggesting the possibility of Structure II gas hydrate. Although thermogenic Structure II gas hydrates are common in petroleum basins such as the Gulf of Mexico (Sassen et al., 2001) and the Caspian Sea (Ginsburg and Soloviev, 1998), only Structure I methane hydrates were found at Hydrate Ridge prior to ODP Leg 204 (Gutt et al., 1999).

The C_1/C_2 ratios for gas hydrate–bound gas show the same trend as void gases (Fig. F19). However, most gas hydrate samples are slightly enriched in ethane relative to void gases from adjacent depths.

Carbon Analyses, Elemental Analyses, and Rock-Eval Characterization

A total of 13 sediment samples were analyzed for IC, total carbon (TC), OC (by difference), TN, and TS. The results are reported in Table T8. IC content, plotted against depth of burial in Figure F21, varies from 0.15 to 2.46 wt% (average = 0.66 wt%). The greatest concentration of IC at 1.16 mbsf correlates well with the carbonate-rich patch described in "Lithostratigraphy," p. 2. The relatively high concentration of IC at the base of the cored section is related to the presence of calcareous fossils. When calculated as $CaCO_3$, the carbonate contents in the sediments vary from 1.13 to 20.49 wt% (Fig. F21).

T8. IC, OC, TN, and TS, and C/N ratios, p. 70.

F21. IC, OC, TN, and TS, p. 46.

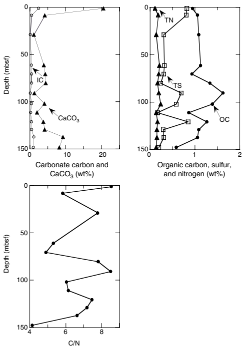

OC content of sampled intervals (Table T8; Fig. F21) ranges from 0.58 to 1.62 wt% (average = 1.10 wt%). The analyzed sample with the highest OC content is at 90.86 mbsf, where the concentration of IC is lowest in the section. The C/N ratios are <10. Based on the C/N ratios, OC in the sediments is predominantly of marine origin.

TN in the sediments varies consistently between 0.11 and 0.23 wt%. (Table T8; Fig. F21). The nitrogen data show no apparent trends vs. either depth or OC content. The sediment samples have TS contents ranging from 0.17 to 0.82 wt% (Table T8; Fig. F21) and show a consistent relationship between sulfur and OC.

The results of Rock-Eval pyrolysis of selected samples are given in Table T9. This analysis was performed in part to evaluate the possible presence of migrated liquid hydrocarbons. Although the production index values seem moderately elevated (i.e., >0.1), they are fairly typical for continental margin sediments cored by ODP. There is no correlation between increased C_{2+} gas components and higher production index values and no definitive evidence for oil staining.

T9. Rock-Eval pyrolysis, p. 71.

PHYSICAL PROPERTIES

Two holes were drilled at Site 1248 and sediments from them were analyzed for physical properties. Hole 1248B consists of three cores, but only Cores 204-1248B-1H and 2H were analyzed (Core 3H was too short for physical property analysis). Hole 1248C was cored to a TD of 148.5 mbsf, but in the upper 50 mbsf, recovery was <25% and only five dispersed sections out of this interval were recovered and were available for physical property analyses. Standard IR imaging was performed on all sections recovered, and these images were used for identification of cold-spot anomalies associated with the presence of hydrate. Physical property measurements were performed on whole-round core sections, and discrete samples were taken for moisture and density (MAD) analyses from the working half of the split core sections (see **"Physical Properties,"** p. 22, in the "Explanatory Notes" chapter).

Infrared Scanner

IR imaging of cores recovered at Site 1248 provided on-catwalk identification of hydrate zones in each core as described in **"Physical Properties,"** p. 24, in the "Site 1244" chapter and **"Physical Properties,"** p. 22, in the "Explanatory Notes" chapter). This information was used to facilitate hydrate sampling and preservation as applied to all cores from this site.

Most of the hydrate detectable by IR imaging at this site (50%) is present as disseminated layers. However, an unusually high percentage of hydrate appears as nodular textures in the IR images (26%). Veins or layers account for 25% of IR-detected hydrate. No thick zones of concentrated hydrate were detected. Poor recovery in the upper 48 mbsf of Holes 1248B and 1248C prevented direct observation of high concentrations of hydrate as estimated from LWD data (see **"Downhole Logging,"** p. 19). However, the core that was recovered in the upper 48 mbsf exhibited extensive cold anomalies even in partially filled core liners, a result typical of disrupted or dissociated hydrate and consistent with poor recovery in a zone of abundant hydrate.

Typical hydrate thermal anomalies are shown in Figure **F22**, including examples of the nodular texture that is relatively abundant in Hole 1248B. The IR thermal anomalies from this site are cataloged in Table **T10**, and a qualitative interpretation of the hydrate texture is provided for each anomaly. An example of the size and geometry of hydrate nodules detectable by IR is illustrated in Figure **F23**. Two IR scans of anomaly IR117 (Table **T10**) taken ~19 min apart show a ΔT of 5.5°C in the first scan and ~1°C in the second scan. The second scan has also developed a warm spot at the center of the anomaly that is interpreted to be a void developing where hydrate previously existed. The archive half of the split core clearly shows a small area of mousselike texture, ~2.5 cm in diameter, associated with the hydrate. The hydrate did not fully penetrate the core, and the disrupted zone (or IR anomaly) is consistent with a variety of shapes, including spherical, cylindrical, or blade shaped.

Circular-shaped anomalies in Hole 1248C suggest a spherical shape for these nodules; if they were commonly blade shaped, a larger number of oblate shapes would have been observed. Figure **F23** also illustrates that a spherical nodule of hydrate 2 cm in diameter in the center of a core would probably exhibit the IR signature of disseminated hydrate because low-temperature hydrate would not be in direct contact with the core liner. Thus, thermal anomalies classified as "disseminated" may represent a range of hydrate textures, from a single nodule in the center of a core to distributed particles of millimeter-size hydrate grains to dispersed pore-filling hydrates present on the submillimeter to micrometer scale. Such anomalies are not veins or layers large enough to transect the core or nodules larger than a few centimeters because these features would show up as well-defined large ΔT anomalies.

Successive thermal images were used to produce a downcore thermal log for each core recovered at Site 1248 (Fig. **F24**). The logs show the overall thermal structure of each core. The dominant features identified in the thermal logs are cold anomalies for the limited amount of core recovered in the upper 16 and 48 m in Holes 1248B and 1248C, respectively, and relatively abundant discrete cold anomalies from 48 to 124

F22. Hydrate IR thermal anomalies, p. 47.

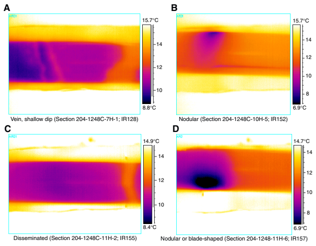

A: Vein, shallow dip (Section 204-1248C-7H-1; IR128)
B: Nodular (Section 204-1248C-10H-5; IR152)
C: Disseminated (Section 204-1248C-11H-2; IR155)
D: Nodular or blade-shaped (Section 204-1248-11H-6; IR157)

T10. Presence of gas hydrate based on IR images, p. 72.

F23. IR images, p. 48.

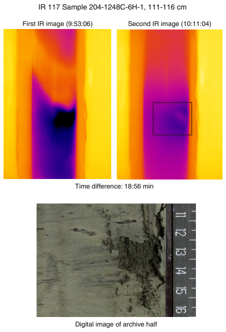

F24. Downhole temperature, p. 49.

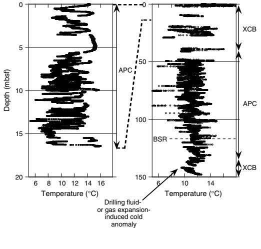

mbsf in Hole 1248C. Cold anomalies are observed below the BSR for ~5 m. Minor cold anomalies below 124 mbsf are only present at the top of individual cores and are explained by the impact of drilling fluid in the deeper parts of the hole or perhaps by gas expansion or exsolution. This phenomenon is well documented by the IR temperature data and is most common for XCB cores (see **"Physical Properties,"** p. 19, in the "Site 1251" chapter). Results from Hole 1248C indicate that cold core tops can also be present with APC coring. The IR temperature anomalies are plotted as a function of depth in Figure **F25.** These results demonstrate that the distribution of hydrate is consistent with LWD pore water saturation (S_w) data (Fig. **F25**) (also see **"Downhole Logging,"** p. 19).

F25. IR thermal anomalies with S_w, p. 50.

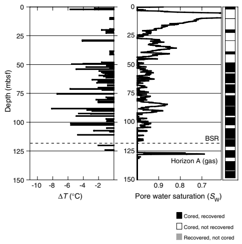

The presence of gas hydrate 5 m below the BSR may be within the combined uncertainty of the BSR depth and core depth. However, if we take the available depths at face value, the lower two IR anomalies fall below the GHSZ, as inferred from seismic (BSR depth estimated at 119 mbsf) and LWD data (estimate based on Archie saturation at 118 mbsf). They fall within the stability zone of hydrates of higher molecular weight hydrocarbons (see **"Organic Geochemistry,"** p. 12) and within the methane/seawater/hydrate stability zone predicted by in situ temperature measurement (129 mbsf) (see **"Downhole Tools and Pressure Coring,"** p. 18). Considering that there may be a 4-m mismatch between the cored hole and the LWD hole (Fig. **F26**), it is premature to conclude that these two IR anomalies were present below the methane hydrate stability zone, but it is possible.

F26. Physical properties, p. 51.

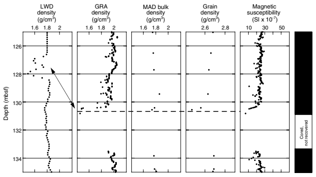

Sediment Density from Multisensor Track and Moisture and Density

Poor core recovery resulted in only sparse physical property data from the upper 50 mbsf in Holes 1248B and 1248C. Bulk density values increase with depth from ~1.6 g/cm³ at the seafloor to ~1.75 g/cm³ at 150 mbsf (Table **T11;** Fig. **F27**). A notable feature at this site is Horizon A, which is identified from the seismic data at ~128 mbsf. Logging data indicate a large decrease in sediment density at this depth (Figs. **F26, F27**), which is inferred to be associated with sand/ash layers described in the core descriptions (see **"Lithostratigraphic Subunit IIIA,"** p. 4, in "Lithostratigraphic Units" in "Lithostratigraphy"). However, this interval was not fully recovered in the cores. The GRA density data do indicate a decrease in density around this interval, but there is a depth discrepancy of ~4 m for the top of Horizon A between the LWD and GRA density measurements. This discrepancy may be explained by uncertainties associated with the coring depth and the poor core recovery. The 4-m discrepancy may also be caused by structural offset between Holes 1248A and 1248C. The poor core recovery in the interval around Horizon A did not allow high-resolution sampling for MAD analyses, and the few data points available do not indicate a prominent change in the bulk density. There are two data points in this interval that show reduced grain densities, possibly associated with the ash layers. The interpretation of the low-density ash layer as the major cause of Horizon A is consistent with the reversed polarity nature of this seismic reflector, which is reinforced by the presence of free gas trapped in this layer.

T11. MAD values, p. 73.

F27. LWD, GRA, MAD, grain density, and MS, p. 52.

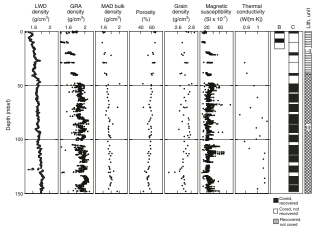

The boundary between the lithostratigraphic Units I-II and III is defined at 39 mbsf (see **"Lithostratigraphy,"** p. 2). Because of poor core recovery, few density data from the multisensor track (MST) or MAD analyses are available for correlation to the lithostratigraphic units.

Magnetic Susceptibility

The MS data below 50 mbsf do not show large variability. Data values range between 20 and 60 × 10^{-7} SI, which are relatively low compared to other sites. Within lithostratigraphic Unit III (39–150 mbsf), the interval between 105 and 125 mbsf shows slightly higher variability in the MS record. These variations were correlated to the presence of sand layers (see **"Lithostratigraphy,"** p. 2).

Non Contact Resistivity System

The Non Contact Resistivity (NCR) system was fully implemented at this site as part of the MST measurements and worked well. In particular, it proved to be very stable (i.e., very little drift between sections). Despite the fact that the sensor system was working well, it only shows that the data are dominated by the effect of abundant cracks caused by gas expansion. This cracking results in apparently high and very variable resistivity values (Fig. **F28**), which although representative of the sediment in the core does not accurately represent the in situ lithologies. A close inspection of the two cores recovered in Hole 1248B at a depth above 10 mbsf (where gas expansion is less strong) does show detailed downcore variation of resistivity values ranging between 0.5 and 1.5 Ωm, which reflect subtle but real lithologic variations. This demonstrates the potential use of the NCR system for fluid-saturated core sections.

F28. NCR, p. 53.

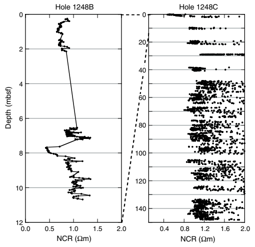

Compressional Wave Velocity from the Multisensor Track and Hamilton Frame Velocimeter

Because of the extensive gas-expansion effect, compressional (*P*)-wave velocities (V_P) could not be measured with the MST; no measurements were possible with the Hamilton Frame velocimeter either.

Thermal Conductivity

Only a limited number of measurements were conducted to determine thermal conductivity values at this site because of the extensive gas expansion cracks (Table **T12;** Fig. **F27**). In general, the measured values are slightly higher than those reported from the other sites, with an average value of 0.99 W(m·K). As a result of the limited number of measurements, no correlation to other physical properties was performed.

T12. Thermal conductivity values, p. 74.

Shear Strength

No measurements with the hand-held Torvane were conducted at this site because of extensive gas expansion cracks.

Special Hydrate Dissociation Experiment

Section 204-1248C-4X-1, which contained disseminated hydrate, was used to test whether the dissociation of hydrate is detectable by repeated measurements of physical properties using the MST sensors over a time period of several hours. Section 204-1248C-4X-1 was measured five times with the MST and was scanned in the X-ray line scanner (see **"Operations,"** p. 2, in the "Site 1249" chapter) four times during a time period of 160 min. GRA density and MS profiles remained stable with time. However, an analysis of the NCR data shows a response in conductivity over time (see Fig. **F29**). Part of this change could be associated with the increase in core temperature. However, a change of ~10°C, as observed during this experiment, has an effect on the resistivity value of only ~0.1 Ωm. The resistivity values changed by ~0.5 Ωm, on average, in this section over time. Assuming this effect is from the dissociation of small amounts of hydrate, then the best structural model is one where the hydrate is present as veins or veinlets. Disseminated small nodules would have a negligible effect on resistivity upon dissociation.

F29. Gas hydrate dissociation experiment, p. 54.

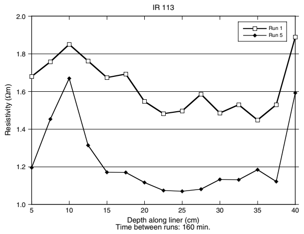

Summary and Discussion

Poor core recovery in both Holes 1248B and 1248C yielded only a limited amount of useful physical property data from Site 1248. No correlation to the lithostratigraphic units was therefore possible. At this site, Horizon A was drilled at a depth of ~128 mbsf. The top of this horizon was recovered, and the MST data show a decrease in the sediment density, which agrees with what was seen in the LWD data. No MS anomaly could be correlated to this horizon. Thermal IR imaging provided a robust and rapid tool for hydrate identification on the catwalk. Post-catwalk processing of thermal anomaly data from the IR images shows a good correlation to the S_w derived from LWD resistivity logs.

DOWNHOLE TOOLS AND PRESSURE CORING

Downhole Temperature Measurements

Six in situ temperature runs were made at this site: three APCT tool, two DVTPP, and one DVTP runs (Table **T13;** Fig. **F30**). APCT data were modeled using the software program TFIT (as described in **"Downhole Tools and Pressure Coring,"** p. 34, in the "Explanatory Notes" chapter) using measured thermal conductivities (see **"Physical Properties,"** p. 14). The DVTP data were modeled using the software program CONEFIT. Temperatures for the DVTPP runs were measured directly from the data because the longer time taken for this measurement results in temperatures that appear to have reached equilibrium. Neither of the DVTPP time series shows the frictional pulse that is expected when the temperature probe is extracted, suggesting poor coupling to the sediment, and the deeper measurement shows an anomalous increase in temperature with time after the initial temperature decay. The shallowest APCT tool measurement shows an anomalous extraction pulse.

The resulting temperature estimates are given in Table **T13** and shown in Figure **F31.** Excluding the deeper DVTPP measurement and the APCT tool measurement, the data suggest a temperature gradient of ~0.056°C/m and a depth to the base of the GHSZ of 130 mbsf. The apparent mismatch of ~20 m between the observed BSR depth of ~115 mbsf and the depth calculated from the temperature data, assuming a pure methane/seawater system, is similar to that observed at other sites.

T13. Temperature measurements, p. 75.

F30. Temperature time series, p. 55.

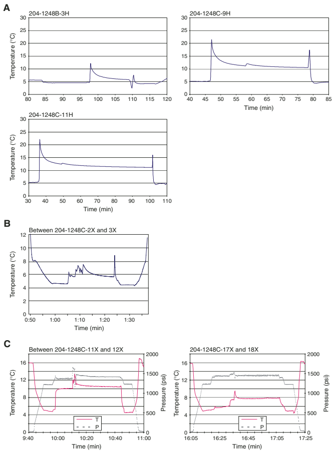

F31. Estimated temperature, p. 56.

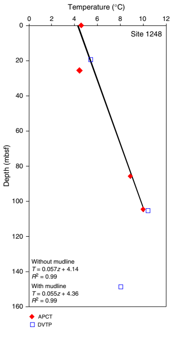

In Situ Pressure Measurements

No in situ pressure measurements were made at this site.

Pressure Core Sampler

No pressure core sampler cores were taken at this site.

HYACINTH Pressure Core Sampler

No HYACINTH pressure cores were taken at this site.

DOWNHOLE LOGGING

Logging While Drilling

Operations

LWD operations at Site 1248 began with the spudding of Hole 1248A at 0530 hr Universal Time Coordinated (UTC) on 21 July 2002 at a water depth of 843.00 meters below rig floor (mbrf) (drillers depth) near the crest of southern Hydrate Ridge. Drilling proceeded at reduced penetration rates of 15 m/hr and lower fluid circulation rates of 15 strokes per minute (spm) to minimize formation washout at shallow depths below seafloor. No real-time MWD or Nuclear Magnetic Resonance (NMR-MRP) tool data were recorded over this interval, as the pump rate was insufficient to activate the turbines in the downhole tools. The penetration rate was increased to ~25 m/hr and fluid circulation was returned to more normal levels at a bit depth of 30 mbsf to TD (194 mbsf), and real-time MWD and NMR-MRP data were recorded. The LWD tools were pulled to ~60 m clear of the seafloor at 1500 hr on 21 July for a dynamic positioning move to Site 1249. The total bit run took ~10 hr.

F32. Quality control LWD logs, p. 57.

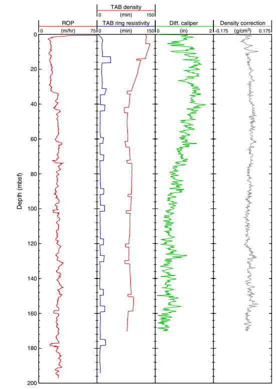

Logging Quality

Figure F32 shows the quality control logs for Hole 1248A. The planned reduced ROP in the near-surface interval (0–30 mbsf) was only partially successful, with the most notable discrepancy in the upper 5 mbsf of Hole 1248A. Below a depth of ~35 mbsf, higher, more normal ROP values of 25 m/hr (±5 m/hr) were achieved. An ROP of 25 m/hr was sufficient to record one sample per 4-cm interval (~25 samples per meter), which was obtained over 70% of the total section of the hole. With this relatively high sample rate, the quality of RAB images for Hole 1248A is quite high and no significant resolution loss is observed with variation in the ROP (Fig. F33). The increased pump rates below 30 mbsf and an ROP of 25 m/hr yield enhanced NMR-MRP porosity data, with a data sampling resolution of ~1 sample per 15-cm interval.

F33. LWD log data, p. 58.

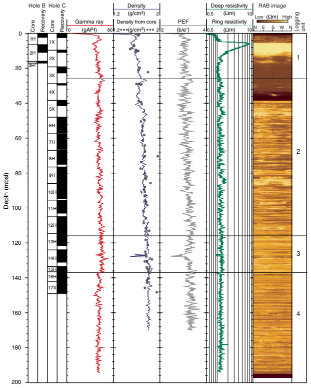

The differential caliper log, which gives the distance between the tool sensor and the wall of the borehole as recorded by the LWD density tool, is the best indicator of borehole conditions. The differential caliper values are <1 in over 70% of the total section in Hole 1248A. Only the uppermost 78 mbsf of the hole contains washouts >1 in. The density correction, calculated from the difference between the short- and long-spaced density measurements, varies from 0 to 0.09 g/cm³ (Fig. F32), which suggests very high quality density measurements. A standoff of <1 in between the tool and the borehole wall also indicates high-quality density measurements, with an accuracy of ±0.015 g/cm^3.

Below ~30 mbsf in Hole 1248A, the time-after-bit (TAB) measurements were 10 ± 5 min for ring resistivity and gamma ray logs and 85 ± 5 min for density and neutron porosity logs (Fig. F32). TAB values remain relatively constant over the interval, coinciding with steady ROP while drilling over most of the hole.

The depths, relative to seafloor, for all of the logs were fixed by identifying the gamma ray signal associated with the seafloor and shifting the log data to the appropriate depth as determined by the drillers pipe tallies. For Hole 1248A, it was determined that the gamma ray log pick for the seafloor was at a depth of 839.0 mbrf. The rig floor logging datum was located 11.0 m above sea level.

Interpretation of Logging-While-Drilling Logs

LWD logs from Hole 1248A show excellent-quality data (Figs. F33, F34). Lower pump rates through the shallow subsurface section greatly reduced the effect of borehole washout on the logs in the near-surface unconsolidated sediments. No sliding tests were conducted to evaluate downhole tool motion at Site 1248. The downhole LWD logs dramatically highlight gas hydrate–bearing sediments as high resistivity anomalies (Fig. F35). Resistivity and density log variations below the hydrate zone may indicate lithologic changes, possibly carbonates, and the presence of free gas. Borehole breakouts, which result from subsurface horizontal stress differences, are observed in the lower portion of the hole.

F34. LWD- and core-derived porosities, p. 59.

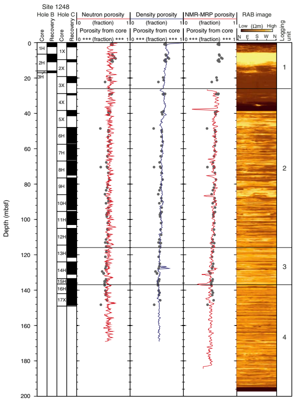

Logging Units

The logged section in Hole 1248A is divided into four "logging units" on the basis of obvious changes in the LWD gamma ray, bulk density, and electrical resistivity measurements (Fig. F33).

Logging Unit 1 (0–26 mbsf) is characterized by a 16-m-thick high-resistivity zone (2–18 mbsf), with a measured peak value >8 Ωm. Logging Unit 1 is also characterized by increasing densities with depth as measured by the LWD tools. However, this trend in the downhole recorded density data is probably due in part to degraded log measurements within the enlarged portion of the near-surface borehole as shown in Figure F32. Logging Unit 1 is within lithostratigraphic Unit I-II (0–39 mbsf), which is described as a dark greenish gray silty clay sequence with abundant sulfide minerals (see **"Lithostratigraphic Unit I-II,"** p. 3, in "Lithostratigraphic Units" in "Lithostratigraphy"). The transition from logging Unit 1 to 2 is defined by a sharp increase in LWD-derived density (from ~1.63 to ~1.75 g/cm^3) and a relatively subtle increase in resistivity (from ~1.1 to ~1.3 Ωm)

F35. Log-derived gas hydrate saturations, Hole 1248A, p. 60.

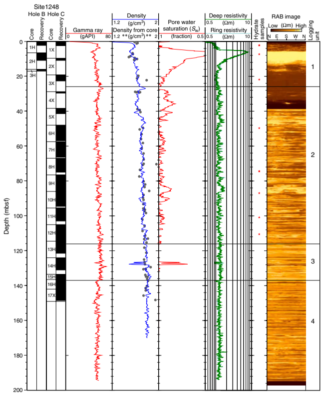

Logging Unit 2 (26–116 mbsf) is characterized by zones of distinct high resistivities, with measured peak values >1.4 Ωm. The gamma ray log in this unit shows a characteristic cyclicity of values that may reflect interbedded silty clay with silt and sand turbidite sequences as described by the shipboard sedimentologists for lithostratigraphic Unit III (39–149 mbsf) (see **"Lithostratigraphic Unit III,"** p. 4, in "Lithostratigraphic Units" in "Lithostratigraphy"). The downhole log-measured density increases with depth in logging Unit 2 (1.65 g/cm^3 at the top to near 1.8 g/cm^3 at the bottom). Neither the RAB resistivity log nor the Vision Neutron Density (VND) tool density log reveals any distinct formation property changes at the expected depth of the BSR. The selection of the boundary between logging Units 2 and 3 at Site 1248 is also complicated by the lack of acoustic transit-time logging data. For Hole 1248A, the calculated Archie-derived water saturation log (Fig. F35), which integrates LWD log-derived density porosities and RAB resistivities, has been used to select the depth of the boundary between logging Units 2 and 3. Thus, the boundary between logging Units 2 and 3 was placed at the base of the deepest logging-inferred presence of gas hydrate (116 mbsf), which corresponds closely to the estimated depth of the BSR at this site.

Logging Unit 3 (116–137 mbsf) correlates with the lower part of lithostratigraphic Unit III (39–149 mbsf), which is described as an interbedded silty clay, silt, and sand turbidite sequence (see **"Lithostratigraphic Unit III,"** p. 3, in "Lithostratigraphic Units" in "Lithostratigraphy"). Logging Unit 3 is generally characterized by more uniform resistivities compared to Unit 2. The transition from logging Unit 3 to Unit 4 is marked by an abrupt drop in gamma ray values (from ~ 65 to 55 American Petroleum Institute gamma ray units [gAPI]) and a more subtle drop in density (Fig. F33), which appears to mark the contact with the deformed sediments of the accretionary complex. A 2-m-thick anomalous interval, characterized by high resistivities (1.3 Ωm) and low densities (<1.5 g/cm^3) is present in logging Unit 3 within the depth interval from ~126 to ~128 mbsf, which suggests the presence of a free gas–saturated sand. This apparent free gas–bearing interval corresponds to seismic Horizon A, which has been mapped regionally (see **"Introduction,"** p. 1).

Logging Unit 4 (137–194 mbsf; TD of Hole 1248A), reflecting the upper portion of the deformed sediments of the accretionary complex, is characterized by almost constant gamma ray and density log measurements with depth.

Resistivity-at-the-Bit Images

The RAB tool produces high-resolution images of the electrical resistivity characteristics of the borehole wall that can be used for detailed sedimentological and structural interpretations. The RAB tool can also be used to make high-resolution electrical images of gas hydrates in the borehole, thus yielding information about the nature and texture of the gas hydrate in sediments. The RAB image in Figure F36 is characterized by light (high resistivity) to dark (low resistivity) bands, which in many cases can be traced across the display. The light continuous high-resistivity bands probably represent gas hydrate occupying low-angle fractures and nearly flat-lying stratigraphic horizons in Hole 1248A.

F36. RAB image, Hole 1248A, p. 61.

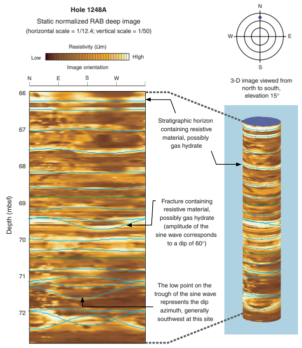

Logging Porosities

Sediment porosities can be determined from analyses of recovered cores and from numerous borehole measurements (see **"Physical Properties,"** p. 22, and **"Downhole Logging,"** p. 43, both in the "Explanatory Notes" chapter). Data from the LWD density, neutron, and LWD-NMR logs have been used to calculate sediment porosities for Hole 1248A. Core-derived physical property data, including porosities (see **"Physical Properties,"** p. 14), have been used to both calibrate and evaluate the log-derived sediment porosities.

The VND LWD log-derived measurements of density in Hole 1248A (Fig. F33) increase with depth and are relatively consistent within logging Units 2 through 4, with values ranging from ~1.65 g/cm^3 near the top of logging Unit 2 to >1.85 g/cm^3 in logging Unit 4. The density log measurements are degraded in logging Unit 1 as discussed above. The LWD log-derived density measurements (ρ_b) from Hole 1248A were used to calculate sediment porosities (ϕ) using the standard density-porosity relation,

$$\phi = (\rho_m - \rho_b)/(\rho - \rho_w).$$

Water density (ρ_w) was assumed to be constant and equal to 1.05 g/cm^3; however, variable core-derived grain/matrix densities (ρ_m) were assumed for each logging density porosity calculation. The core-derived grain densities (ρ_m) in Hole 1248B ranged from an average value at the seafloor of 2.73 g/cm^3 to ~2.68 g/cm^3 at the bottom of the hole (see **"Physical Properties,"** p. 14). The density log-derived porosities in logging Units 2–4 (26–194 mbsf) of Hole 1248A range from ~52% to 67% (Fig. **F34**). However, the density log porosities in logging Unit 1 (0–26 mbsf) are more variable, ranging from 57% to 72%, which is in part controlled by poor borehole conditions.

The LWD neutron porosity log from Hole 1248A (Fig. **F34**) yielded sediment porosities that range from an average value at the top of the logged section of ~65% to about 59% in logging Unit 4. The "total" sediment porosities derived by the NMR-MRP tool in Hole 1248A (Fig. **F34**) ranged from ~65% near the top of logging Unit 2 to about 50% near the bottom of the hole (BOH).

The comparison of core- and log-derived porosities in Figure **F34** reveals that the density- and NMR-MRP–derived porosities are generally similar to the core porosities throughout most of the hole. However, the NMR-MRP porosity log also exhibits numerous low-porosity zones throughout the entire hole, which will be further evaluated after the cruise. The neutron porosities are slightly higher than the core-derived porosities throughout portions of logging Units 2–4 (26–194 mbsf).

Gas Hydrate

The presence of gas hydrate at Site 1248 was documented by direct sampling, with gas hydrate–bearing cores being recovered from both logging Units 1 and 2 (Fig. **F35**). It was inferred, based on geochemical core analyses (see **"Interstitial Water Geochemistry,"** p. 9), IR image analysis of cores (see **"Physical Properties,"** p. 14), and downhole logging data that disseminated gas hydrate is present in portions of logging Units 1 and 2. As previously discussed in **"Downhole Logging,"** p. 43, in the "Explanatory Notes" chapter, the presence of gas hydrate is generally characterized by increases in logging-measured electrical resistivities and acoustic velocities. Logging Units 1 and 2 at Site 1248 are characterized by intervals of high electrical resistivities, but we have no acoustic data (because no wireline logging was conducted at Site 1248) to further evaluate the presence of gas hydrate or free gas at this site.

Resistivity logging data were used to quantify the amount of gas hydrate at Site 1248. For the purpose of discussion, it is assumed that the high resistivities measured in logging Units 1 and 2 are due to the presence of gas hydrate. Archie's Relation,

$$S_w = (aR_w/\phi^m R_t)^{1/n},$$

(see **"Downhole Logging,"** p. 43, in the "Explanatory Notes" chapter) was used with resistivity data (R_t) from the LWD RAB tool and porosity data (ϕ^m) from the LWD density tool to calculate water saturations in Hole 1248A. It should be noted that gas hydrate saturation (S_h) is the measurement of the percentage of pore space in a sediment occupied by gas hydrate, which is the mathematical complement of Archie-derived S_w, with

$$S_h = 1 - S_w.$$

For Archie's Relation, the formation water resistivity (R_w) was calculated from recovered core-water samples, and the Archie a and m variables were calculated by a crossplot technique that compares the downhole log-derived resistivities and density porosities. See Collett and Ladd (2000) for the details on how to calculate the required formation water resistivities and Archie variables. The values used for Site 1248 were $a = 1$, $m = 2.8$, and $n = 1.9386$.

Archie's Relation yielded water saturations (Fig. **F35**) ranging from a minimum value of only ~42% in logging Unit 1 to a maximum of 100% in portions of logging Units 1 and 2 (0–116 mbsf), so calculated gas hydrate saturations in Hole 1248A range from 0% to 58%. The low water saturations shown in logging Unit 3 (Fig. **F35**) probably indicate the presence of free gas–bearing sediments (as discussed above).

REFERENCES

Clague, D., Maher, N., and Paull, C.K., 2001. High-resolution multibeam survey of Hydrate Ridge, offshore Oregon. *In* Paull, C.K., and Dillon, W.P. (Eds), *Natural Gas Hydrates: Occurrence, Distribution, and Detection.* Am. Geophys. Union, Geophys. Monogr. Ser., 124:297–306.

Collett, T.S., and Ladd, J., 2000. Detection of gas hydrate with downhole logs and assessment of gas hydrate concentrations (saturations) and gas volumes on the Blake Ridge with electrical resistivity log data. *In* Paull, C.K., Matsumoto, R., Wallace, P.J., and Dillon, W.P. (Eds.), *Proc. ODP, Sci. Results,* 164: College Station, TX (Ocean Drilling Program), 179–191.

Froelich, P.N., Klinkhammer, G.P., Bender, M.L., Luedtke, N.A., Heath, G.R., Cullen, D., Dauphin, P., Hammond, D., Hartman, B., and Maynard, V., 1979. Early oxidation of organic matter in pelagic sediments of the eastern equatorial Atlantic: suboxic diagenesis. *Geochim. Cosmochim. Acta,* 43:1075–1090.

Ginsburg, G.D., and Soloviev, V.A., 1998. Submarine gas hydrates. *VNIIOkeangeologia* (St. Petersburg), 216.

Gutt, C., Asmussen, B., Press, W., Merkl, C., Casalta, H., Greinert, Y., Bohrmann, G., Tse, J.S., and Hueller, A., 1999. Quantum rotations in natural methane-clathrates from Pacific seafloor. *Europhys. Lett.,* 48:269–275.

Johnson, J.E., Goldfinger, C., and Suess, E., in press. Geophysical constraints on the surface distribution of authigenic carbonates across the Hydrate Ridge region, Cascadia margin. *Mar. Geo.*

Kastner, M., Sample, J.C., Whiticar, M.J., Hovland, M., Cragg, B.A., and Parkes, J.R., 1995. Geochemical evidence for fluid flow and diagenesis at the Cascadia convergent margin. *In* Carson, B., Westbrook, G.K., Musgrave, R.J., and Suess, E. (Eds.), *Proc. ODP, Sci. Results,* 146 (Pt 1): College Station, TX (Ocean Drilling Program), 375–384.

Paull, C.K., Spiess, F.N., Ussler, W., III, and Borowski, W.A., 1995. Methane-rich plumes on the Carolina continental rise: associations with gas hydrates. *Geology,* 23:89–92.

Pimmel, A., and Claypool, G., 2001. Introduction to shipboard organic geochemistry on the *JOIDES Resolution*. *ODP Tech. Note,* 30 [Online]. Available from World Wide Web: <http://www-odp.tamu.edu/publications/tnotes/tn30/INDEX>. [Cited 2002-07-03]

Reeburgh, W.S., 1976. Methane consumption in Cariaco Trench waters and sediments. *Earth Planet. Sci. Lett.,* 28:337–344.

Sahling, H., Rickert, D., Lee, R.W., Linke, P., and Suess, E., 2002. Macrofaunal community structure and the sulfide flux at gas hydrate deposits from the Cascadia convergent margin, NE Pacific. *Mar. Ecol.: Prog. Ser.,* 231:121–138.

Sassen, R., Sweet, S.T., Milkov, A.V., Defreitas, D.A., and Kennicutt, M.C., 2001. Thermogenic vent gas and gas hydrate in the Gulf of Mexico slope: is gas hydrate decomposition significant? *Geology,* 29:107–110.

Torres, M.E., Bohrmann, G., and Suess, E., 1996. Authigenic barites and fluxes of barium associated with fluid seeps in the Peru subduction zones. *Earth Planet. Sci. Lett.,* 170:1–15.

Torres, M.E., McManus, J., Hammond, D.E., de Angelis, M.A., Heeschen, K.U., Colbert, S.L., Tryon, M.D., Brown, K.M., and Suess, E., 2002. Fluid and chemical fluxes in and out of sediments hosting methane hydrate deposits on Hydrate Ridge. *Earth Planet. Sci. Lett.,* 201:525–540.

Torres, M.E., Mix, A.C., Kinports, K., Haley, B., Klinkhammer, G.P., McManus, J., and de Angelis, M.A., in press. Is methane venting at the seafloor recorded by $\delta^{13}C$ of benthic foraminifera shells? *Paleoceanography.*

Tryon, M.D., Brown, K.M., and Torres, M.E., 2002. Fluid and chemical flux at Hydrate Ridge, II. Observations and long-term records reveal insights into dynamic driving mechanisms. *Earth Planet. Sci. Lett.,* 201:541–557.

Figure F1. Bathymetric map showing locations of holes drilled at Site 1248. Bathymetry from EM300 data acquired by Monterey Bay Aquarium Research Institute (MBARI) (Clague et al., 2001).

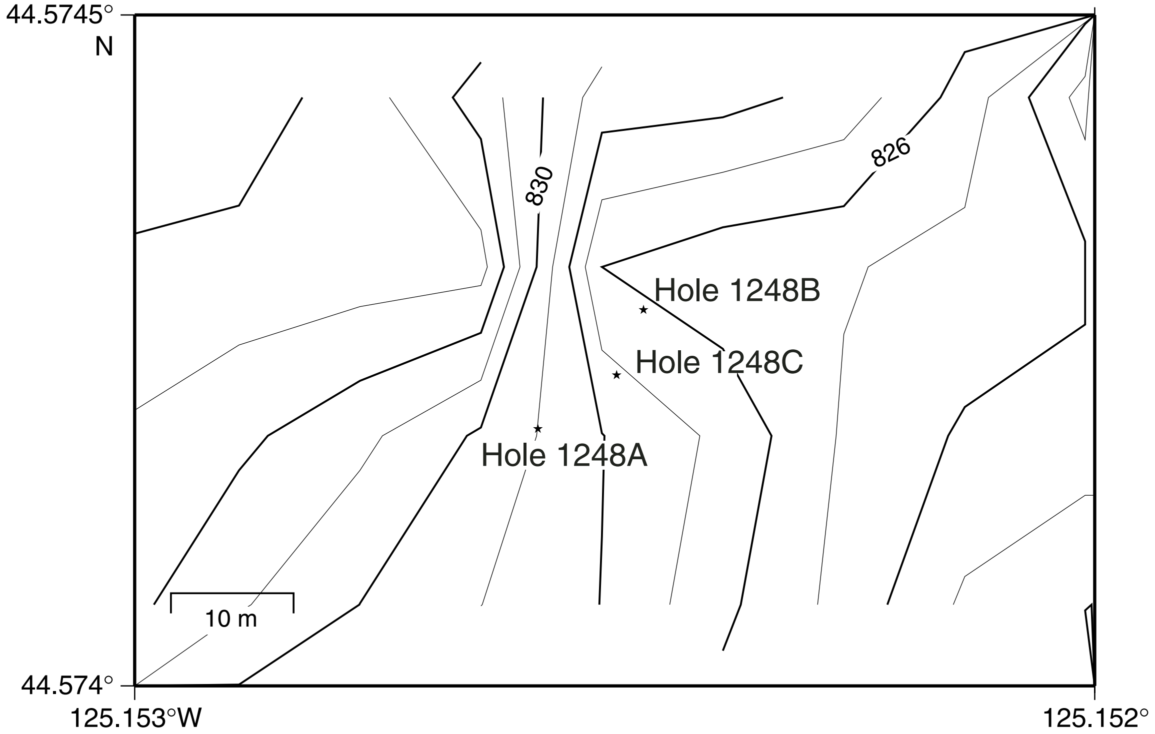

Figure F2. Lithostratigraphic summary for Site 1248.

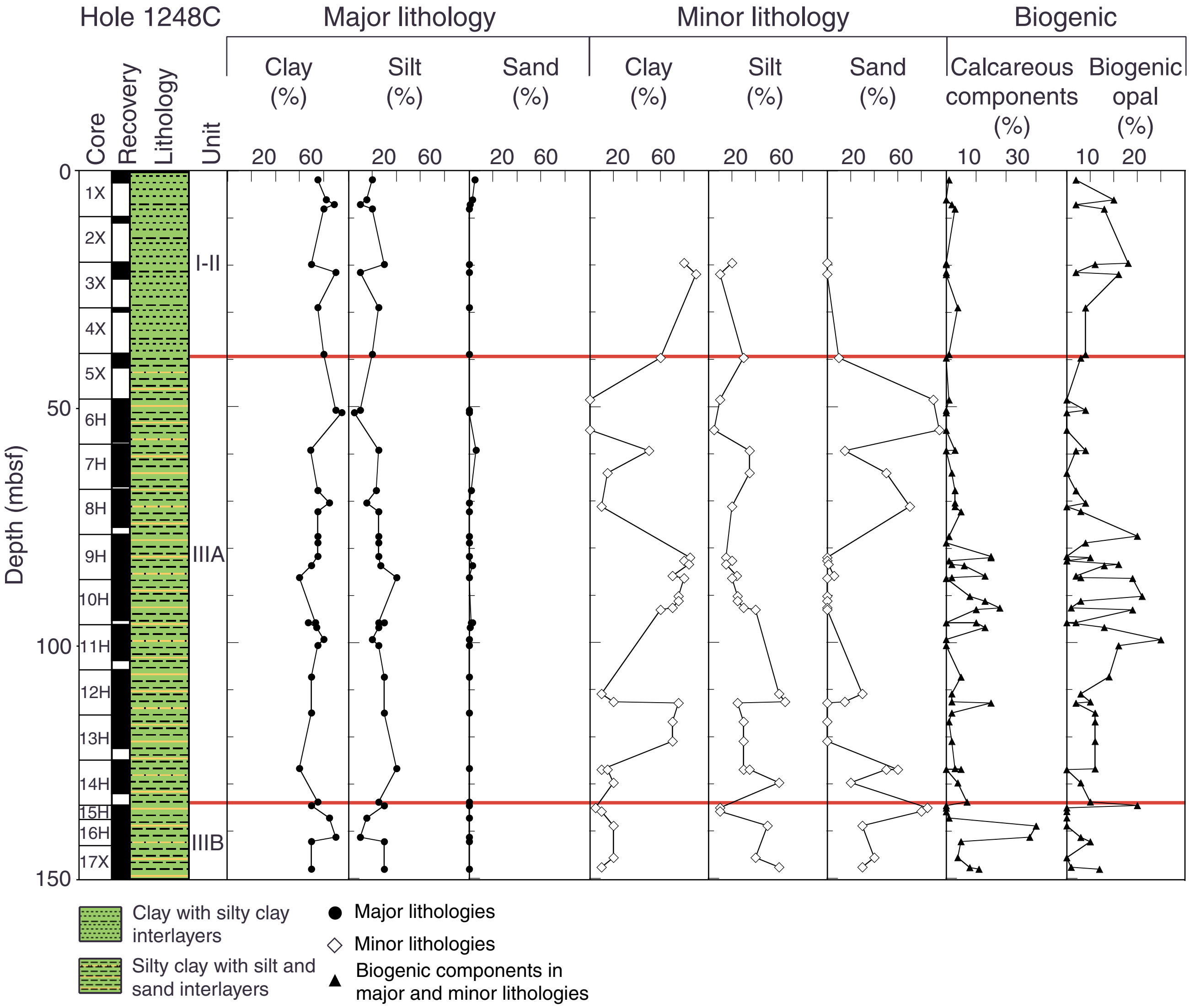

Figure F3. Seismic reflection profile from west (left) to east (right) and LWD data across Site 1248. Lithostratigraphic units and subunits distinguished at Site 1248 are depicted. RAB = resistivity at the bit, BSR = bottom-simulating reflector, SF = seafloor.

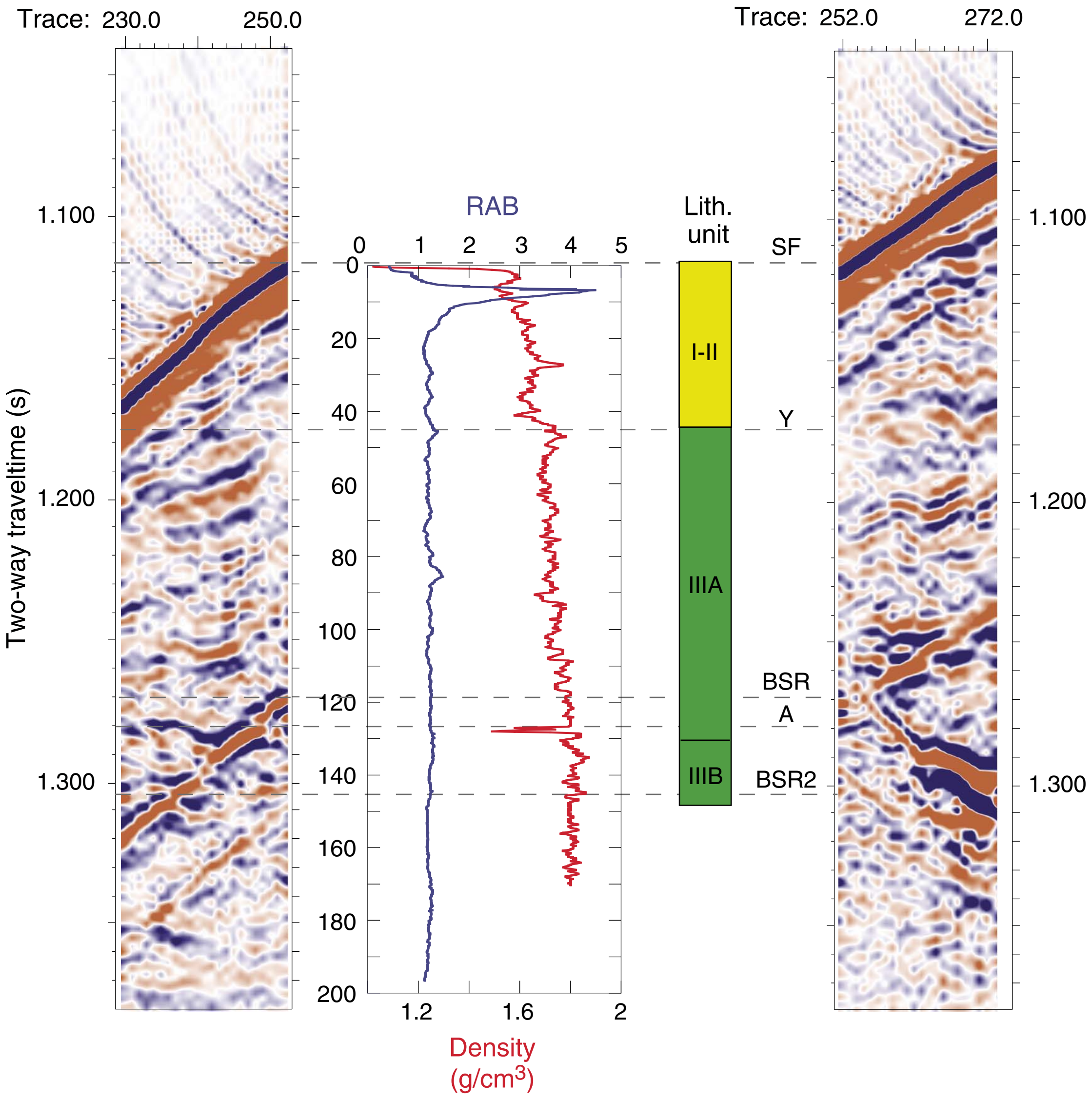

Figure F4. Close-up photographs of sediment textures related to hydrate dissociation in sediments in lithostratigraphic Unit I-II. **A.** Mousselike texture (interval 204-1248B-1H-2, 48–58 cm). **B.** Mousselike texture containing carbonate precipitates and soupy texture at the lower part of the image (interval 204-1248B-1H-2, 66–78 cm).

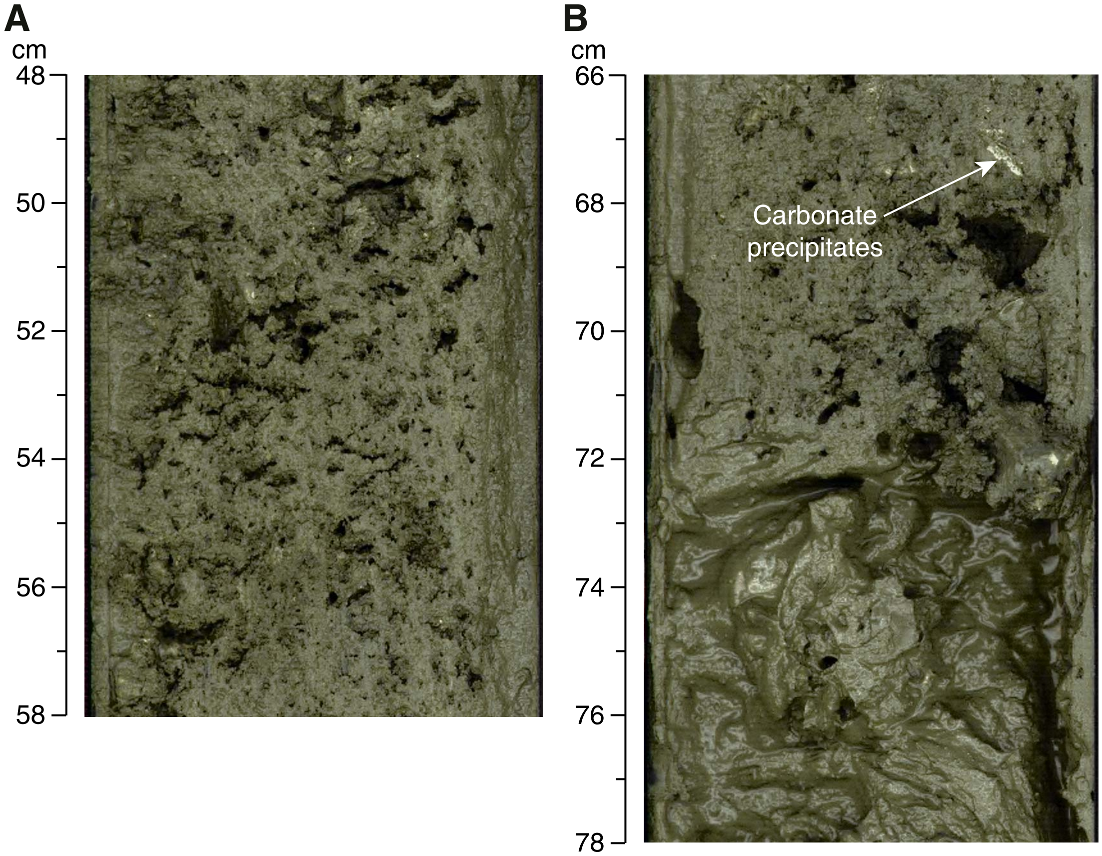

Figure F5. Close-up photographs of (**A**) a carbonate nodule in association with mousselike sediments (interval 204-1248B-1H-1, 100–110 cm) and (**B**) two halves of a 6-cm-long carbonate nodule (interval 204-1248B-1H-02, 0–13 cm). Both samples are found in lithostratigraphic Unit I-II.

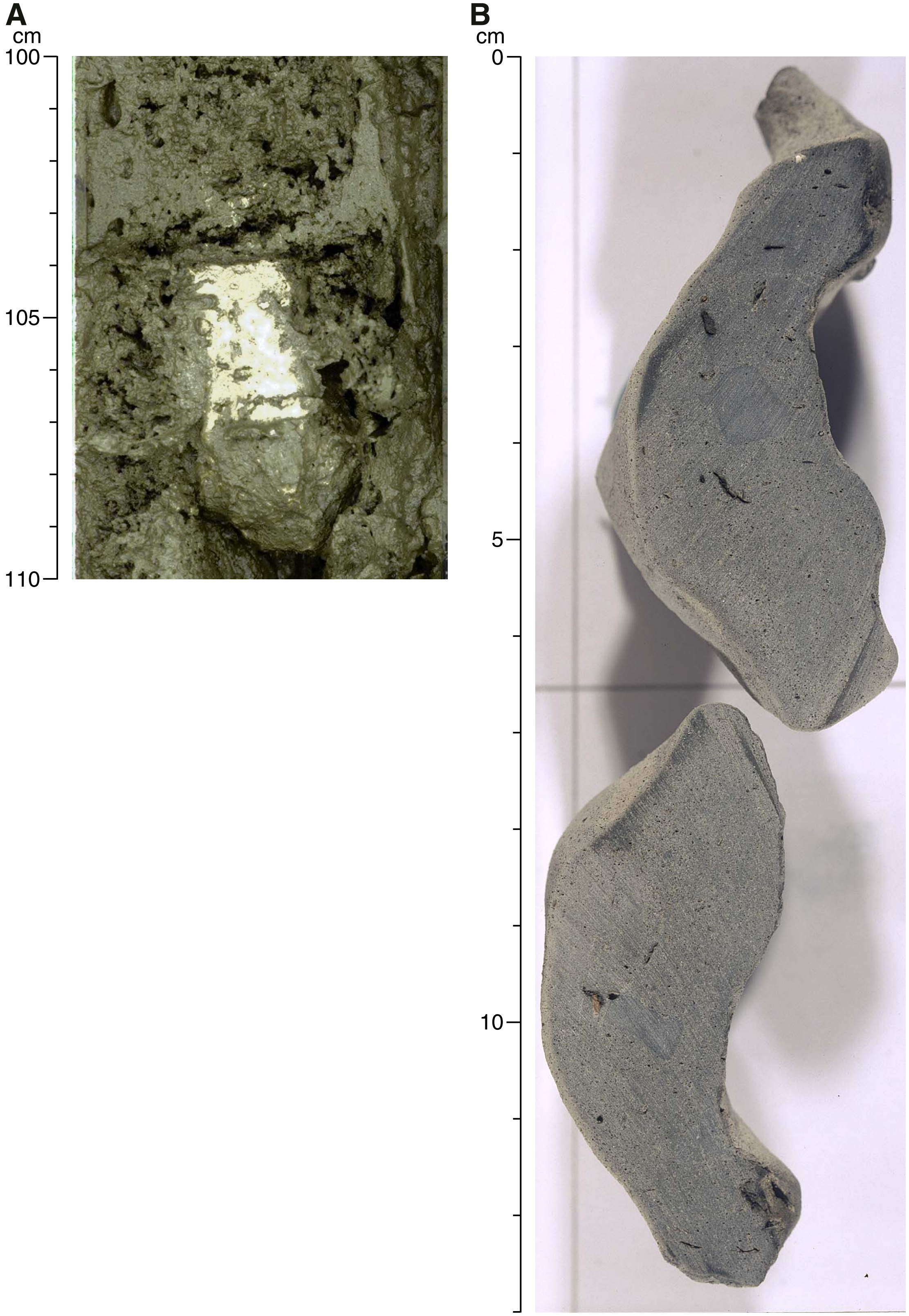

Figure F6. Photomicrograph from a thin section of a carbonate nodule, consisting of micritic carbonate cement with clasts of diverse origin (foraminifers, glauconite, quartz, and opaques). Dashed line = boundary between the coarse- and fine-grained clasts (Sample 204-1248B-1H-2, 10–15 cm).

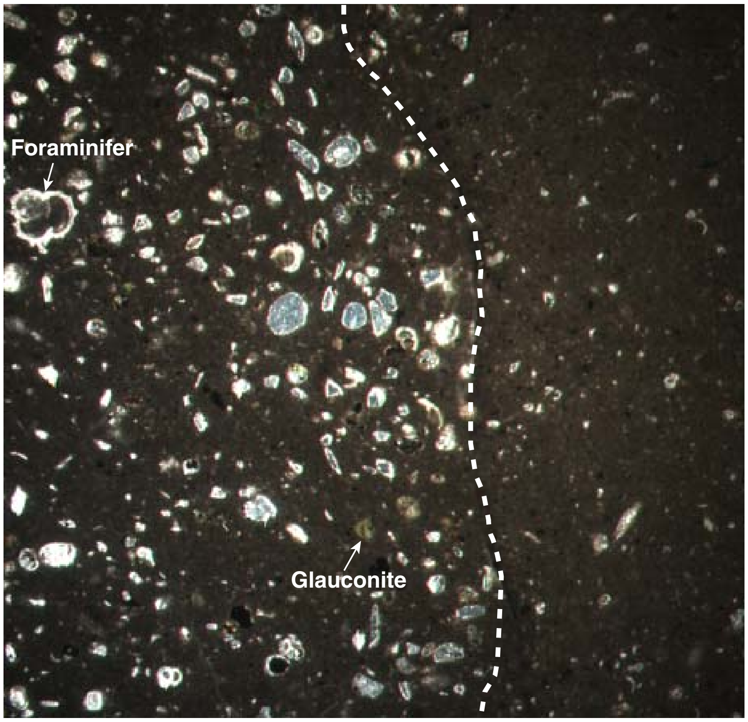

Figure F7. XRD records showing a decrease in calcite with depth in lithostratigraphic Unit I-II. Samples are from Sections (**A**) 204-1248C-1X-1 (1.16 mbsf), (**B**) 204-1248B-1H-2 (1.52 mbsf), (**C**) 204-1248C-2H-3 (8.58 mbsf), (**D**) 204-1248C-3X-2 (21.15 mbsf), and (**E**) 204-1248C-4X-1 (29.05 mbsf).

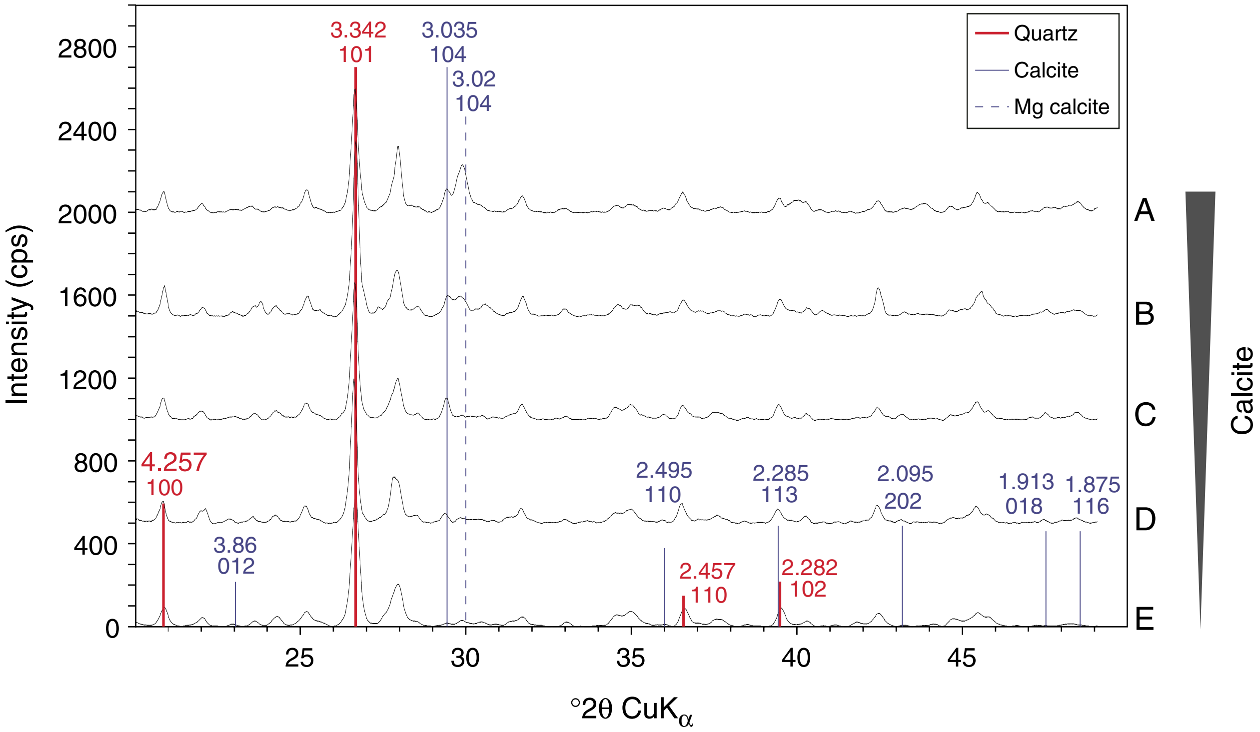

Figure F8. Close up photographs of debris flow deposits from lithostratigraphic Subunit IIIA from intervals (**A**) 204-1248C-9H-5, 7–30 cm, and (**B**) 204-1248C-2H-6, 70–110 cm.

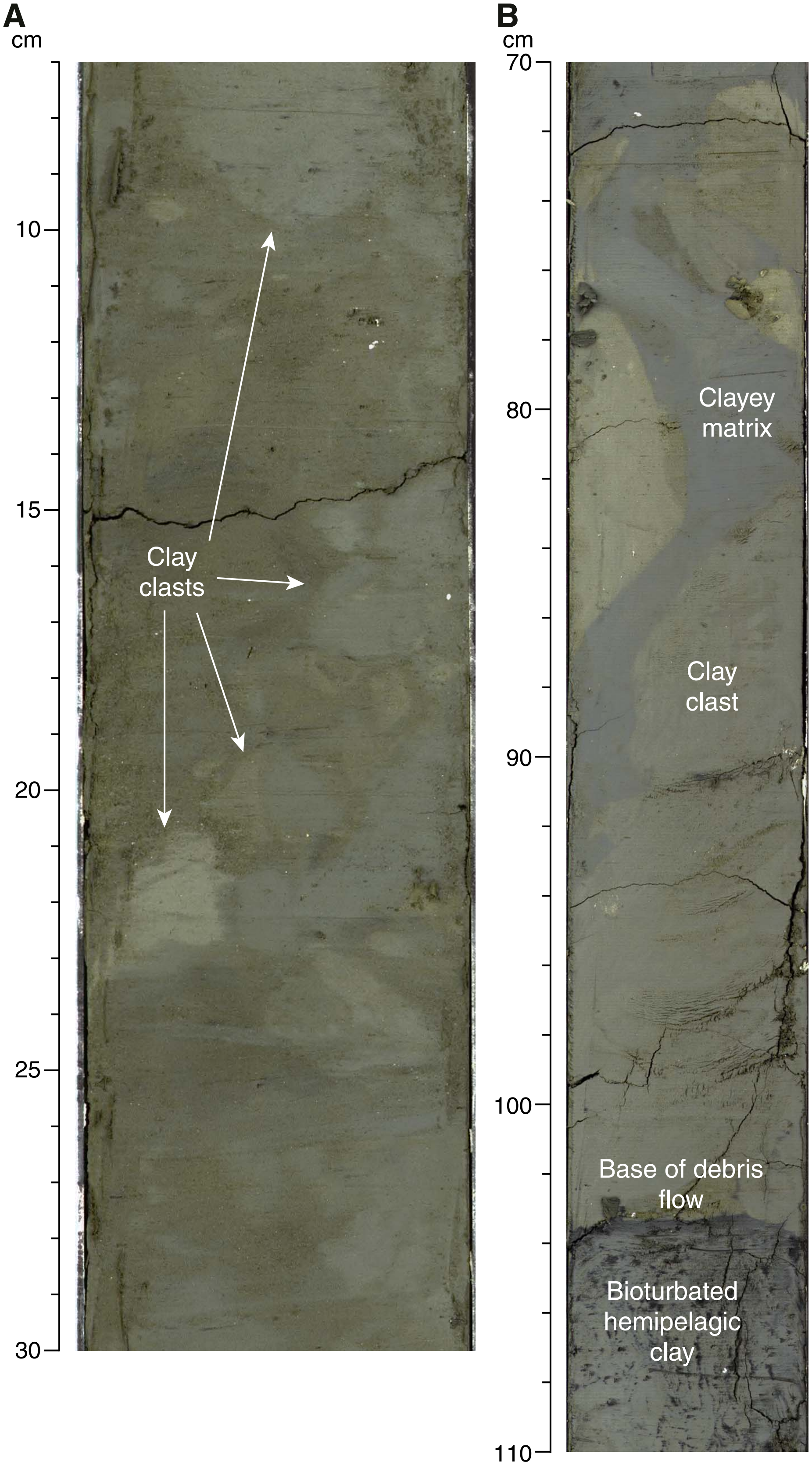

Figure F9. A. Close-up photograph of the volcanic glass–rich sand layers associated with Horizon A in lithostratigraphic Subunit IIIA (interval 204-1248C-14H-3, 112–118 cm). **B.** Photomicrograph of the volcanic ash layer (Sample **204-1248C-14H-3, 116 cm**).

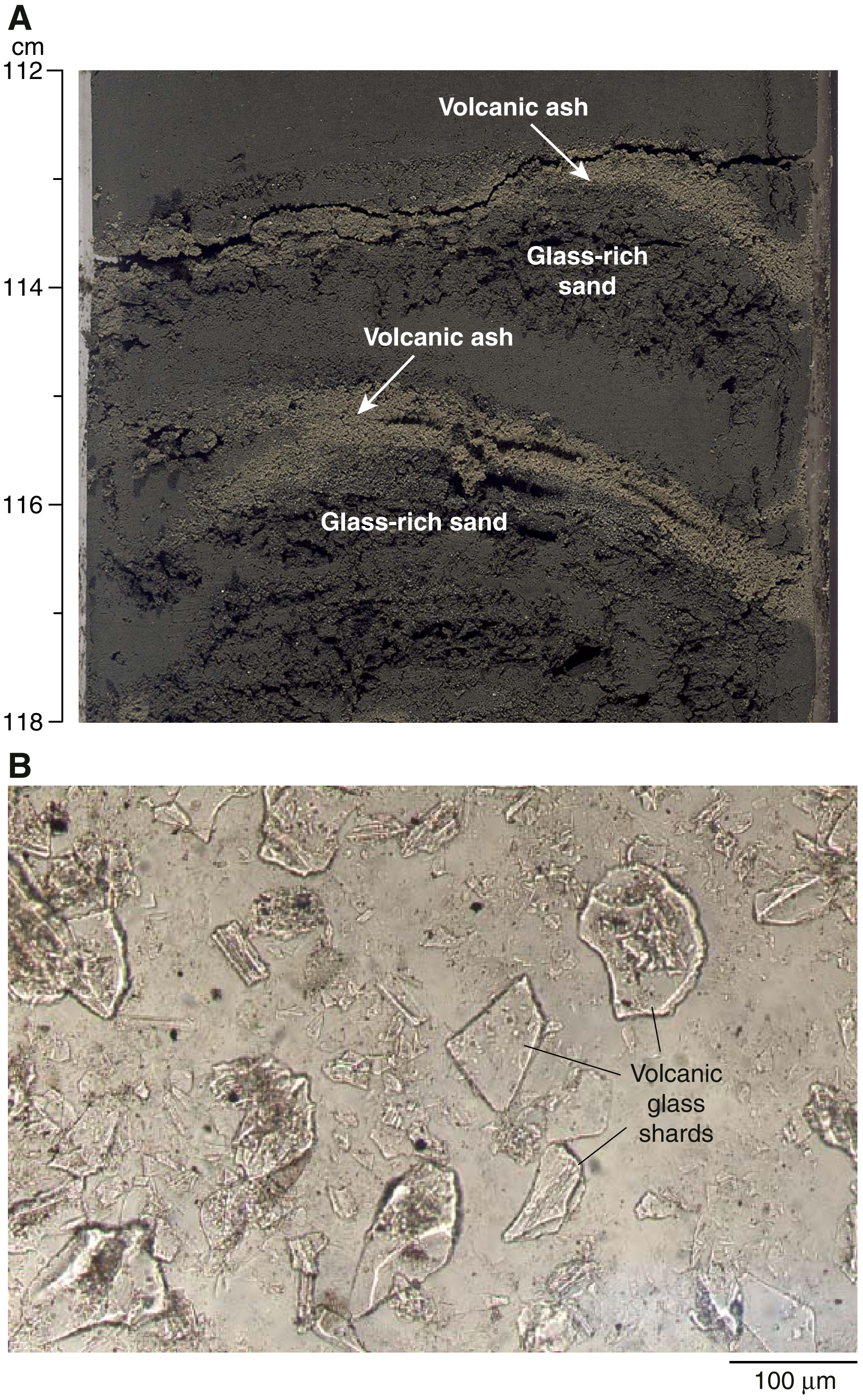

Figure F10. Chart of diatom and nannofossil event marker species in Hole 1248C.

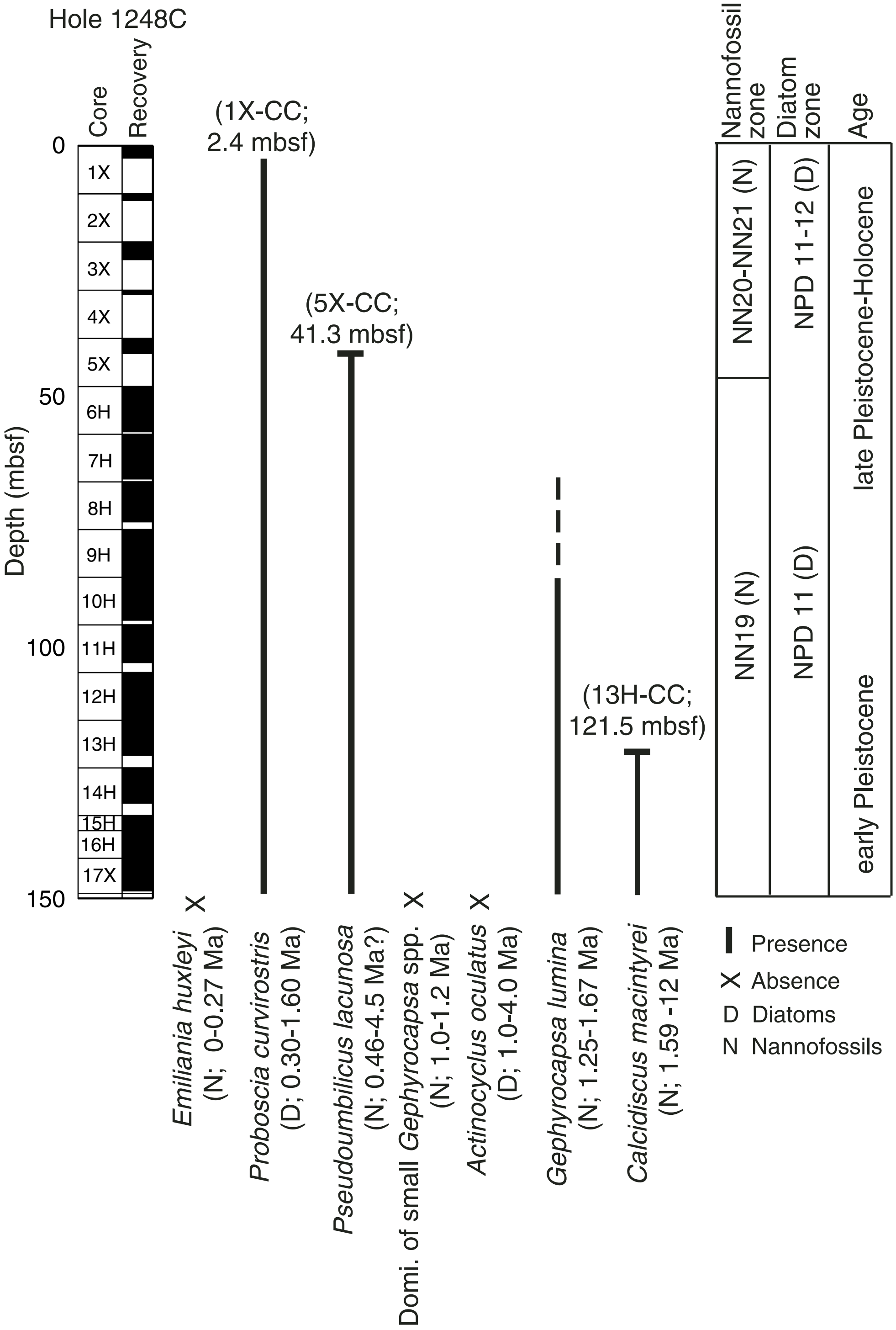

Figure F11. Age-depth plot based on diatom and calcareous nannofossil bioevents for Hole 1248C. The detailed age and depth of control points are shown in Table T3, p. 65. D = diatom event, N = nannofossil event.

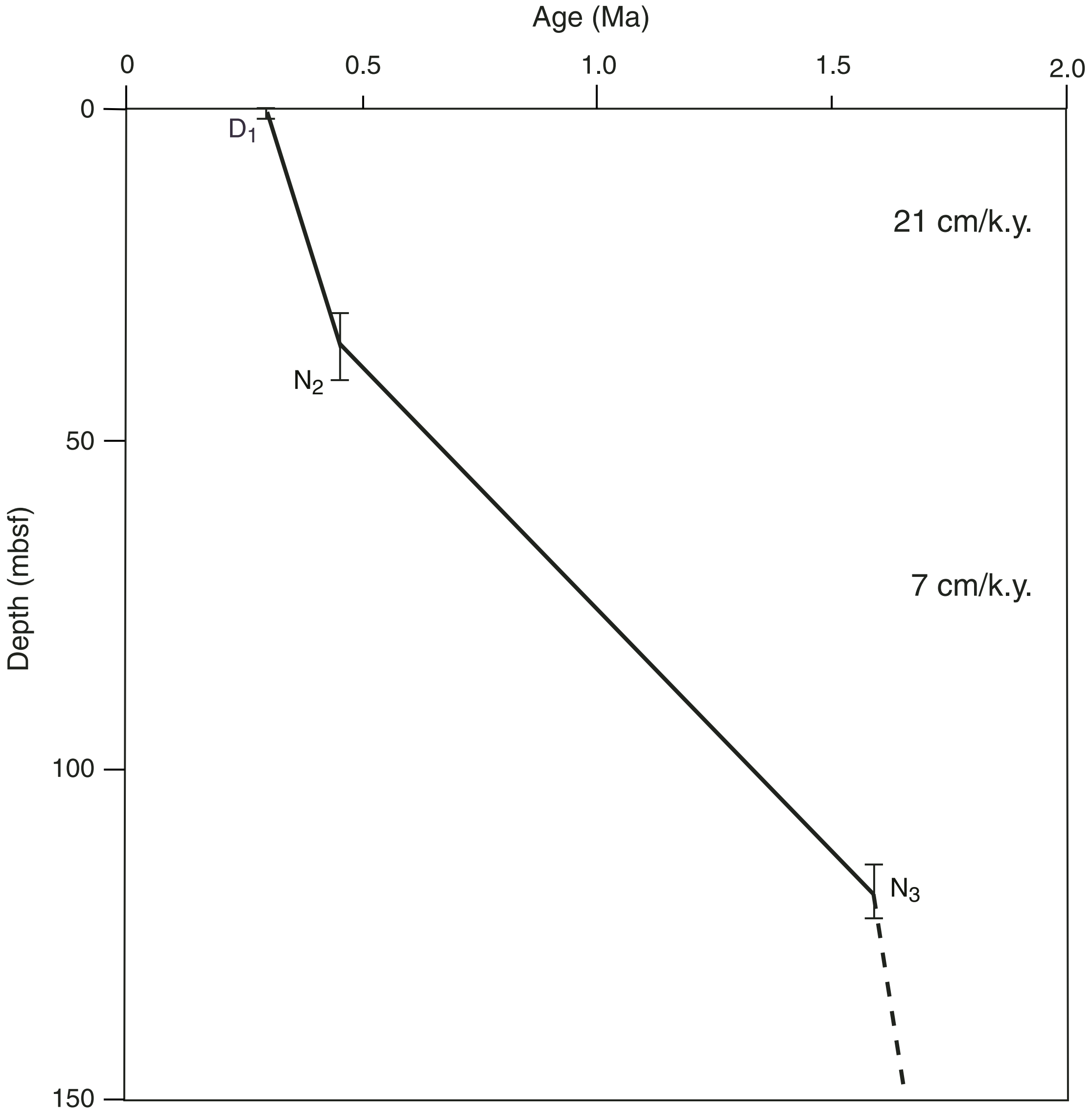

Figure F12. Concentration profiles of various dissolved species in pore waters from Holes 1248B (blue circles) and 1248C (red squares). DOC = dissolved organic carbon. (Continued on next page.)

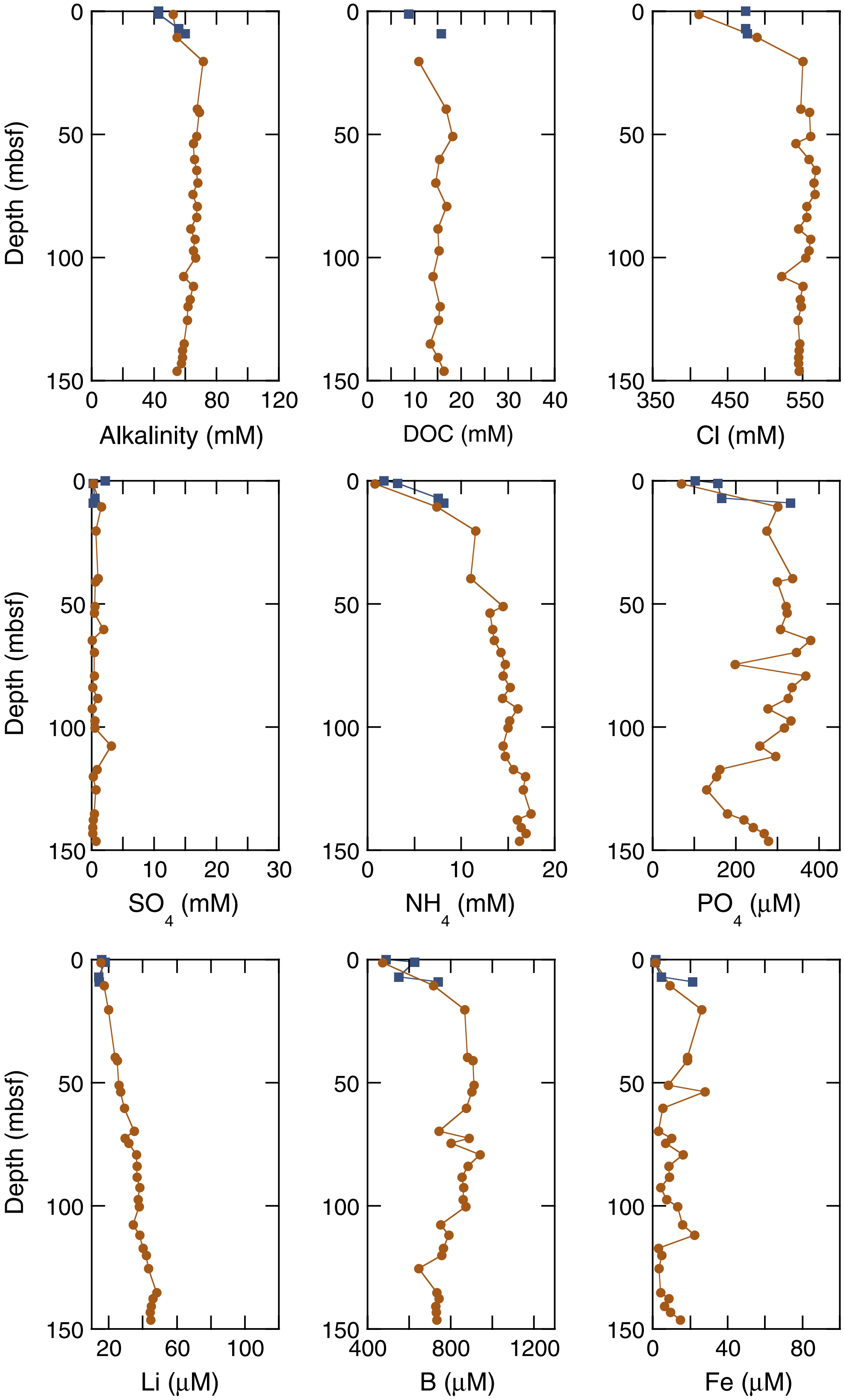

Figure F12 (continued).

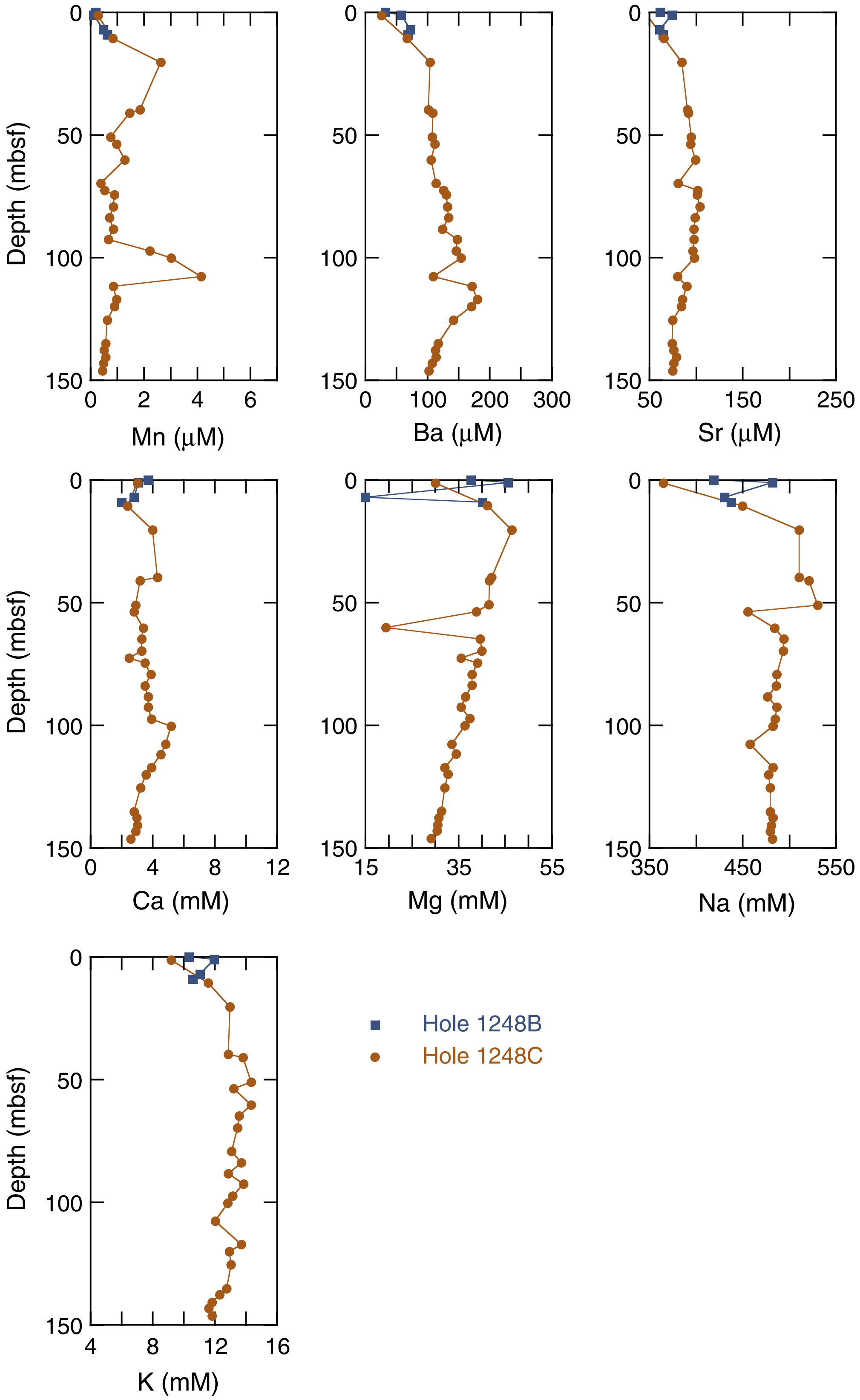

Figure F13. Chloride (Cl^-) concentration profile at Site 1248 showing its relationship to the position of the bottom-simulating reflector (BSR) at the base of the GHSZ. Data from Sites 1244 and 888 are shown for comparison. **A.** Chloride concentration data from Site 1248 show excursions to fresher values superimposed on a near-vertical baseline. The red shaded portion presumably reflects dissociation of gas hydrate, which is most prevalent in the sediments above 20 mbsf. Interstitial chloride data from Sites 1244 (blue circles) and 888 (black circles) are shown for comparison. **B.** Estimates of the fraction of pore space occupied by gas hydrate at Sites 1248 (red) and 1244 (blue). Note that based on the available IW data, as much as 25% of the pore space at Site 1248 is occupied by gas hydrate in the uppermost sediments. Deeper in the sediments, 0% to 5% of sediment pore space contains gas hydrate that is apparently localized in specific horizons. **C.** Interstitial sulfate data from Sites 1248 (red) and 1244 (blue). Sulfate is present in the uppermost sediments at Site 1244 so that methane and, thus, gas hydrate is absent from near-surface sediments. However, at Site 1248 sulfate is absent in the uppermost sediments and methane is present in sufficient concentration to form gas hydrate, possibly reflecting upward fluid advection at this site. BSR = bottom-simulating reflector.

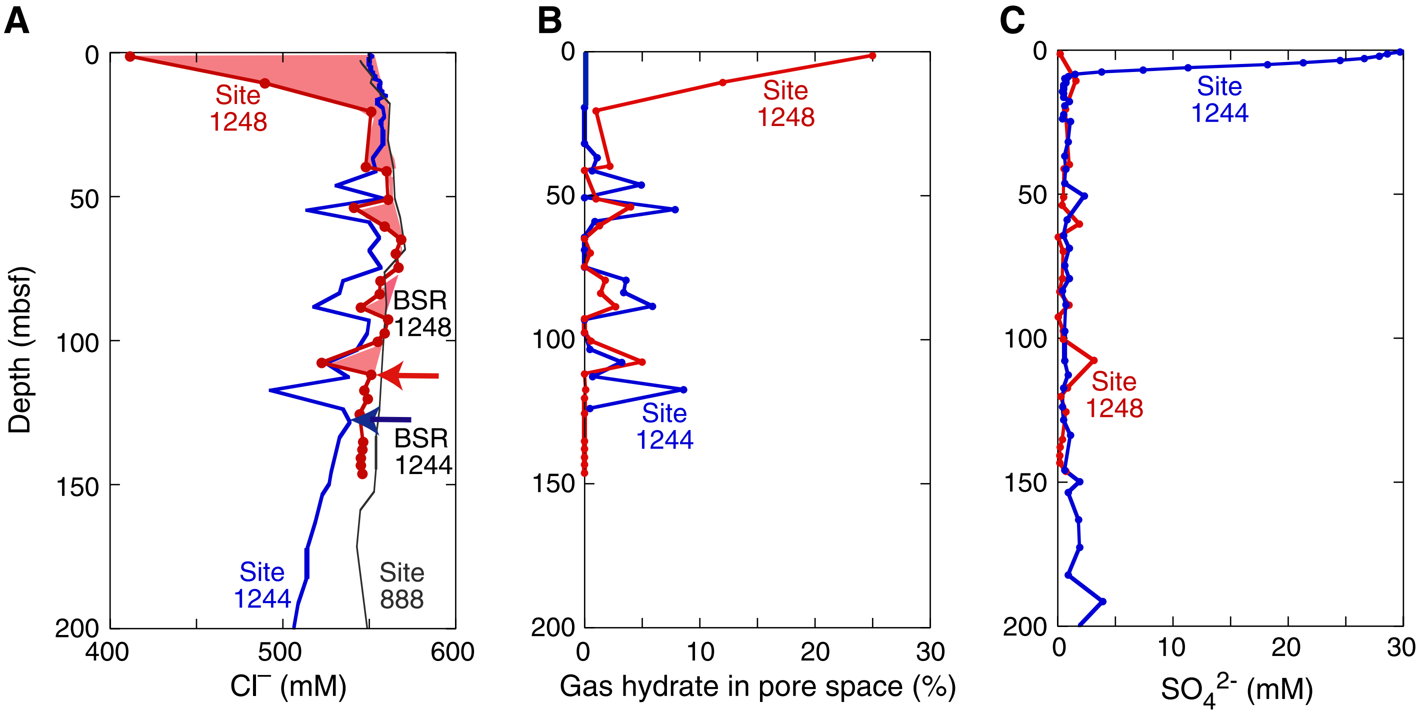

Figure F14. Profiles of dissolved interstitial sulfate (SO_4^{2-}) and barium (Ba^{2+}) at (**A**) Sites 1248 and (**B**) 1244, showing different processes at these sites. At Site 1244, sulfate is present in the upper sediments and dissolved barium concentrations are near zero because of presumed barite ($BaSO_4$) precipitation in this zone. At Site 1248, sulfate is absent in the upper sediments, so that dissolved barium may be released into the overlying water. The dashed line in A reflects higher barium concentration in situ, before freshwater is added to interstitial water by gas hydrate dissociation during sample recovery.

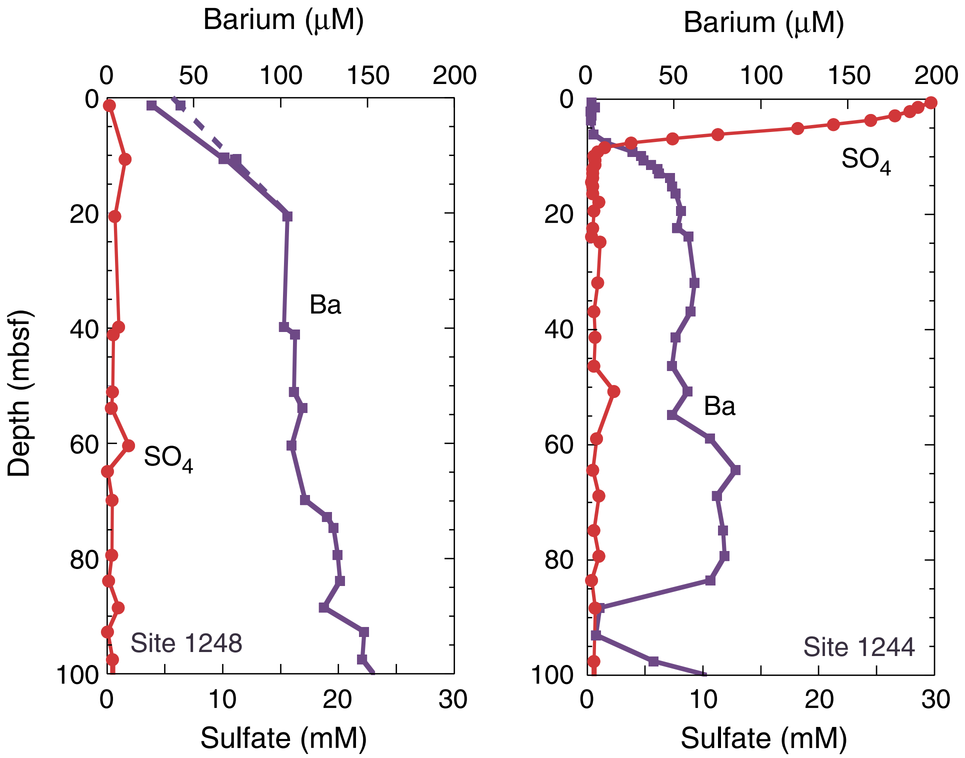

Figure F15. Interstitial dissolved boron (B) and strontium (Sr^{2+}) concentrations at Sites (**A**) 1248 and (**B**) 1244. At Site 1244, boron is enriched in the zone between 25 and 100 mbsf probably because of the release of boron from aragonite as it transforms to calcite during carbonate diagenesis. Note that strontium shows no increase in this zone. At Site 1248, both boron and strontium are enriched in the zone below 25 mbsf and show very similar profiles. BSR = bottom simulating reflector, Hor. A = Horizon A.

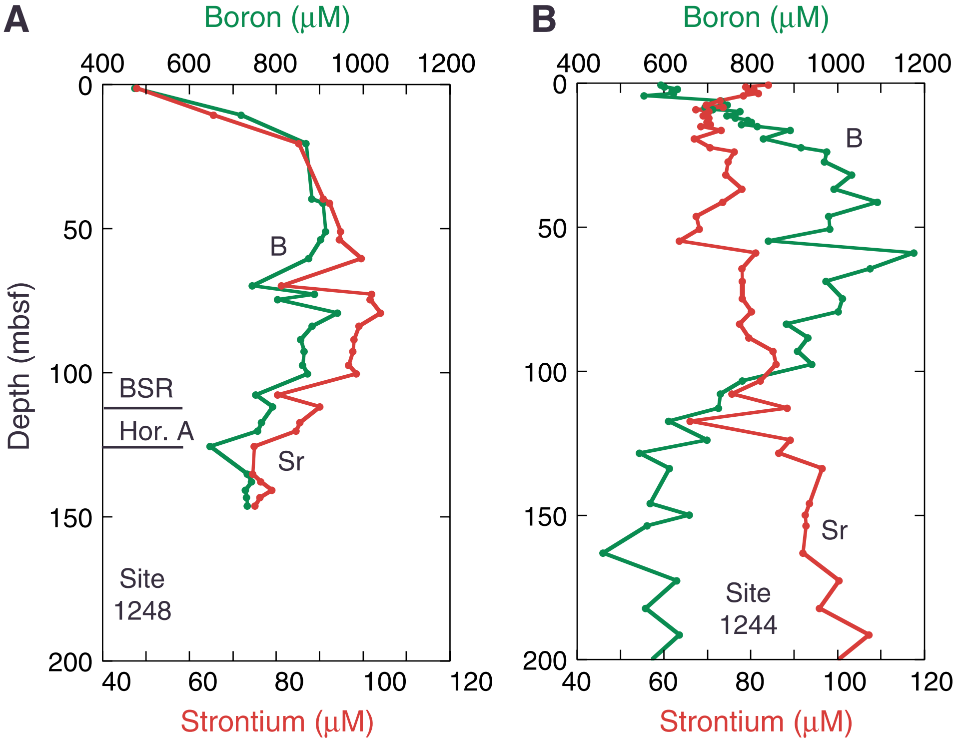

Figure F16. Concentrations of C_1, C_2, and C_3 from the headspace method vs. depth for Holes 1248B and 1248C.

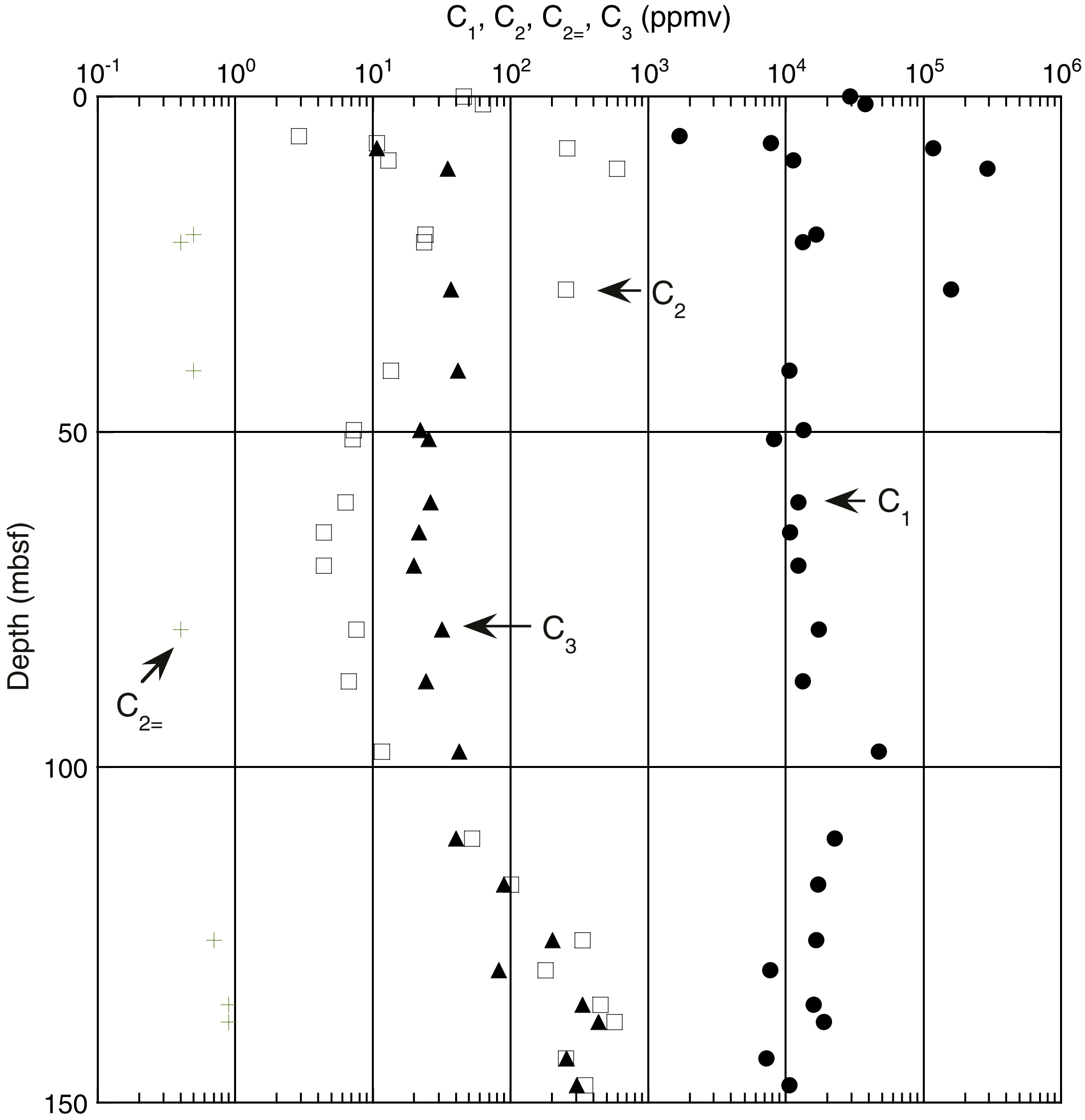

Figure F17. C_1, C_2, C_3, *i*-C_4, and *n*-C_4 from void gas vs. depth for Holes 1248B and 1248C.

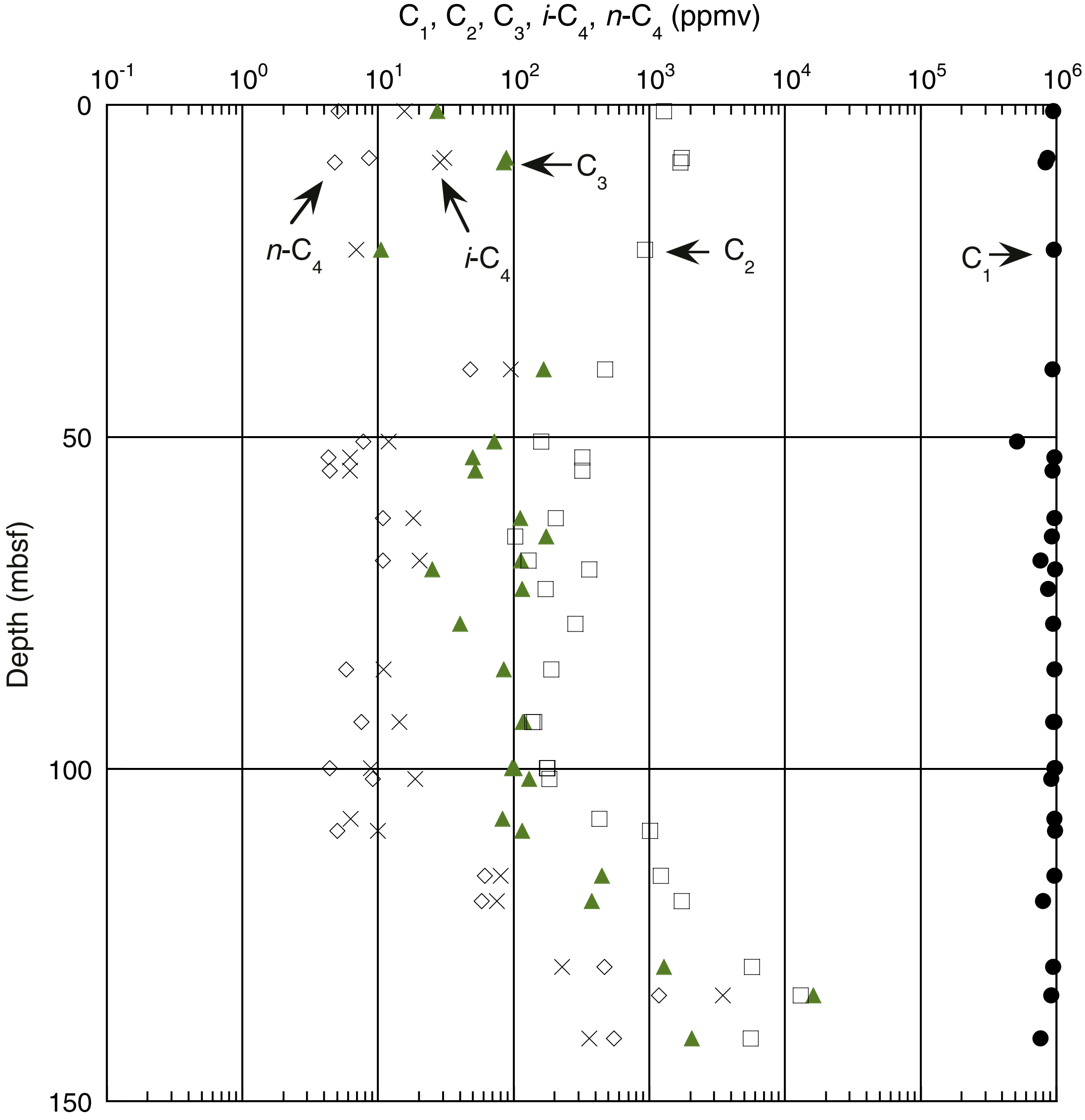

Figure F18. C_1, C_2, C_3, *i*-C_4, and *n*-C_4 from decomposed gas hydrates vs. depth for Holes 1248B and 1248C.

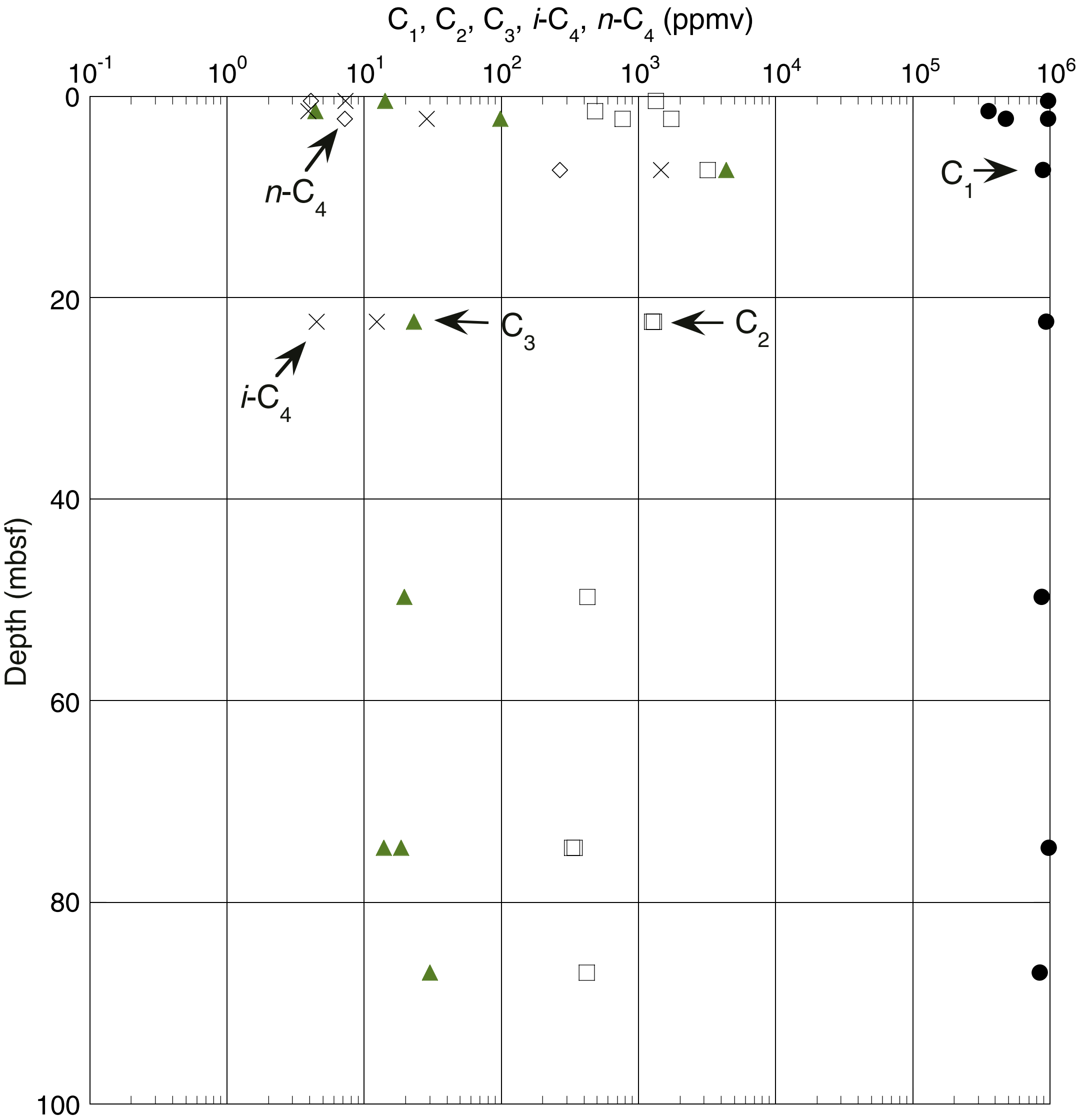

Figure F19. C_1/C_2 ratio vs. depth for Holes 1248B and 1248C. GH = gas hydrate, HS = headspace, VAC = vacutainer.

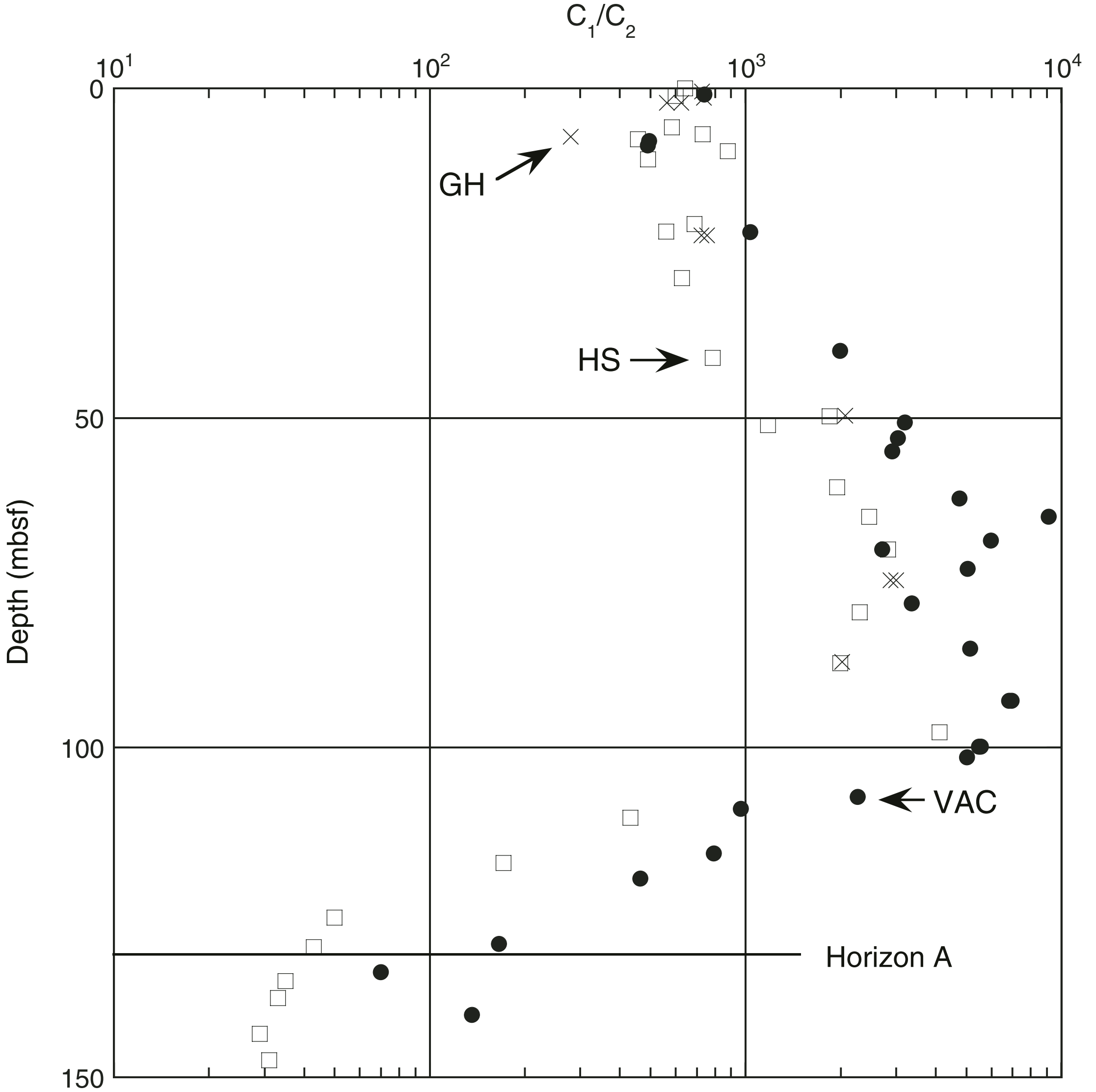

Figure F20. C_1/C_2 ratio vs. temperature for Holes 1248B and 1248C. GH = gas hydrate, HS = headspace, VAC = vacutainer.

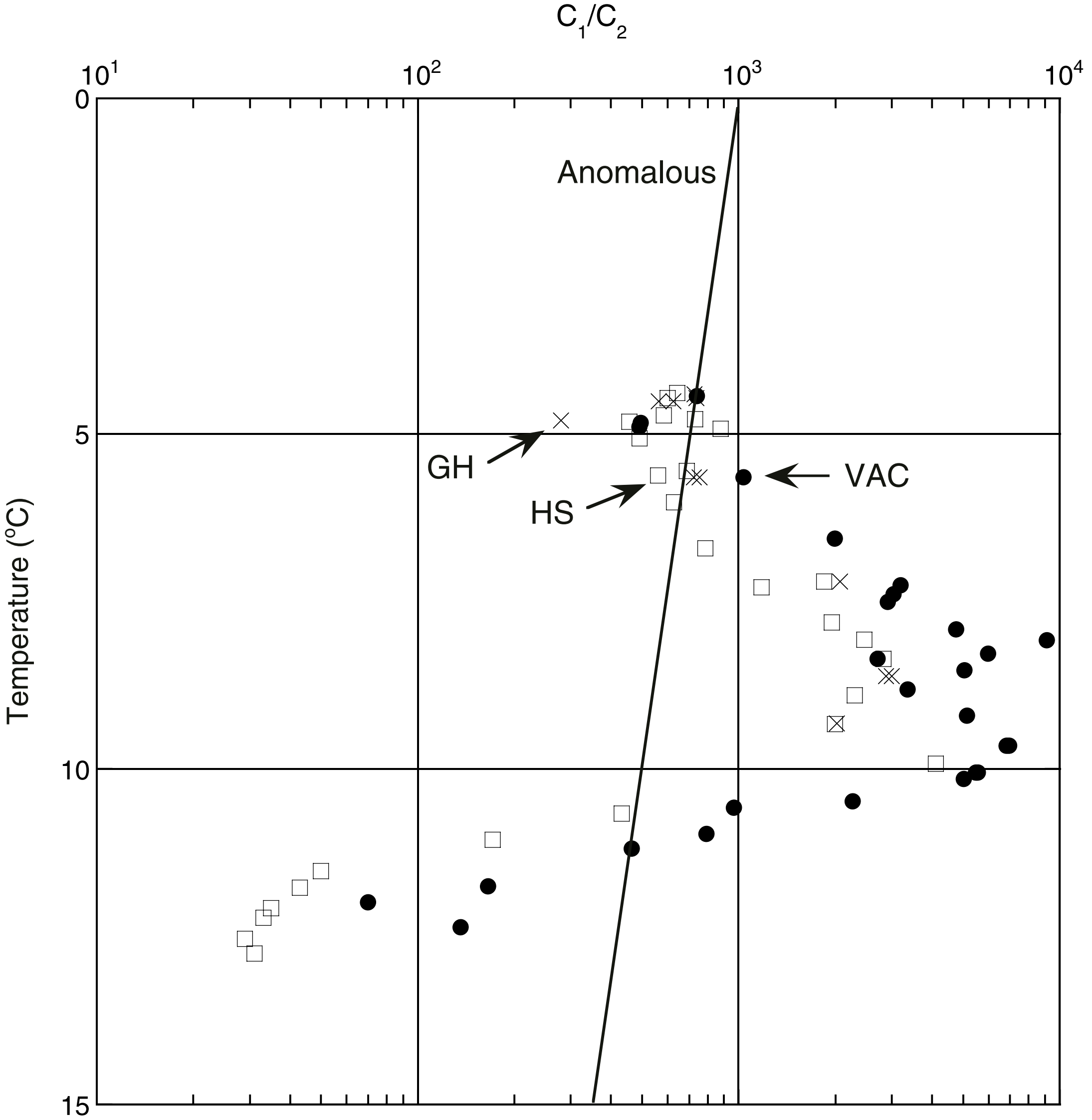

Figure F21. Contents of IC, OC, TN, and TS in sediment from Site 1248.

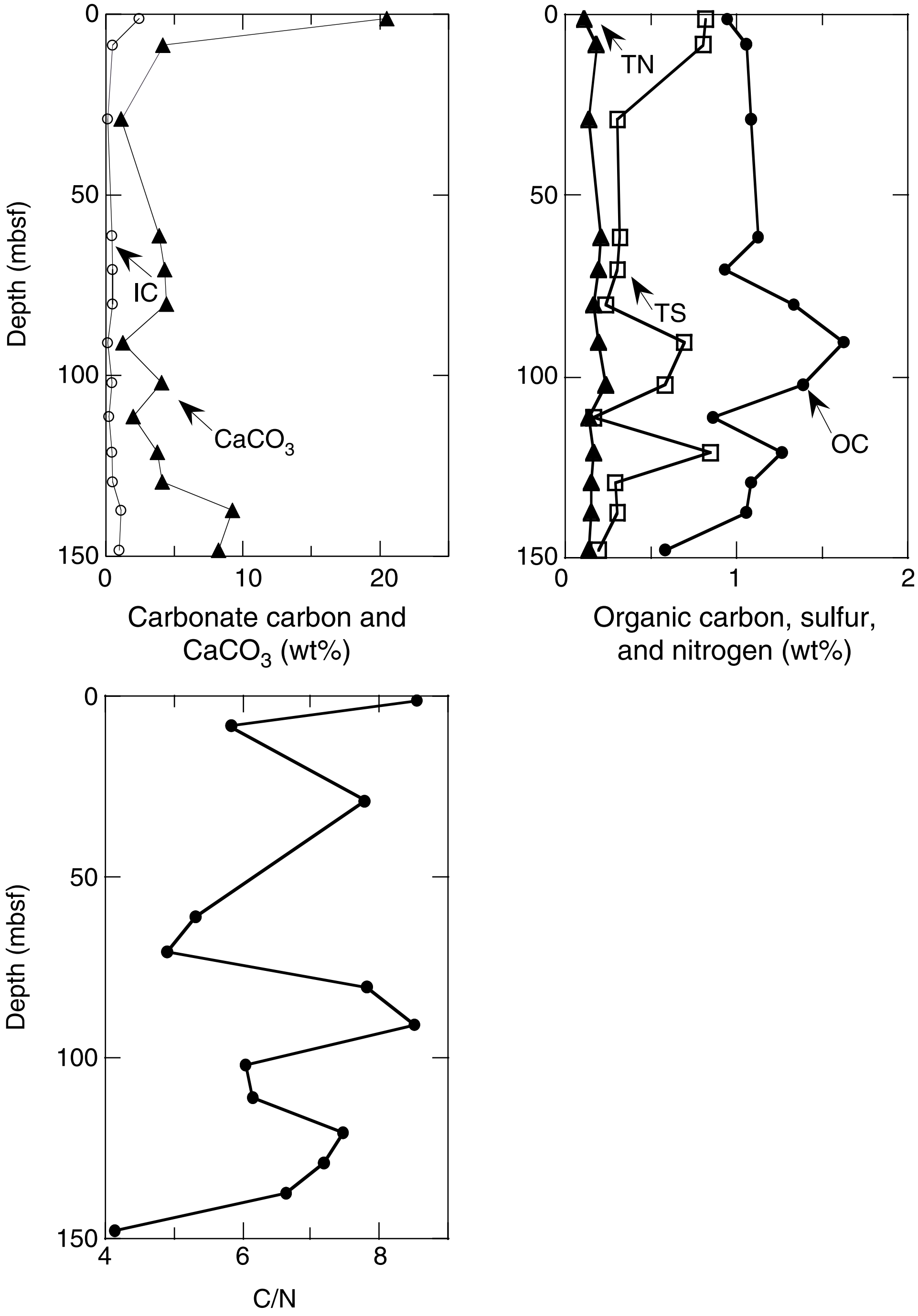

Figure F22. Examples of the different character of hydrate IR thermal anomalies. **A.** Vein at a shallow dip (Section 204-1248C-7H-1). **B.** Nodular (Section 204-1248C-10H-5). **C.** Disseminated (Section 204-1248C-11H-2). **D.** Nodular or blade shaped (Section 204-1248C-11H-6).

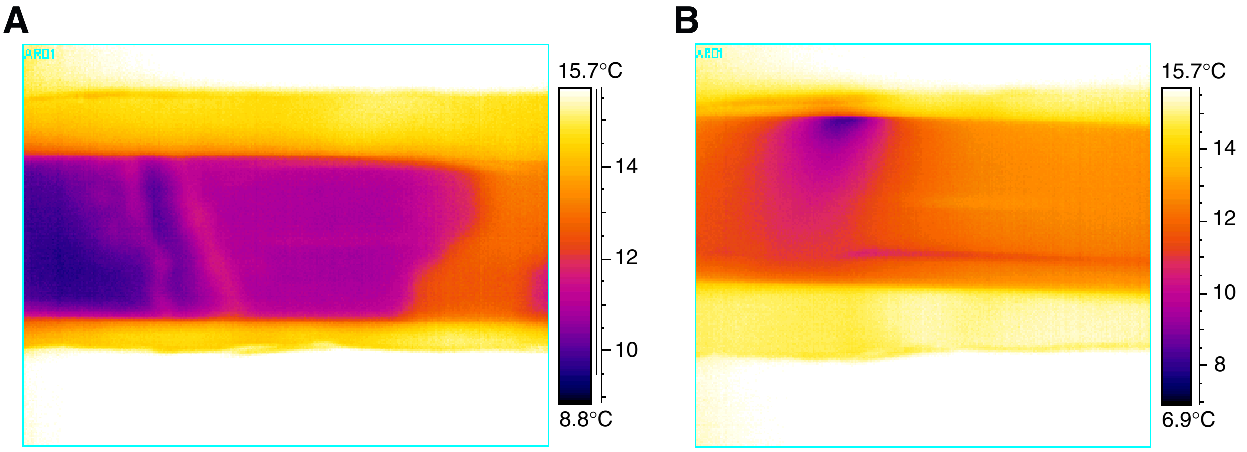

Vein, shallow dip (Section 204-1248C-7H-1; IR128)

Nodular (Section 204-1248C-10H-5; IR152)

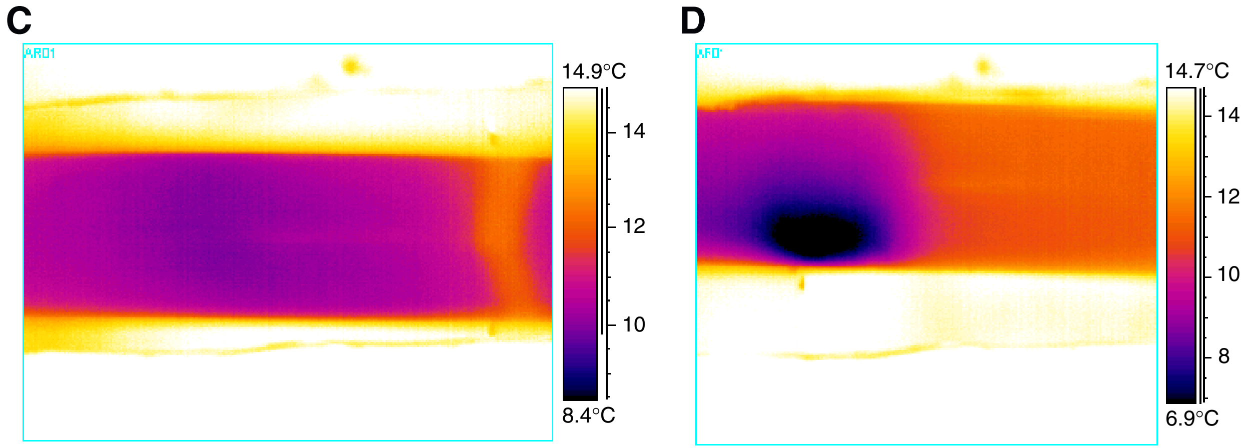

Disseminated (Section 204-1248C-11H-2; IR155)

Nodular or blade-shaped (Section 204-1248-11H-6; IR157)

Figure F23. Relationship between IR images and development of minor mousselike texture and voids in split cores after temperature equilibration (interval 204-1248C-6H-1, 111–116 cm).

IR 117 Sample 204-1248C-6H-1, 111-116 cm

First IR image (9:53:06)

Second IR image (10:11:04)

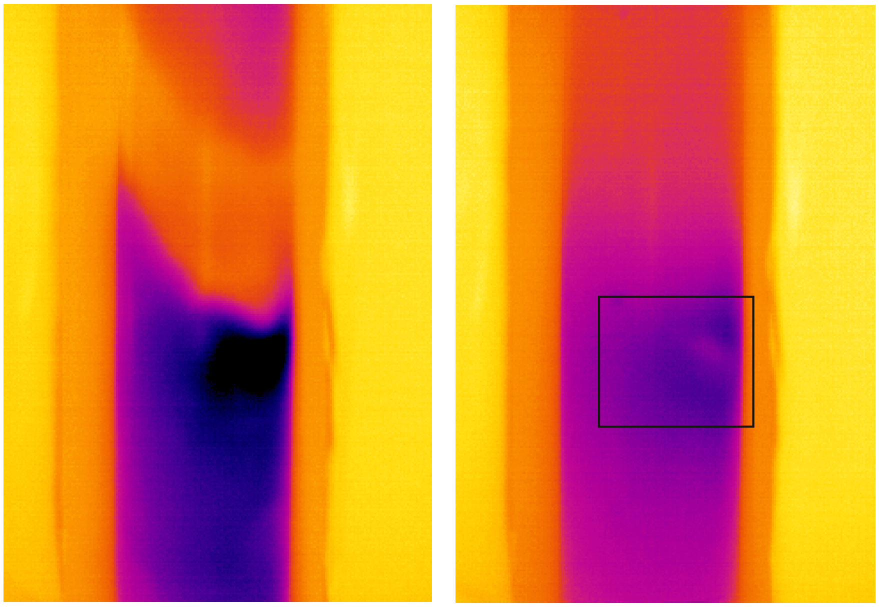

Time difference: 18:56 min

Digital image of archive half

Figure F24. Downhole temperature derived from IR thermal images for Holes 1248B and 1248C. APC = advanced piston corer, XCB = extended core barrel, BSR = bottom-simulating reflector.

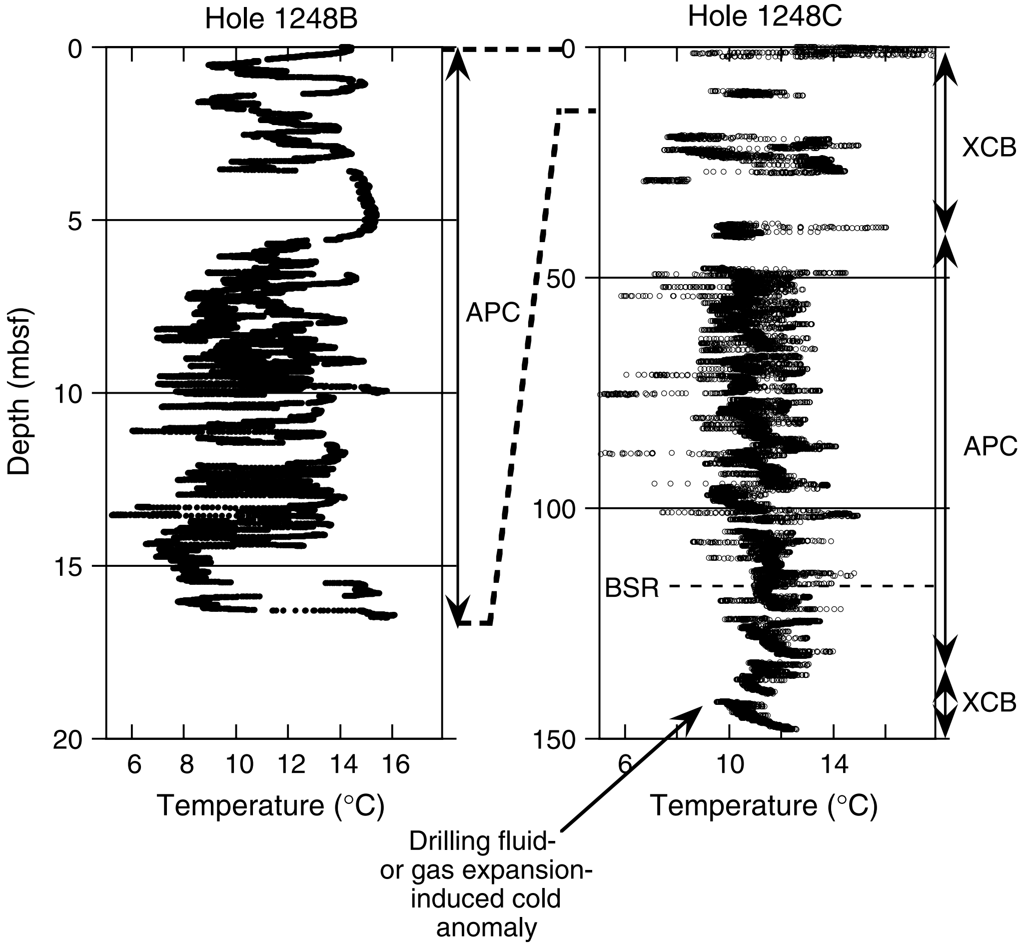

Figure F25. Comparison of IR thermal anomalies with S_w from LWD resistivity and core recovery at Site 1248. BSR = bottom-simulating reflector.

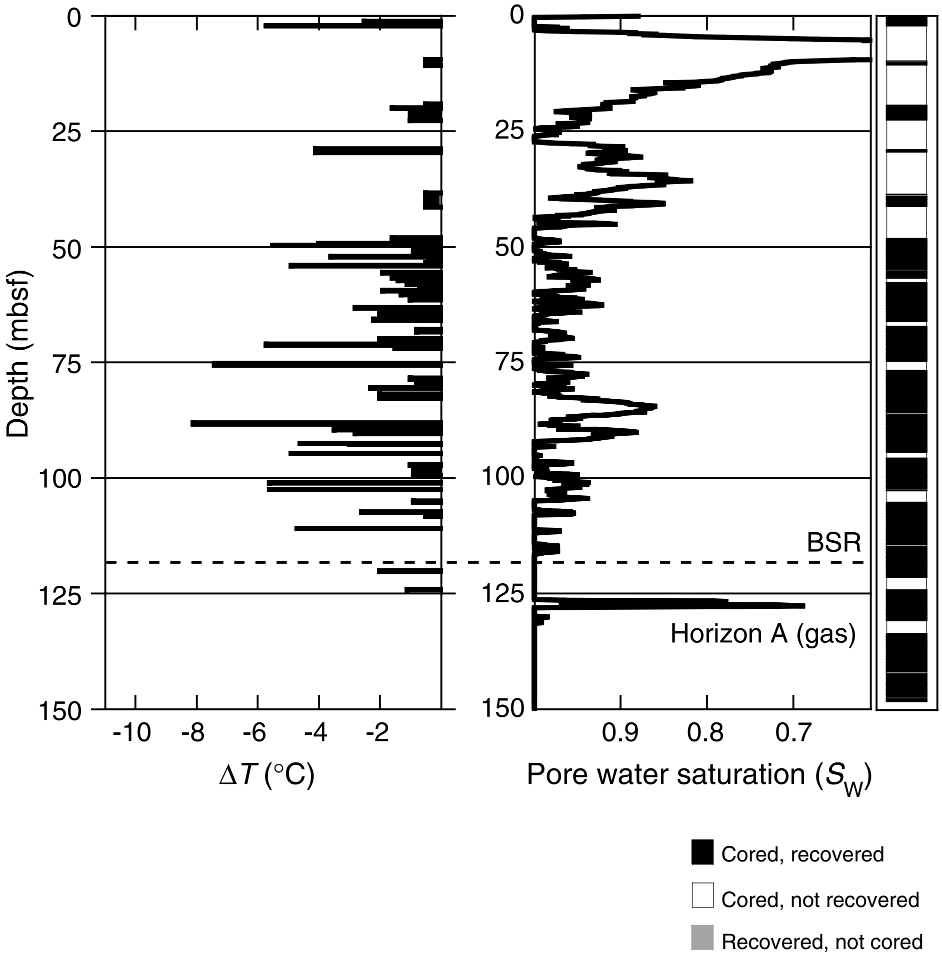

Figure F26. Physical properties across Horizon A at Site 1248. LWD = logging-while-drilling, GRA = Gamma ray attenuation, MAD = moisture and density.

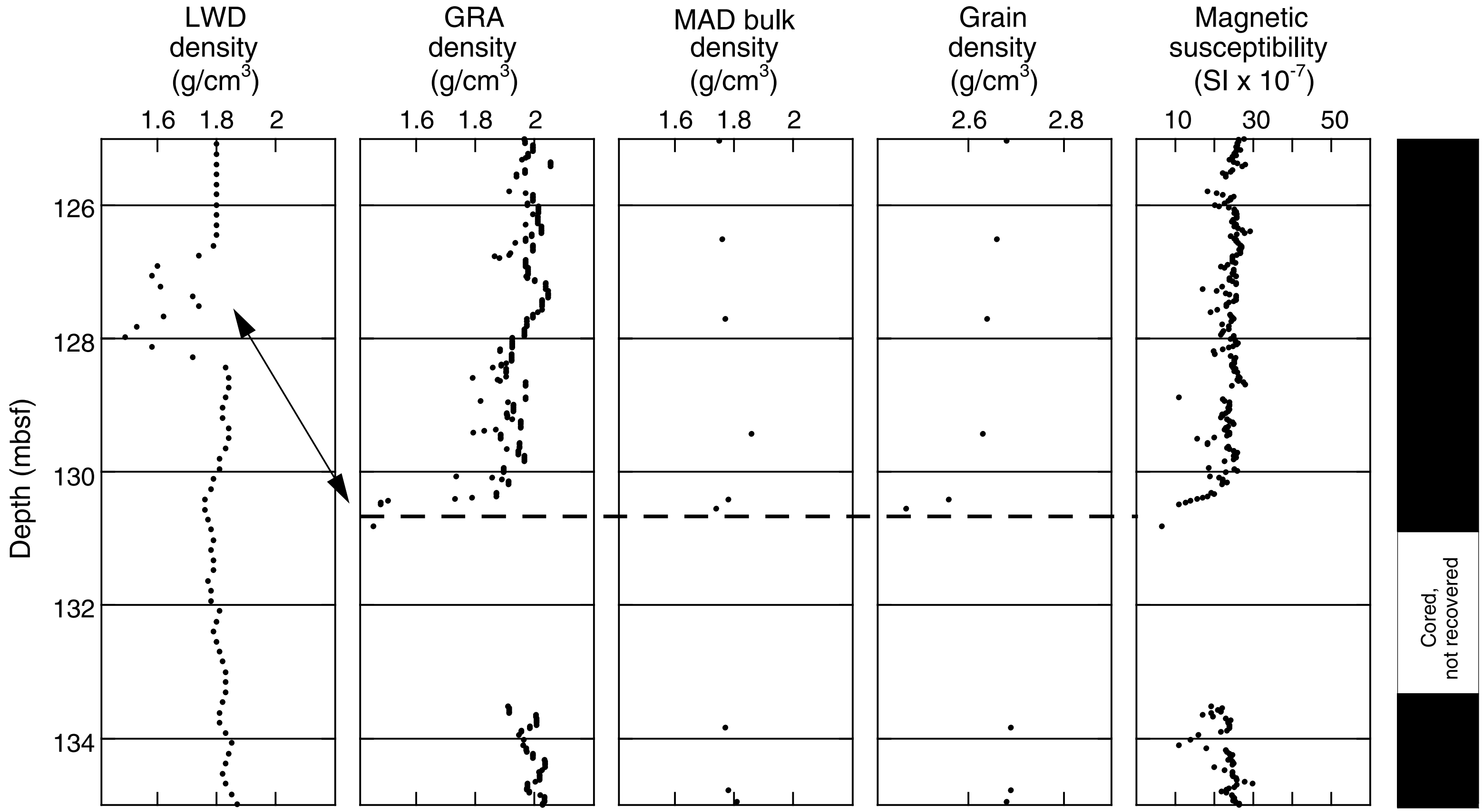

Figure F27. Overview of physical properties measured at Site 1248. LWD = logging-while-drilling, GRA = Gamma ray attenuation, MAD = moisture and density.

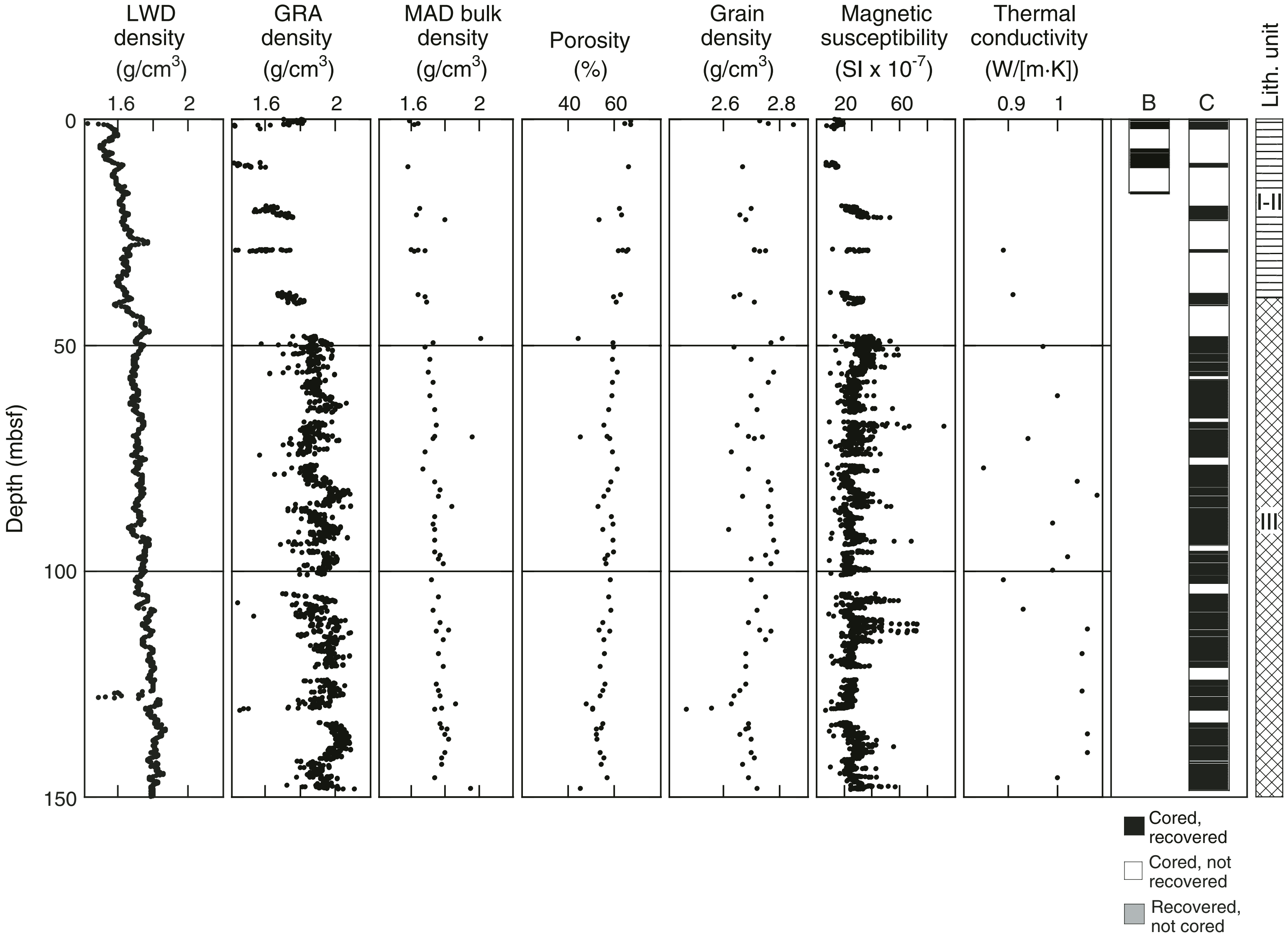

Figure F28. Noncontact resistivity (NCR) profiles illustrating the effects of extensive gas cracking below the first few meters from Holes 1248B and 1248C.

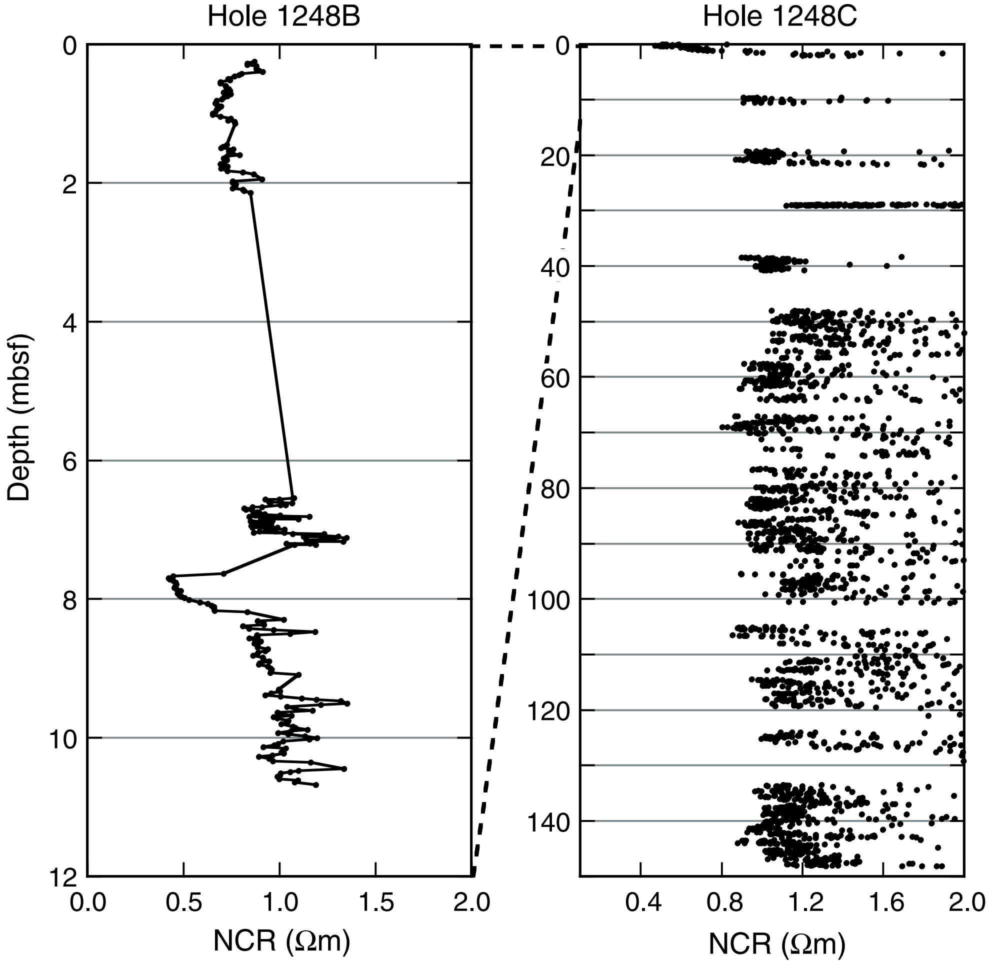

Figure F29. Change in resistivity between start and end of a gas hydrate dissociation experiment indicating a measurable effect from hydrate during dissociation.

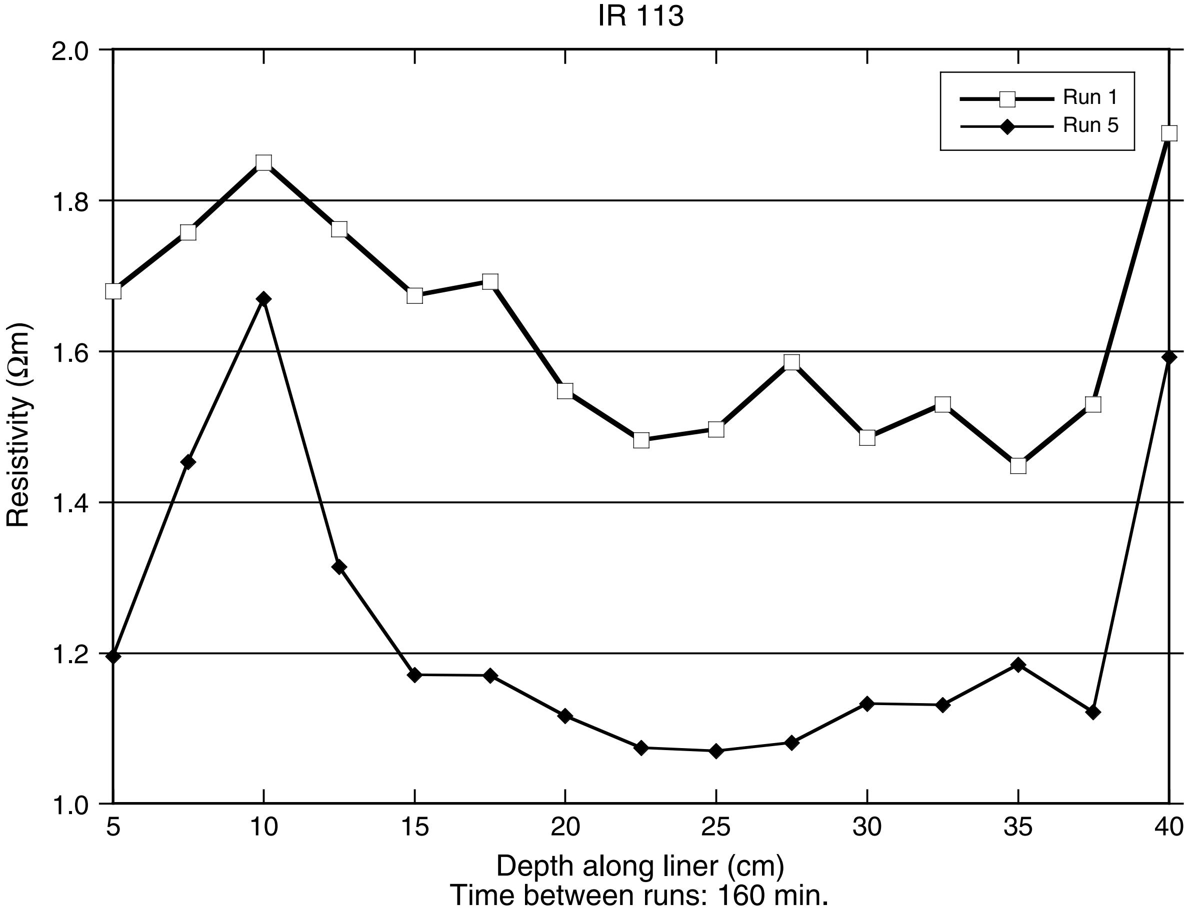

Figure F30. Temperature time series recorded at Site 1248. **A.** APCT tool data. **B.** DVTP data. **C.** DVTPP data.

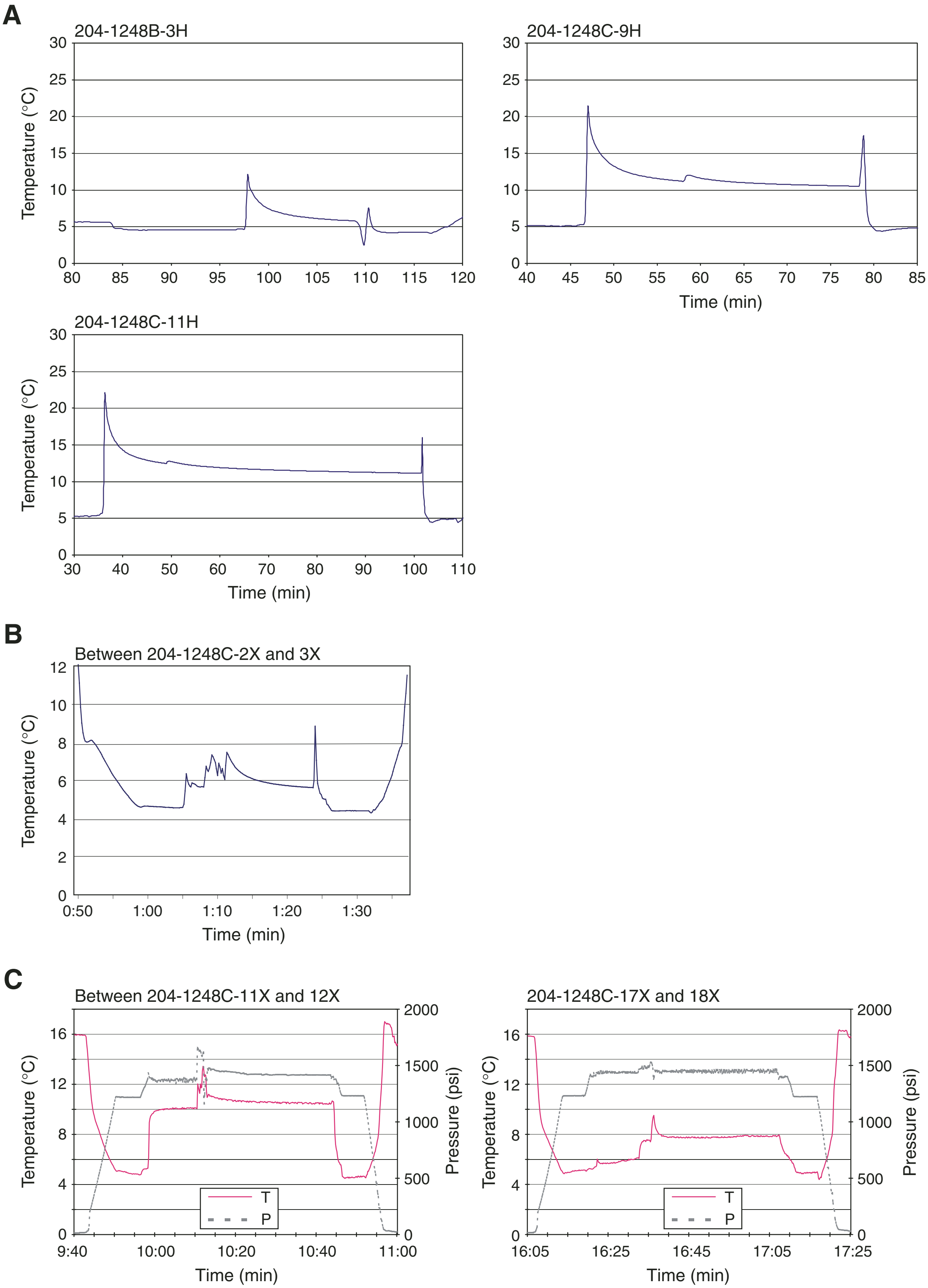

Figure F31. Estimated temperature as a function of depth at Site 1248. Open symbols = not used for calculation of temperature gradient. APCT = advanced piston corer temperature tool, DVTP = Davis-Villinger Temperature Probe.

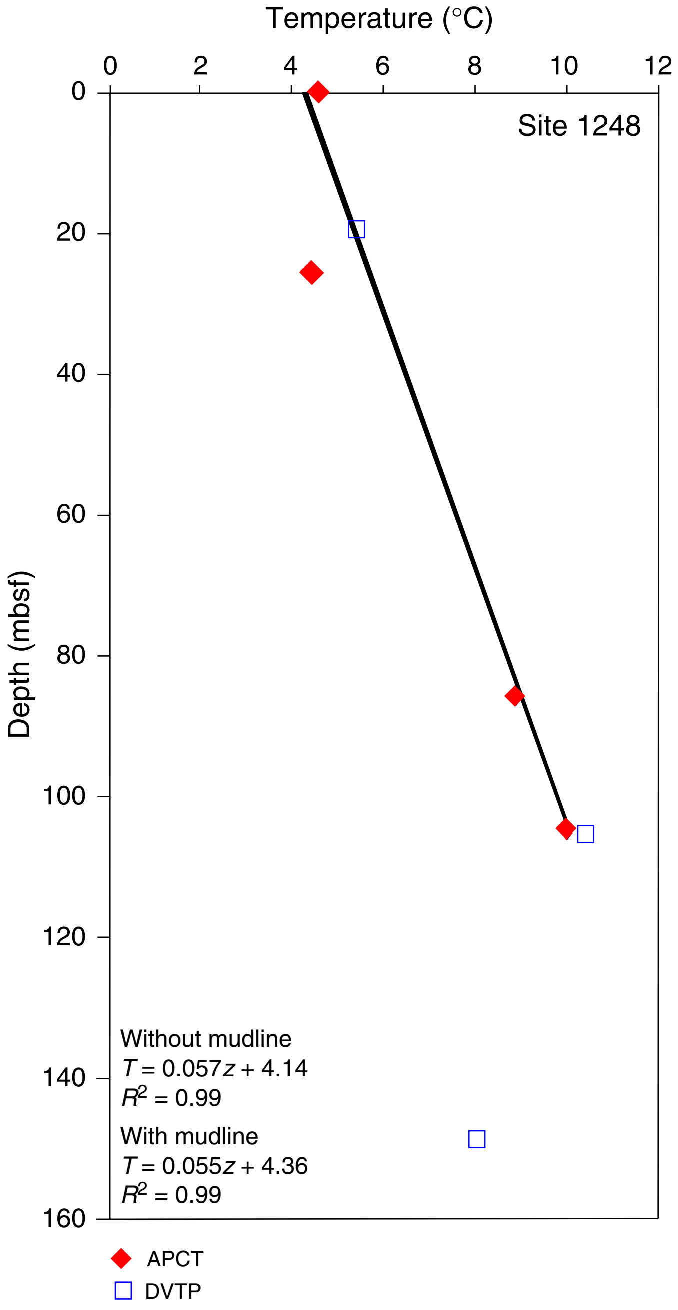

Figure F32. Quality control LWD logs for Hole 1248A. TAB = time after bit.

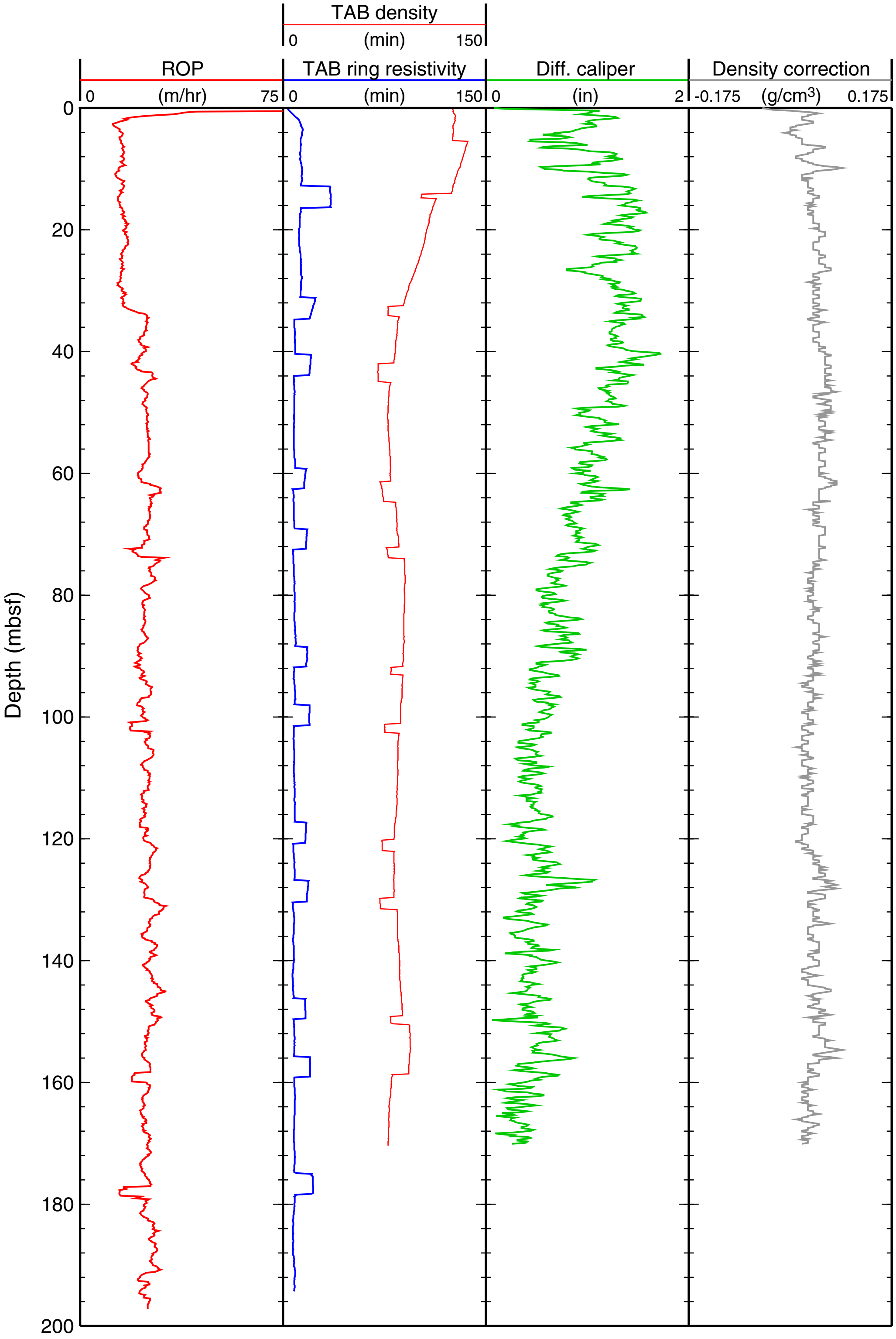

Figure F33. Summary of LWD log data from Hole 1248A. TAB = time after bit, RAB = resistivity-at-the-bit.

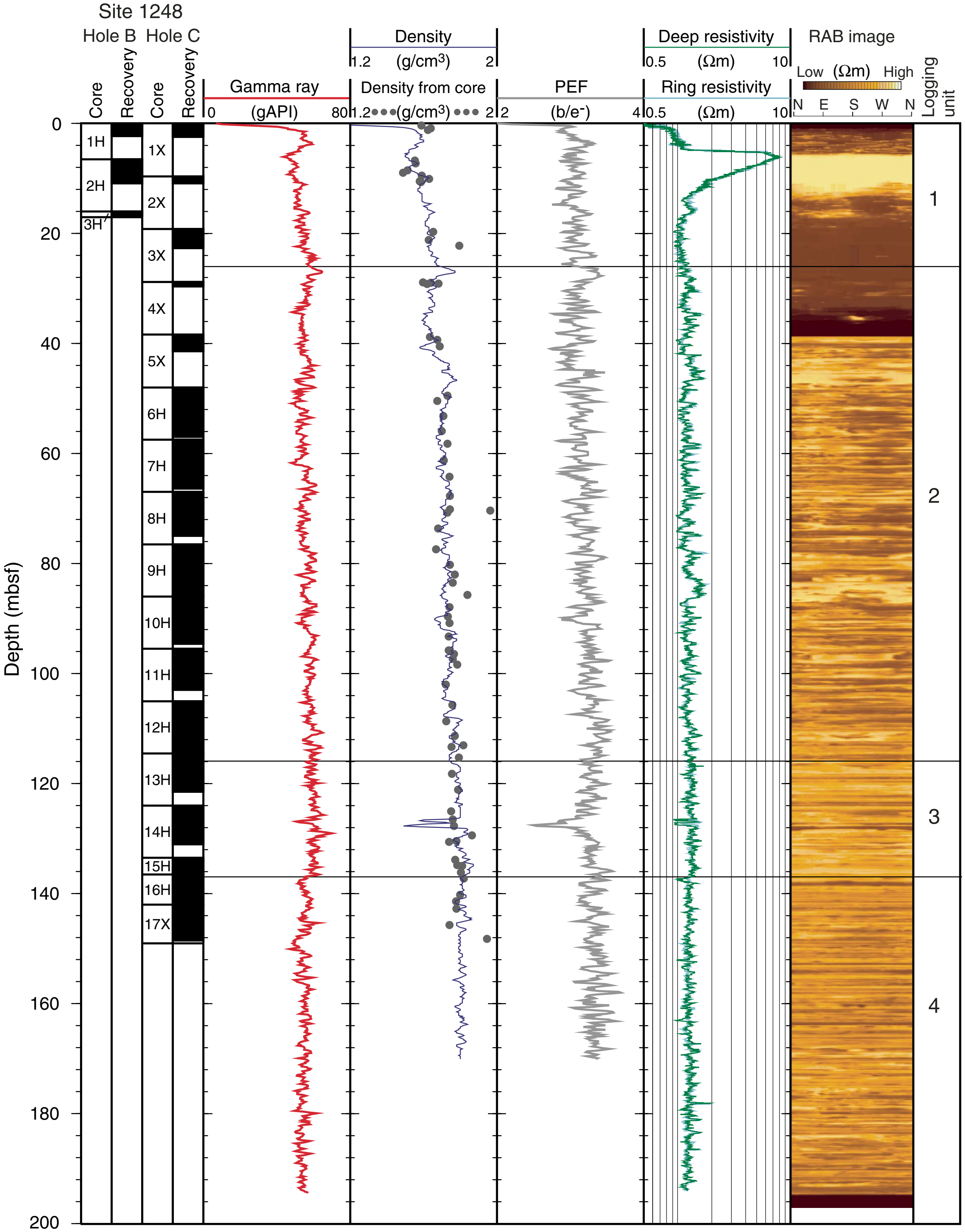

Figure F34. LWD- and core-derived porosities for Hole 1248A. NMR-MRP = Nuclear Magnetic Resonance tool, RAB = resistivity-at-the-bit.

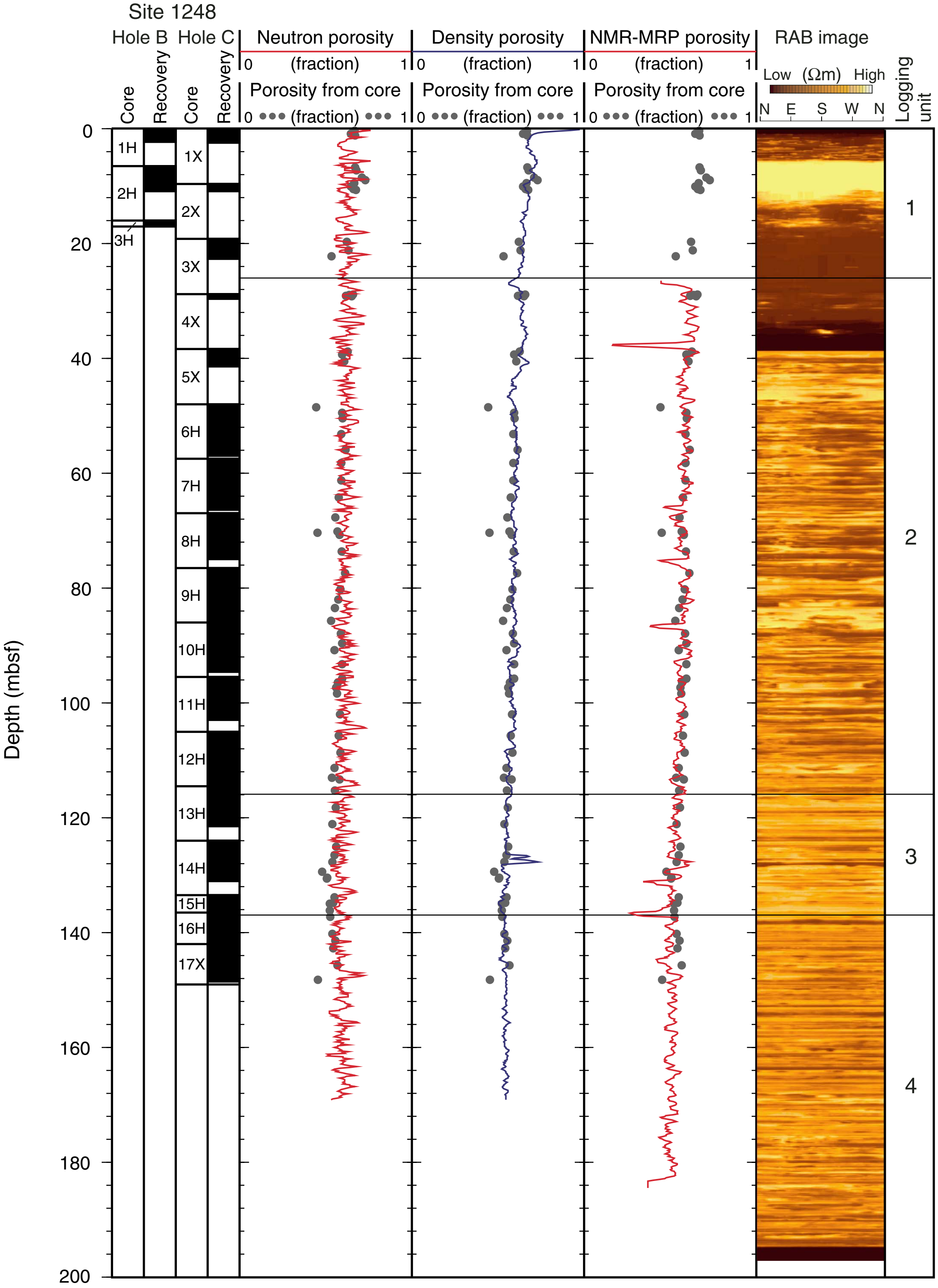

Figure F35. Logging-derived gas hydrate saturations for Hole 1248A. gAPI = American Petroleum Institute gamma ray units, RAB = resitivity-at-the-bit.

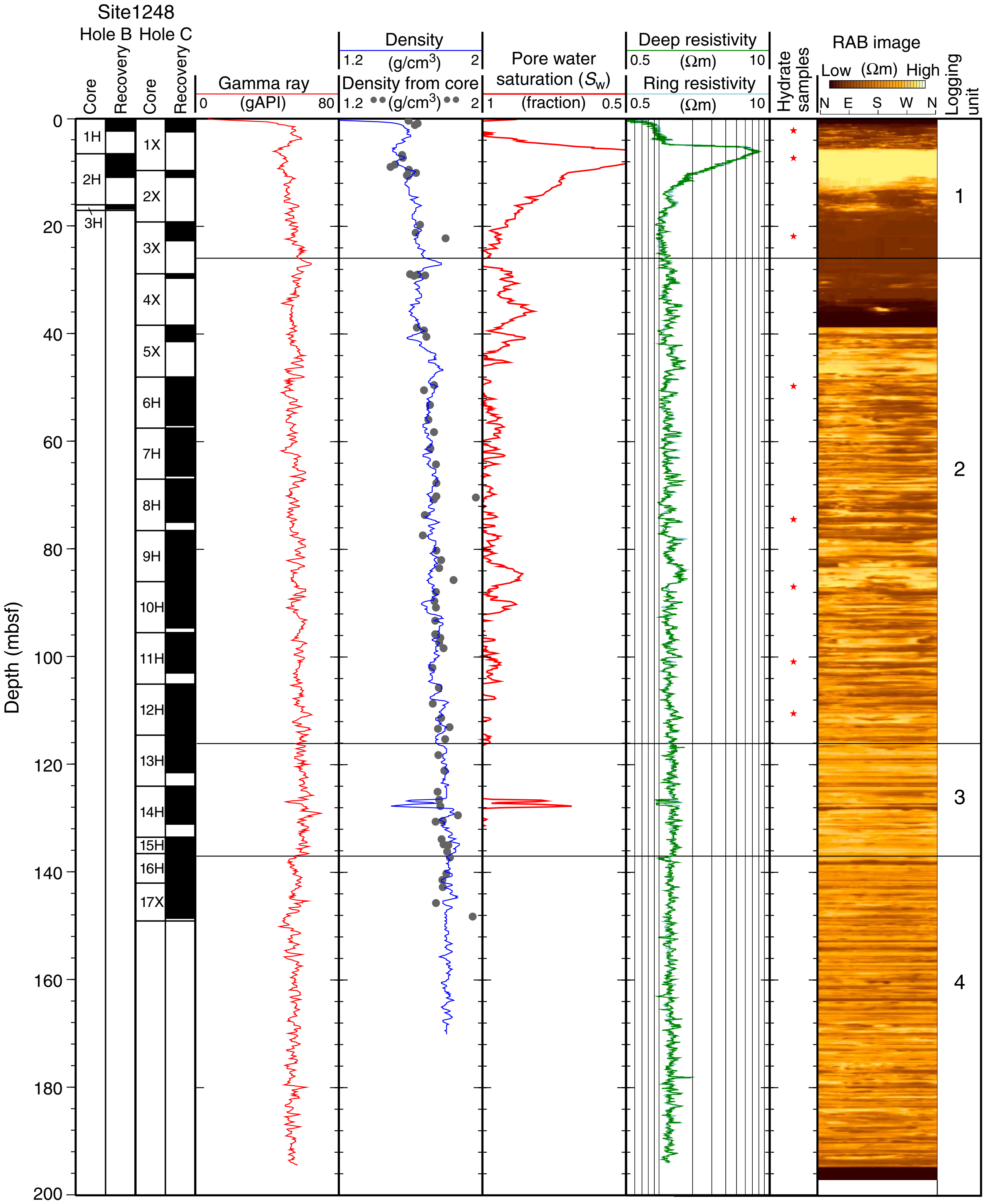

Figure F36. Resistivity-at-the-bit (RAB) image showing the possible presence of gas hydrate as bright resistive material occupying low-angle fractures and nearly flatlying stratigraphic horizons in Hole 1248A. 3-D = three-dimensional.

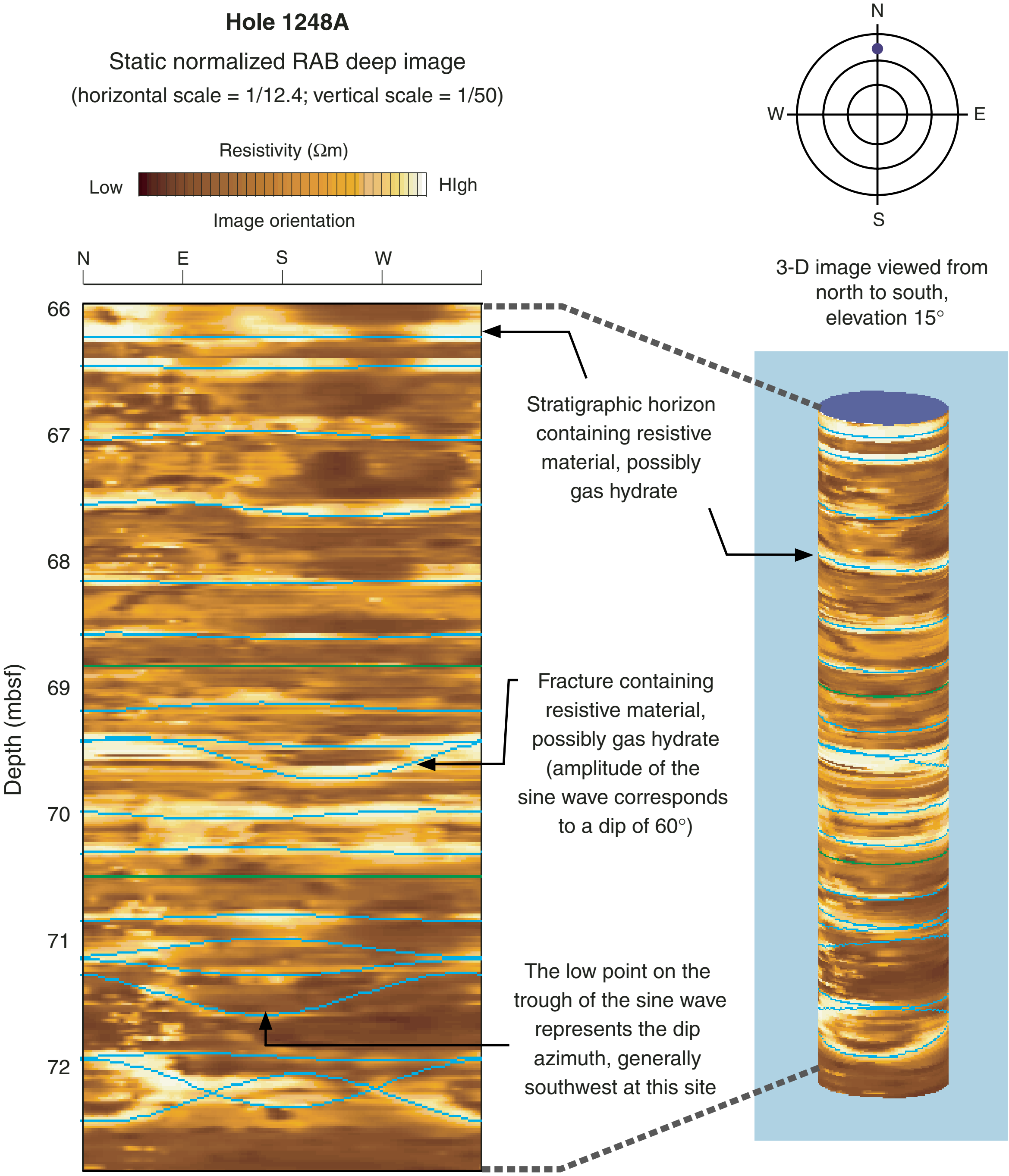

Table T1. Coring summary, Site 1248. (Continued on next page.)

Hole 1248A

Latitude: 44°34.4515′N
Longitude: 125°9.1548′W
Time on site (hr): 49 (1515 hr, 20 Jul–0645 hr, 21 Jul 2002)
Time on hole (hr): 15.5 (1515 hr, 20 Jul–0645 hr, 21 Jul 2002)
Seafloor (drill pipe measurement from rig floor, mbrf): 843
Distance between rig floor and sea level (m): 11
Water depth (drill pipe measurement from sea level, m): 832
Total depth (drill pipe measurement from rig floor, mbrf): 1037
Total penetration (meters below seafloor, mbsf): 194
Total number of cores: 0
Total number of drilled intervals: 1
Total length of cored section (m): 0
Total core recovered (m): 0
Core recovery (%): 0

Hole 1248B

Latitude: 44°34.4568′N
Longitude: 125°9.1482′W
Time on hole (hr): 10.75 (0300 hr, 1 Aug–1345 hr, 1 Aug 2002)
Seafloor (drill pipe measurement from rig floor, mbrf): 841
Distance between rig floor and sea level (m): 11.4
Water depth (drill pipe measurement from sea level, m): 829.6
Total depth (drill pipe measurement from rig floor, mbrf): 858
Total penetration (meters below seafloor, mbsf): 17
Total number of cores: 3
Total number of drilled intervals: 0
Total length of cored section (m): 17
Total core recovered (m): 7.45
Core recovery (%): 43.8

Hole 1248C

Latitude: 44°34.45′N
Longitude: 125°9.1499′W
Time on hole (hr): 22.75 (1345 hr, 1 Aug–1230 hr, 2 Aug 2002)
Seafloor (drill pipe measurement from rig floor, mbrf): 841
Distance between rig floor and sea level (m): 11.4
Water depth (drill pipe measurement from sea level, m): 829.6
Total depth (drill pipe measurement from rig floor, mbrf): 990
Total penetration (meters below seafloor, mbsf): 149
Total number of cores: 17
Total number of drilled intervals: 0
Total length of cored section (m): 149
Total core recovered (m): 101.44
Core recovery (%): 68.1

Core	Date (Aug 2002)	Local time (hr)	Depth (mbsf)		Length (m)		Recovery (%)
			Top	Bottom	Cored	Recovered	
204-1248A-							
			*****Drilled from 0 to 194 mbsf*****				
204-1248B-							
1H	1	0935	0.0	6.5	6.5	2.32	35.7
2H	1	1100	6.5	16.0	9.5	4.42	46.5
3H	1	1220	16.0	17.0	1.0	0.71	71.0
			Cored totals:		17.0	7.45	43.8
			Drilled total:		0.0		
			Total:		17.0		
204-1248C-							
1X	1	1555	0.0	9.6	9.6	2.43	25.3
2X	1	1740	9.6	19.2	9.6	1.28	13.3
3X	1	1940	19.2	28.8	9.6	3.48	36.3
4X	1	2035	28.8	38.4	9.6	0.85	8.9
5X	1	2105	38.4	48.0	9.6	3.00	31.3
6H	1	2135	48.0	57.5	9.5	8.99	94.6
7H	1	2215	57.5	67.0	9.5	8.88	93.5
8H	1	2245	67.0	76.5	9.5	7.94	83.6
9H	1	2357	76.5	86.0	9.5	9.69	102.0
10H	2	0040	86.0	95.5	9.5	8.56	90.1
11H	2	0230	95.5	105.0	9.5	7.49	78.8
12H	2	0435	105.0	114.5	9.5	9.62	101.3

Table T1 (continued).

Core	Date (Aug 2002)	Local time (hr)	Depth (mbsf)		Length (m)		Recovery (%)
			Top	Bottom	Cored	Recovered	
13H	2	0510	114.5	124.0	9.5	7.01	73.8
14H	2	0610	124.0	133.5	9.5	7.02	73.9
15H	2	0650	133.5	136.5	3.0	3.03	101.0
16H	2	0735	136.5	142.0	5.5	5.65	102.7
17X	2	0900	142.0	149.0	7.0	6.52	93.1
				Cored totals:	149.0	101.56	68.1
				Drilled total:	0.0		
				Total:	149.0		

Table T2. Location of sampled carbonate concretions, Hole 1248B.

Section	Top (cm)	Bottom (cm)	Depth (mbsf)	Volume (cm^3)	Comments
204-1248B-1H-					
1	5	7	0.05	5	One piece; solid
1	107	112	1.07	10	Three pieces; solid
1	0	100	0	10	Two pieces; solid; exact depth unknown
2	10	15	1.3	10	One piece; solid
2	45	48	1.65	10	Two pieces; solid
CC	5	10	2.27	5	One piece; solid

Table T3. Bioevents, Hole 1248C.

Age (Ma)	Bioevent	Top Core, section	Top Depth (mbsf)	Bottom Core, section	Bottom Depth (mbsf)	Average depth (mbsf)	Event number	Comment
		204-1248C-		204-1248C-				
0.30	LO *Proboscia curvirostris*	Top	0.00	1X-CC	2.38	1.19	1	Diatom
0.46	LO *Pseudoemiliania lacunosa*	4X-CC	29.64	5X-CC	41.35	35.50	2	Nannofossil
1.59	FO *Calcydiscus macintyrei*	12H-CC	114.57	13H-CC	121.46	118.02	3	Nannofossil

Note: FO = first occurrence, LO = last occurrence.

Table T4. Interstitial water data, Holes 1248B and 1248C.

Core, section, interval (cm)	Depth (mbsf)	pH	Alkalinity (mM)	Salinity (g/kg)	Cl (mM)	SO_4 (mM)	NH_4 (mM)	PO_4 (µM)	Na (mM)	K (mM)	Mg (mM)	Ca (mM)	B (µM)	Ba (µM)	Fe (µM)	Li (µM)	Mn (µM)	Sr (µM)	DOC (mM)
204-1248B-																			
1H-1, 0–20	0.00	7.88	42.65	34	474	2.2	1.7	103	419	10.3	37.7	3.7	489	32.0	1.5	15.74	0.19	61.41	—
1H-2, 0–20	1.20	7.87	42.67	34	—	0.2	3.2	156	482	12.0	45.6	3.1	627	57.5	1.1	17.93	0.12	74.68	8.73
2H-1, 77–87	7.27	7.88	55.77	30	474	0.5	7.5	166	431	11.0		2.8	550	72.6	4.6	14.12	0.48	60.80	—
2H-3, 91–101	9.16	7.68	59.90	31	476	0.2	8.1	332	437	10.6	40.2	2.0	739	68.1	21.4	14.55	0.63	64.72	15.76
204-1248C-																			
1X-1, 138–148	1.38	8.33	52.12	25	412	0.2	0.8	69	365	9.2	30.1	3.0	474	25.7	1.4	15.38	0.28	47.85	—
2X-CC, 0–15	10.68	7.44	54.71	31	490	1.6	7.4	302	450	11.6	41.2	2.4	719	67.2	9.5	17.37	0.83	65.53	—
3X-1, 140–150	20.60	7.68	71.42	36	551	0.7	11.6	275	511	13.0	46.5	4.0	869	103.9	26.4	19.93	2.64	85.24	11.00
5X-1, 140–150	39.80	7.60	67.71	35	548	1.0	11.0	336	511	12.9	42.2	4.3	882	101.7	18.7	23.68	1.85	90.83	16.87
5X-CC, 18–28	41.18	7.63	69.10	35	560	0.6	—	300	521	13.8	41.7	3.2	908	108.3	18.6	25.10	1.48	92.31	—
6H-3, 129–139	51.05	7.58	67.49	35	561	0.5	14.5	321	531	14.4	41.6	2.9	914	107.7	8.5	25.94	0.76	94.81	18.17
6H-5, 140–150	53.84	7.63	65.28	34	541	0.4	13.1	324	456	13.2	38.8	2.8	902	112.5	28.2	27.10	0.97	94.53	—
7H-2, 140–150	60.40	7.66	66.02	35	559	1.9	13.4	308	484	14.4	19.5	3.4	875	106.2	5.5	29.17	1.28	99.65	15.47
7H-5, 140–150	64.90	7.44	67.48	35	568	0.0	13.6	380	494	13.6	39.7	3.3	—	—	—	—	—	—	—
8H-2, 137–147	69.87	7.45	68.10	35	565	0.5	14.3	346	494	13.5	40.0	3.3	745	114.0	3.2	35.12	0.38	81.16	14.55
8H-4, 140–150	72.80	—	—	—	—	—	—	—	—	—	35.6	2.5	888	126.5	10.1	29.57	0.53	101.99	—
8H-CC, 0–10	74.65	7.93	64.75	35	567	—	14.7	199	—	—	39.1	3.5	803	130.4	7.0	31.83	0.89	101.63	—
9H-2, 140–150	79.40	7.40	67.55	35	557	0.4	14.5	368	487	13.1	38.0	3.9	941	132.8	16.2	36.40	0.86	104.06	16.93
9H-5, 140–150	83.90	7.45	67.34	35	556	0.2	15.3	336	486	13.7	38.0	3.5	883	134.1	8.6	36.62	0.71	99.08	—
10H-2, 135–150	88.54	7.45	63.30	34	545	1.0	14.5	327	477	12.9	36.5	3.7	856	124.9	9.1	36.59	0.85	97.93	15.09
10H-5, 112–127	92.73	7.65	66.40	35	561	0.0	16.1	277	487	13.8	35.6	3.7	864	148.0	4.3	38.39	0.68	97.66	—
11H-2, 135–150	97.51	7.67	65.37	35	559	0.5	15.2	333	485	13.1	37.5	3.9	861	146.9	7.4	37.21	2.23	96.66	15.36
11H-4, 122–137	100.36	7.45	66.71	35	555	0.5	15.0	317	483	12.9	36.5	5.2	873	154.3	13.3	37.96	3.03	98.51	—
12H-2, 131–146	107.81	7.58	58.76	34	522	3.1	14.5	258	458	12.0	33.6	4.8	753	109.5	15.9	34.28	4.16	80.34	14.00
12H-5, 135–150	111.96	7.57	65.41	35	551	—	14.7	296	—	—	34.6	4.5	792	172.2	22.3	38.20	0.86	90.05	—
13H-2, 135–150	117.33	7.74	62.98	34	547	0.9	15.6	162	483	13.7	32.1	3.9	766	180.7	3.2	40.28	0.98	85.47	—
13H-4, 132–147	120.21	7.65	61.86	34	549	0.3	16.9	153	478	13.0	32.8	3.6	757	171.2	5.0	42.11	0.89	84.57	15.56
14H-2, 135–150	125.62	7.70	61.37	34	545	0.7	16.7	130	480	13.1	32.0	3.2	648	141.9	3.5	43.28	0.63	74.92	15.23
14H-5, 0–15	128.74	—	—	—	—	—	—	—	—	—	—	—	—	—	—	—	—	—	—
15H-2, 85–100	135.30	7.58	59.37	34	547	0.4	17.5	180	480	12.8	31.4	2.8	733	117.6	4.3	48.14	0.56	74.57	13.49
16H-1, 135–150	137.85	7.55	58.28	34	546	0.2	16.0	219	483	12.3	30.8	3.0	743	113.2	8.5	46.11	0.50	76.43	—
16H-3, 135–150	140.85	7.44	58.29	34	545	0.2	16.4	241	481	11.8	30.6	3.0	729	113.4	6.5	44.99	0.56	78.97	15.08
17X-1, 130–150	143.30	7.38	57.57	34	545	0.2	17.0	269	480	11.6	30.4	2.9	732	107.5	9.5	44.42	0.48	76.29	—
17X-3, 135–150	146.35	7.48	54.65	34	546	0.7	16.2	278	482	11.8	29.2	2.6	733	102.5	14.8	44.77	0.45	75.07	16.33

Notes: DOC = dissolved organic carbon. — = no sample was available.

Table T5. Concentrations of methane, ethane, ethylene, and propane in headspace gas, Holes 1248B and 1248C.

Core, section, interval (cm)	Depth (mbsf)	C_1 (ppmv)	C_2 (ppmv)	$C_{2=}$ (ppmv)	C_3 (ppmv)	C_1/C_2
204-1248B-						
1H-2, 0–5	1.20	37,715	62.9			599
1H-4, 0–5	6.00	1,685	2.9			583
1H-5, 0–5	7.00	7,827	10.7			732
2H-2, 38–39	7.75	118,447	258.9		10.7	457
2H-5, 42–43	10.82	292,790	595.4		35.2	492
204-1248C-						
1X-1, 0–5	0.00	29,475	45.7			645
2X-1, 0–5	9.60	11,329	12.9			878
3X-1, 145–150	20.65	16,585	24.1	0.5		688
3X-2, 108–113	21.78	13,264	23.7	0.4		560
4X-1, 0–5	28.80	158,896	252.7		37.1	629
5X-2, 105–110	40.95	10,666	13.6	0.5	41.5	785
6H-3, 0–5	49.76	13,475	7.3		22.1	1,848
6H-4, 0–5	51.15	8,285	7.1		25.3	1,175
7H-3, 0–5	60.50	12,330	6.3		26.3	1,945
7H-6, 0–5	65.00	10,709	4.4		21.7	2,456
8H-3, 0–5	69.97	12,423	4.4		20.0	2,823
9H-3, 0–5	79.50	17,380	7.6	0.4	31.9	2,296
10H-2, 0–5	87.19	13,346	6.7		24.2	1,998
11H-3, 0–5	97.66	47,621	11.6		42.4	4,112
12H-5, 0–5	110.61	22,686	52.6		40.1	431
13H-3, 0–5	117.48	17,304	100.9		89.1	171
14H-3, 0–5	125.77	16,719	335.1	0.7	201.9	50
14H-6, 0–5	130.24	7,761	179.4		82.6	43
15H-3, 0–5	135.45	15,984	450.4	0.9	335.0	35
16H-2, 0–5	138.00	18,874	566.9	0.9	437.2	33
17X-2, 0–5	143.45	7,274	251.9		255.8	29
17X-5, 0–5	147.45	10,614	346.8		302.8	31

Note: C_1 = methane, C_2 = ethane, $C_{2=}$ = ethylene, C_3 = propane.

Table T6. Concentration of light hydrocarbon and nonhydrocarbon gases in VAC samples of core gas void, Holes 1248B and 1248C.

Core, section, interval (cm)	Depth (mbsf)	C_1 (ppmv)	C_2 (ppmv)	C_3 (ppmv)	i-C_4 (ppmv)	n-C_4 (ppmv)	i-C_5 (ppmv)	n-C_5 (ppmv)	i-C_6 (ppmv)	n-C_6 (ppmv)	H_2S (ppmv)	CO_2 (ppmv)	O_2 (ppmv)	N_2 (ppmv)	C_1/C_2
204-1248B-															
2H-2, 70–71	8.07	858,023	1,731	88.4	30.9	8.6						12,554	1,736	1,286	496
2H-3, 50–51	8.75	834,876	1,698	84.6	28.6	4.8						11,793	1,677	1,219	492
204-1248C-															
1X-1, 100–101	1.00	948,012	1,282	27.3	15.7	5.1					4,276	3,305	7,448	23,982	740
3X-2, 113–114	1.83	958,373	928	10.5	6.9							16,201	2,632	2,679	1,033
5X-1, 148–149	39.88	935,862	470	166.4	94.9	47.9	18.9					39,401	2,269	3,202	1,991
6H-3, 99–100	50.75	511,882	160	72.0	11.9	7.8						8,362	93,230	364,922	3,201
6H-5, 69–70	53.13	972,788	320	50.1	6.2	4.3						6,238	95	961	3,037
6H-6, 120–121	55.14	936,879	321	52.0	6.2	4.4						5,947	9,092	29,497	2,920
7H-4, 20–21	62.20	966,565	203	112.4	18.1	10.9						5,575	1,995	1,754	4,759
7H-6, 4–5	65.04	927,900	102	173.5	NA	NA	NA	NA	NA	NA	NA	NA	NA	NA	9,106
8H-2, 15–16	68.65	770,525	129	113.2	20.3	10.9						15,439	43,174	167,507	5,974
8H-3, 2–3	69.99	975,948	360	25.1								6,128	1,457	993	2,711
8H-5, 6–7	72.96	871,816	172	114.8	NA	NA	NA	NA	NA	NA	NA	NA	NA	NA	5,063
9H-2, 20–21	78.20	955,294	284	40.0	NA	NA	NA	NA	NA	NA	NA	NA	NA	NA	3,361
9H-6, 99–100	84.99	972,360	189	84.5	11.0	5.8						10,313	1,033	1,056	5,139
10H-5, 132–133	92.91	964,287	141	118.9	14.3	7.5						15,771	1,421	1,335	6,844
10H-5, 132–133	92.91	950,209	137	116.2	NA	NA	NA	NA	NA	NA	NA	NA	NA	NA	6,956
11H-4, 70–71	99.84	979,838	178	96.8	NA	NA	NA	NA	NA	NA	NA	NA	NA	NA	5,495
11H-4, 70–71	99.84	974,197	175.3	100.9	8.8	4.4						8,668	56	963	5,557
11H-6, 28–29	101.54	923,730	183.4	129.7	18.8	9.2						51,628	3,352	6,972	5,037
12H-2, 98–99	107.48	974,347	430.7	83.1	6.3							12,303	80	832	2,262
12H-3, 134–135	109.30	979,029	1,012.8	115.9	10.0	5.0						7,362	845		967
13H-2, 7–8	116.05	965,767	1,218	445.6	79.7	61.4	19.2					16,755	95	956	793
13H-4, 101–102	119.90	798,002	1,719.46	377.3	74.9	58.4	22.6					27,677	35,069	132,810	464
14H-5, 101–102	129.75	947,460	5,707.7	1,272.7	225.7	466.8	196.5		8.7			30,445	1,199	1,050	166
15H-1, 56–57	134.06	919,295	13,076.3	16,163.8	3,503.9	1,180.2	225.4	125.7	44.9	14.8		25,688	1,049	1,008	70
16H-3, 107–108	140.57	762,952	5,599	2,059.1	360.9	547.4	202.5	114.8	36.4	10.7		20,029	162,249	41,995	136

Note: NA = not analyzed, C_1 = methane, C_2 = ethane, C_3 = propane, i-C_4 = isobutane, n-C_4 = normal butane, i-C_5 = isopentane, n-C_5 = normal pentane, i-C_6 = isohexane, n-C_6 = normal hexane, H_2S = hydrogen sulfide, CO_2 = carbon dioxide, O_2 = oxygen, N_2 = nitrogen.

Table T7. Composition of gas from analyses of decomposed samples of gas hydrate, Holes 1248B and 1248C.

Core, section, interval (cm)	Depth (mbsf)	C_1 (ppmv)	C_2 (ppmv)	C_3 (ppmv)	i-C_4 (ppmv)	n-C_4 (ppmv)	H_2S (ppmv)	CO_2 (ppmv)	O_2 (ppmv)	N_2 (ppmv)	C_1/C_2
204-1248B-											
1H-1, 50–55	0.50	970,905	1,337	14.2	7.3	4.1	11,812	2,227	1,188	1,444	726
1H-CC	2.22	476,042	762	98.1	28.5	7.2		3,072	86,386	377,811	625
2H-2, 0–25*	7.37	891,709	3,197	4,379	1,459	267		5,196	91	1,005	279
204-1248C-											
1X-2, 0–10	1.48	356,583	483	4.4	3.9		25.0	1,186	113,053	500,804	739
1X-CC*	2.24	969,865	1,722					16,201	2,632	2,862	563
3X-CC	22.38	943,030	1,253	23.1	12.3			7,863	6,954	22,746	753
3X-CC	22.38	939,921	1,298		4.5			5,808	7,851	25,889	724
6H-2, 48–53	49.71	872,949	421	19.6				3,375	23,779	88,520	2,072
8H-6, 85–87	74.63	979,093	327	13.9				5,103	23	442	2,994
8H-6, 85–87	74.63	979,018	341	18.6				5,057	24	400	2,874
10H-1, 100–119	87.00	845,931	419	30.3				4,193	29,324	112,138	2,017

Notes: * = pure gas hydrate sample (minimal contamination from sediment). C_1 = methane, C_2 = ethane, C_3 = propane, i-C_4 = isobutane, n-C_4 = normal butane, H_2S = hydrogen sulfide, CO_2 = carbon dioxide, O_2 = oxygen, N_2 = nitrogen.

Table T8. Carbonate carbon, calcium carbonate, total carbon, organic carbon, total nitrogen, and total sulfur contents and C/N ratios, Holes 1248B and 1248C.

Core, section, interval (cm)	Depth (mbsf)	Carbonate carbon (wt%)	$CaCO_3$ (wt%)	Total carbon (wt%)	Organic carbon (wt%)	Total nitrogen (wt%)	Total sulfur (wt%)	C/N
204-1248B-								
2H-3, 33–34	8.58	0.50	4.19	1.55	1.05	0.18	0.8	5.83
204-1248C-								
1X-1, 116–117	1.16	2.46	20.49	3.40	0.94	0.11	0.82	8.55
4X-1, 25–26	29.05	0.14	1.13	1.23	1.09	0.14	0.31	7.79
7H-3, 75–76	61.25	0.47	3.92	1.59	1.12	0.21	0.32	5.33
8H-3, 75–76	70.72	0.52	4.33	1.45	0.93	0.19	0.31	4.89
9H-3, 75–76	80.25	0.53	4.44	1.86	1.33	0.17	0.24	7.82
10H-4, 75–76	90.86	0.15	1.24	1.77	1.62	0.19	0.69	8.53
11H-6, 76–77	102.02	0.49	4.09	1.88	1.39	0.23	0.58	6.04
12H-5, 77–78	111.38	0.24	2.03	1.10	0.86	0.14	0.17	6.14
13H-5, 77–78	121.13	0.45	3.76	1.72	1.27	0.17	0.85	7.47
14H-5, 72–73	129.46	0.50	4.14	1.58	1.08	0.15	0.29	7.20
16H-1, 77–78	137.27	1.11	9.26	2.17	1.06	0.16	0.31	6.63
17X-5, 77–78	148.22	0.99	8.26	1.57	0.58	0.14	0.20	4.14

Table T9. Rock-Eval pyrolysis of samples, Hole 1248C.

Core, section, interval (cm)	Depth (mbsf)	Organic carbon (wt%)	S_1 (mg/g)	S_2 (mg/g)	Production index (S_1/[S_1+S_2])	Hydrogen index (mg S_2/g C)	T_{max} (°C)
204-1248C-							
9H-3, 75-76	80.25	1.33	0.25	1.46	0.15	110	400
11H-6, 76-77	102.02	1.39	0.33	1.65	0.17	119	404
13H-5, 77-78	121.13	1.27	0.27	1.69	0.14	133	408
14H-5, 72-73	129.46	1.08	0.21	1.19	0.15	110	404
16H-1, 77-78	137.27	1.06	0.24	1.62	0.13	153	409
17X-5, 77-78	148.22	0.58	0.16	1.13	0.12	195	415

Note: S_1 and S_2 are as defined in **"Organic Matter Characterization,"** p. 18, in "Organic Geochemistry" in the "Explanatory Notes" chapter.

Table T10. Presence of gas hydrate based on infrared images of cores in liners, Hole 1248C.

Core, section	ΔT (°C)	Gas hydrate texture*	Depth interval (mbsf)†		Anomaly designation‡	Sampled interval		
			Top	Bottom		Top (cm)	Bottom (cm)	Depth (mbsf)
204-1248C-								
1X	–2.5		1.30	2.20	IR107	71	76	2.19
1X-2	–5.7		2.21	2.27	IR108			
1X-CC	–0.5	Background uncertain; could be 1.0 ΔT.	9.60	10.88	IR109	0	14	2.24
3X-3	–0.5	Poor recovery but generally cold	19.20	20.00	IR110	0	3	21.83
3X	–1.6	Cold spot in generally cold core	20.00	20.10	IR111			
3X	–1.0	Some variability	20.10	22.68	IR112			
4X	–4.1	Some variability	28.80	29.65	IR113			
5X	–0.5	Disseminated; slight variability; questionable	38.40	41.40	IR114			
6H	–1.6	Nodular	48.10	48.30	IR115			
6H	–4.0	Nodular	49.30	49.40	IR116			
6H-2	–5.5	Disseminated	49.70	49.77	IR117	48	53	49.71
6H	–0.9	Vein; crosses bedding	50.70	51.20	IR118			
6H	–3.6	Disseminated; ΔT from 0.2 to 0.5	52.10	52.20	IR119			
6H	–0.4	Disseminated	52.30	53.10	IR120			
6H	–0.5	Nodular	53.50	53.70	IR121			
6H	–4.9	Vein parallel to bedding	54.00	54.20	IR122			
6H	–1.9	Disseminated	55.60	55.70	IR123			
6H	–1.6	Disseminated	56.00	56.80	IR124			
6H	–1.4	Nodular?	57.30	57.40	IR125			
7H	–1.1	Disseminated	58.10	58.20	IR126			
7H	–0.7	Vein; low dip	58.80	59.20	IR127			
7H	–1.9	Disseminated	59.40	59.60	IR128			
7H	–1.3	Disseminated	60.20	60.35	IR129			
7H	–1.0	Disseminated above possible vein	60.40	60.55	IR130			
7H	–1.0	Disseminated above vein	61.00	61.50	IR131			
7H	–2.8	Disseminated	63.20	63.35	IR132			
7H	–2.0	Nodular with possible vein	64.20	64.50	IR133			
7H	–2.2	Nodular with possible vein	65.70	65.90	IR134			
7H	–0.8	Disseminated	65.95	66.00	IR135			
8H	–0.8	Nodular	67.90	68.00	IR136			
8H	–0.8	Vein	68.20	68.40	IR137			
8H	–2.0	Massive?	69.90	70.00	IR138			
8H	–5.7	Vein	71.10	71.30	IR139			
8H	–1.5	Nodular/massive	72.00	72.10	IR140			
8H-6	–7.4	Nodular	75.20	75.60	IR141	66	87	74.44
9H	–1.0	Disseminated	78.50	78.65	IR142			
9H	–0.8	Vein; shallow dip	79.40	79.60	IR143			
9H	–2.3	Vein; moderate dip	80.50	80.60	IR144			
9H	–2.0	Disseminated	81.90	82.00	IR145			
9H	–2.0	Disseminated	82.80	82.90	IR146			
9H	–2.0	Massive; disrupted?	82.80	82.90	IR147			
10H-1	–8.1	Nodular	88.10	88.40	IR148	100	119	87.00
10H	–3.5	Nodular	89.50	89.70	IR149			
10H	–2.8	Nodular	90.30	90.50	IR150			
10H	–4.6	Nodular	92.50	92.55	IR151			
10H	–3.0	Nodular	92.70	92.80	IR152			
10H	–4.9	Disseminated	94.75	94.80	IR153			
11H		Disseminated	95.50	97.20	IR154			
11H	–1.0	Disseminated	97.20	97.25	IR155			
11H	–0.9	Nodular (or blade?)	97.26	99.40	IR156			
11H-5	–5.6	Disseminated	101.00	101.10	IR157	38	75	100.89
11H	–5.6	Disseminated; ΔT varies 0.3 to 1.1	102.50	102.60	IR158			
12H	–0.9	Vein	105.00	105.25	IR159			
12H	–2.6	Disseminated	107.40	107.50	IR160			
12H	–0.5	Nodular	108.27	108.32	IR161			
12H-4	–4.7	Nodular/disseminated	110.90	111.00	IR162	105	115	110.51
13H	–2.0	Disseminated	120.05	120.20	IR163			
14H	–1.1	Disseminated	124.15	124.25	IR164			

Notes: * = from anomaly characteristics and core description, if available. † = from uncut core liner. ‡ = used for reference to specific anomalies in text and figures. The difference between these depth intervals and the equivalent curated section depth intervals is typically less than 1 m.

Table T11. Moisture and density, Holes 1248B and 1248C.

Core, section, interval (cm)	Depth (mbsf)	Density (g/cm^3)		Porosity (%)
		Bulk	Grain	
204-1251B-				
2H-1, 26–28	6.76	1.554	2.641	67.2
2H-1, 74–76	7.24	1.557	2.690	68.0
2H-3, 30–32	8.55	1.513	2.720	71.2
2H-3, 71–73	8.96	1.488	2.744	73.0
2H-4, 21–23	9.47	1.592	2.725	66.6
2H-4, 80–82	10.06	1.631	2.738	64.6
2H-5, 25–27	10.65	1.586	2.761	67.7
204-1251C-				
1X-1, 40–42	0.40	1.588	2.734	67.0
1X-1, 88–90	0.88	1.640	2.764	64.6
1X-1, 120–122	1.20	1.624	2.850	67.1
2X-1, 89–91	10.49	1.581	2.666	66.1
3X-1, 50–52	19.70	1.654	2.695	62.3
3X-2, 45–47	21.15	1.628	2.662	63.1
3X-3, 41–43	22.24	1.795	2.676	53.3
4X-1, 7–9	28.87	1.598	2.710	66.0
4X-1, 19–21	28.99	1.639	2.714	63.6
4X-1, 28–30	29.08	1.683	2.751	61.8
4X-1, 38–40	29.18	1.619	2.734	65.2
5X-1, 40–42	38.80	1.635	2.655	62.6
5X-1, 90–92	39.30	1.676	2.637	59.6
5X-2, 60–62	40.50	1.688	2.714	60.7
6H-1, 54–56	48.54	2.014	2.809	44.5
6H-2, 28–30	49.51	1.731	2.769	59.5
6H-3, 70–72	50.46	1.675	2.639	59.7
6H-5, 74–76	53.18	1.708	2.697	59.1
6H-7, 50–52	55.94	1.700	2.775	61.4
7H-1, 74–76	58.24	1.732	2.756	59.1
7H-3, 74–76	61.24	1.711	2.698	58.9
7H-5, 74–76	64.24	1.743	2.716	57.5
8H-1, 74–76	67.74	1.745	2.645	55.5
8H-3, 18–20	70.15	1.744	2.692	56.8
8H-3, 40–42	70.37	1.964	2.739	45.2
8H-3, 74–76	70.71	1.730	2.710	58.1
8H-5, 74–76	73.64	1.679	2.634	59.3
9H-1, 94–96	77.44	1.668	2.685	61.2
9H-3, 74–76	80.24	1.744	2.759	58.5
9H-4, 101–103	82.01	1.771	2.772	57.3
9H-5, 100–102	83.50	1.760	2.674	55.4
9H-7, 74–76	85.74	1.839	2.757	53.0
10H-2, 74–76	87.93	1.743	2.765	58.7
10H-3, 91–93	89.60	1.734	2.774	59.5
10H-4, 74–76	90.85	1.743	2.620	55.0
10H-6, 36–38	93.24	1.737	2.784	59.5
11H-1, 30–32	95.80	1.738	2.790	59.6
11H-2, 30–32	96.46	1.766	2.750	57.0
11H-2, 120–122	97.36	1.760	2.695	56.0
11H-3, 74–76	98.40	1.785	2.771	56.5
11H-6, 74–76	102.00	1.722	2.696	58.3
12H-1, 74–76	105.74	1.758	2.751	57.5
12H-3, 74–76	108.70	1.725	2.719	58.6
12H-5, 74–76	111.35	1.771	2.686	55.1
12H-6, 94–96	113.05	1.817	2.728	53.5
12H-6, 123–125	113.34	1.753	2.766	58.1
13H-1, 74–76	115.24	1.793	2.749	55.4
13H-3, 74–76	118.22	1.756	2.680	55.8
13H-5, 74–76	121.10	1.789	2.682	53.9
14H-2, 76–78	125.03	1.750	2.678	56.1
14H-3, 74–76	126.51	1.760	2.664	55.1
14H-4, 47–49	127.71	1.767	2.635	53.9
14H-5, 69–71	129.43	1.864	2.633	47.8
14H-6, 18–20	130.42	1.780	2.559	50.8
14H-6, 32–34	130.56	1.739	2.472	50.6
15H-1, 34–36	133.84	1.773	2.689	55.1
15H-2, 33–35	134.78	1.784	2.686	54.3
15H-2, 50–52	134.95	1.812	2.678	52.4
15H-3, 70–72	136.15	1.804	2.658	52.3
16H-1, 74–76	137.24	1.819	2.699	52.5
16H-3, 74–76	140.24	1.799	2.700	53.8
16H-4, 40–42	141.40	1.777	2.714	55.5
17X-1, 74–76	142.74	1.779	2.674	54.3
17X-3, 74–76	145.69	1.743	2.689	56.8
17X-5, 74–76	148.19	1.947	2.716	45.4

Table T12. Thermal conductivity, Hole 1248C.

Core, section, interval (cm)	Depth (mbsf)	Thermal conductivity (W/[m·K])	Individual measurements (W/[m·K])		
204-1248C-					
4H-1, 25	29.05	0.893	0.908	0.886	0.886
5H-1, 40	38.80	0.914	0.937	0.911	0.893
6H-3, 50	50.26	0.968	0.969	0.961	0.975
7H-3, 75	61.25	1.000	1.007	0.982	1.010
8H-3, 75	70.72	0.944	0.916	0.944	0.973
9H-1, 75	77.25	0.845	0.849	0.85	0.835
9H-3, 70	80.20	1.044	1.011	1.060	1.060
9H-5, 75	83.25	1.084	1.066	1.090	1.095
10H-3, 68	89.37	0.986	0.986	0.996	0.975
11H-2, 75	96.91	1.017	1.026	1.013	1.012
11H-4, 63	99.77	0.990	0.972	0.992	1.006
11H-6, 75	102.01	0.892	0.877	0.888	0.910
12H-3, 55	108.51	0.928	0.935	0.923	0.925
12H-6, 75	112.86	1.061	1.057	1.045	1.082
13H-3, 75	118.23	1.051	1.075	1.043	1.036
14H-3, 80	126.57	1.053	1.05	1.044	1.065
15H-3, 65	136.10	1.062	1.039	1.070	1.078
16H-3, 75	140.25	1.062	1.077	1.056	1.052
17X-3, 75	145.70	0.998	0.996	1.008	0.991

Table T13. Temperature measurements, Holes 1248B and 1248C.

Core	Depth (mbsf)	Temperature (°C)	Thermal conductivity (W/[m·K])	Tool ID
204-1248B-				
3H	17.0	4.38	0.89	APCT 12
204-1248C-				
9H	86.0	8.82	1.08	APCT 12
11H	105.0	9.93	0.89	APCT 12
2X–3X	19.2	5.28	0.89	DVTP 2
11X–12X	105.0	10.38	—	DVTPP 3*
17X–18X	149.0	7.80	—	DVTPP 2*

Notes: APCT = advanced piston corer temperature tool, DVTP = Davis-Villinger Temperature Probe, DVTPP = Davis-Villinger Temperature-Pressure Probe, ID = identification. Measurements for which two core numbers are given (e.g. 204-1248C-2X–3X) were made with the DVTP or DVTPP between these two cores. APCT measurements were made at the core catcher of the core listed. For APCT measurements, thermal conductivity represents the average of the nine measurements taken in the adjacent core. * = not used for calculation of temperature gradient.